Methods of Diffusing Pulse Detonation Combustion

Adam Martin Janka

Thesis submitted to the faculty of the Virginia Polytechnic Institute and State University
in partial fulfillment of the requirements for the degree of

Master of Science
In
Mechanical Engineering

Uri Vandsburger, Chair
Alan A. Kornhauser
Walter F. O'Brien

April 30, 2014
Blacksburg, VA

Keywords: Pressure gain combustion, pulse detonation combustion, wave dynamics

Methods of Diffusing Pulse Detonation Combustion

Adam Martin Janka

ABSTRACT

Pulse detonation combustion has been of interest for many years since it offers several advantages over standard deflagrative combustion. In theory, detonative combustion is a better use of fuel compared to deflagrative combustion since less entropy is generated during a detonation. As a result, detonation offers higher pressure and temperature gain across the wave front compared to the comparable deflagration. Since a detonation is a supersonic event which uses a shock to compress and dissociate reactants, a Pulse Detonation Combustor (PDC) is a relatively simple device that does not necessarily require a large compressor section at the inlet. Despite these benefits, using a turbine to extract work from a PDC is a problem littered with technical challenges. A PDC necessarily operates cyclically, producing highly transient pressure and temperature fields. This cyclic operation presents concerns with regards to turbine reliability and effective work extraction.

The research presented here investigated the implementation of a pulse detonation diffuser, a device intended to temporally and spatially distribute the energy produced during a detonation pulse. This device would be an inert extension from a baseline PDC, manipulating the decaying detonation front while minimizing entropy production. A diffuser will seek to elongate, steady, attenuate, and maintain the quality of energy contained in the exhaust of a detonation pulse. These functions intend to reduce stresses introduced to a turbine and aid in effective work extraction. The goal of this research was to design, implement, and evaluate such a diffuser using the using conventional analysis and simulated and physical experimentation.

Diffuser concepts using various wave dynamic mechanisms were generated. Analytical models were developed to estimate basic timing and wave attenuation parameters for a given design. These models served to inform the detail design process, providing an idea for geometric scale for a diffuser. Designs were simulated in ANSYS Fluent. The simulated performance of each diffuser was measured using metrics quantifying the wave attenuation, pulse elongation, pulse steadying, and entropy generation for each design. The most promising diffuser was fabricated and tested using a detonation tube. Diffuser performance was compared against analytical and computational models using dynamic pressure transducer diagnostics.

This research was funded in part by the National Energy Technology Laboratory (NETL), a subgroup of the Department of Energy (DOE).

Table of Contents

List of Figures

List of Tables

Nomenclature

PDC	Pulse Detonation Combustor
DDT	Deflagration-to-Detonation Transition
PDD	Pulse Detonation Diffuser
ZND	Zeldovich-von Nuemann-Doring
CJ	Chapman-Jouguet
η_{th}	Thermal Efficiency
π_c	Compression Ratio
ε	Strain
u	x-direction Velocity
CV	Control Volume
CS	Contact Surface
γ	Specific Heat Ratio
a	Speed of Sound, Specific Availability
M	Mach Number
q	Heat release
x	x Position, non-Dimensional Specific Volume
y	y Position, non-Dimensional Pressure
RH	Rankine-Hugoniot
η	RH Equation Intermediate
K	RH Equation Intermediate
J_+, J_-	Riemann Invariants
A	Availability
a_f	Flow Availability/Exergy
α	Area Ratio
ζ	Entropy Generation Ratio
U	Wave Speed
MW	Molecular Weight
L_{run}	Run-up Duct Length
θ	Wedge Angle

PR	Pressure Ratio
t_{duct}	Wave Transit Time
Π	Pressure Attenuation Ratio
CoV	Coefficient of Variance
τ	Pulse Elongation Ratio
ϵ	Effectiveness
f_{op}	PDC Operating Frequency
ϕ	Equivalence Ratio
λ	Detonation Cell Size
D	Diameter
σ	Stress
Φ	Dynamic Amplification Factor
DAQ	Data Acquisition
TOF	Time of Flight
$TOFMN$	Time of Flight Mach Number
CFD	Computational Fluid Dynamics
PP	Partial Pressure
VR	Volume Ratio

Indices

CJ	Chapman-Jouguet
i	Incident
r	Reflected
t	Transmitted
int	Interface
BD	Blowdown
L	Leading
w	Wall
m	Main
s	Secondary
amb	Ambient
0	Initial
nom	Nominal
$corr$	Corrected
$evac$	Evacuation
add	Added

Chapter 1: Introduction

1.1 Background

A detonation wave is supersonic event in which a non-stationary shock wave is coupled to and sustained by a reaction front burning upstream of it. Unlike deflagration which is characterized by slight pressure loss to moderate pressure gain, detonation results in a large net pressure gain across the wave front [1,2].

A Pulse Detonation Combustor (PDC) is a device which is used to generate detonation waves. A PDC consists of a tube which is repeatedly filled with a detonable mixture and ignited at a closed end. A detonation develops along the length of the tube through a process known as Deflagration to Detonation Transition (DDT), with the wave then exiting the tube at the open end. After the detonation products naturally blow down to atmospheric pressure, the tube is purged with an inert medium and the cycle repeats. Figure 1.1 illustrates the pulse detonation cycle [3]. If filled and ignited at a fast enough rate, a PDC could be applied either in a propulsion or work extraction application.

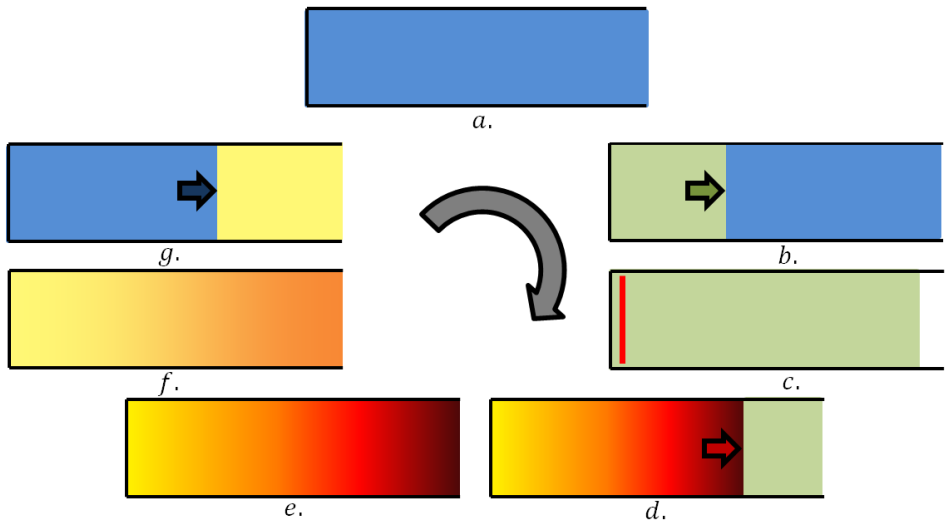

Figure 1.1. Schematic of a pulse detonation cycle. *a*. Initial state *b*. Filling with fuel *c*. Detonation initiation *d*. Detonation propagation *e*. Detonation exit *f*. Isentropic blowdown *g*. Purging

1.2 Motivation

Detonation is commonly modeled as constant volume heat addition, as opposed to deflagration which is modeled as constant pressure. Knowing this, the Humphrey Cycle is selected as an appropriate cycle analogue for a PDC-work extraction system [4]. Similarly, the

Brayton Cycle has been chosen to model a conventional gas turbine installation. The Humphrey cycle assumes initial reactant compression presumably by a fan or small compressor section (0→1), followed by constant volume heat addition (1→2), isentropic expansion (2→3), and isobaric heat rejection back to the original state (3→0). The Brayton Cycle shares the same processes except for the noted difference in heat addition. When compared against a Brayton cycle with the same heat addition and initial compression (Figure 1.2), numerous advantages of the Humphrey Cycle become clear. The first point of interest is the entropy generated during heat addition. It can be shown that a constant volume heat addition only generates ~75% of the entropy compared to that of the constant pressure heat addition [5]. To further back this entropy argument, Petela analytically demonstrated that a detonation wave destroys less exergy than a comparable deflagration [6]. This diagram also shows that detonations reach higher temperatures than deflagrations for the same fuel ($T_{defl} = T_{ad} \approx 2800$ K, $T_{det} = T_{CJ} \approx 3000$ K for acetylene-air mixtures) [1]. Using this kind of cycle analysis, it has be theorized that a PDC can achieve higher first and second law efficiencies over a deflagrative combustor for a wide range of initial compression ratios and fuels [4,7,8].

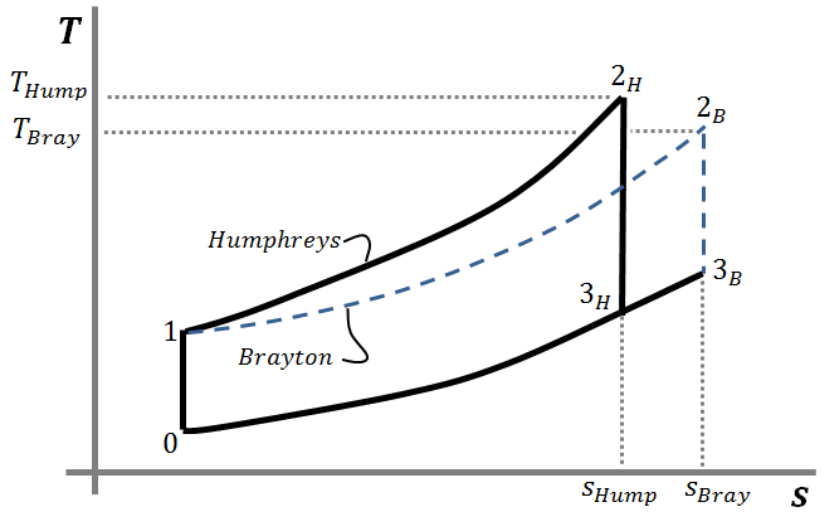

Figure 1.2. T-s diagrams of Humphrey and Brayton cycles. Note that $T_{Hump} > T_{Bray}$ and $s_{Hump} < s_{Bray}$.

Along with the thermodynamic considerations, PDC systems would be much simpler mechanical devices compared to conventional gas turbine installations. A practical pulse detonation system would not require large compressor sections, unlike most gas turbines in use today. The self-compressive nature of the detonation event would only require small compressor or fan sections to facilitate in operation [7,8].

Despite the potential benefits, the implementation of PDC's for energy generation is plagued by numerous practical issues. The inherently unsteady operation of a PDC specifically presents complications with regard to work extraction and turbine reliability [9]. Figure 1.3 is a plot of an outlet pressure history of a fully filled PDC. This figure contains experimental data (black) and the general shape (red). The pressure event generated by a detonation wave occurs for ~8 ms and reaches a magnitude of ~200 psi, depending on the mixture and tube geometry. To this end, the duty cycle of a detonation pulse over the entire cycle is very small, on the order of 10% assuming $f_{op} = 25$ Hz.

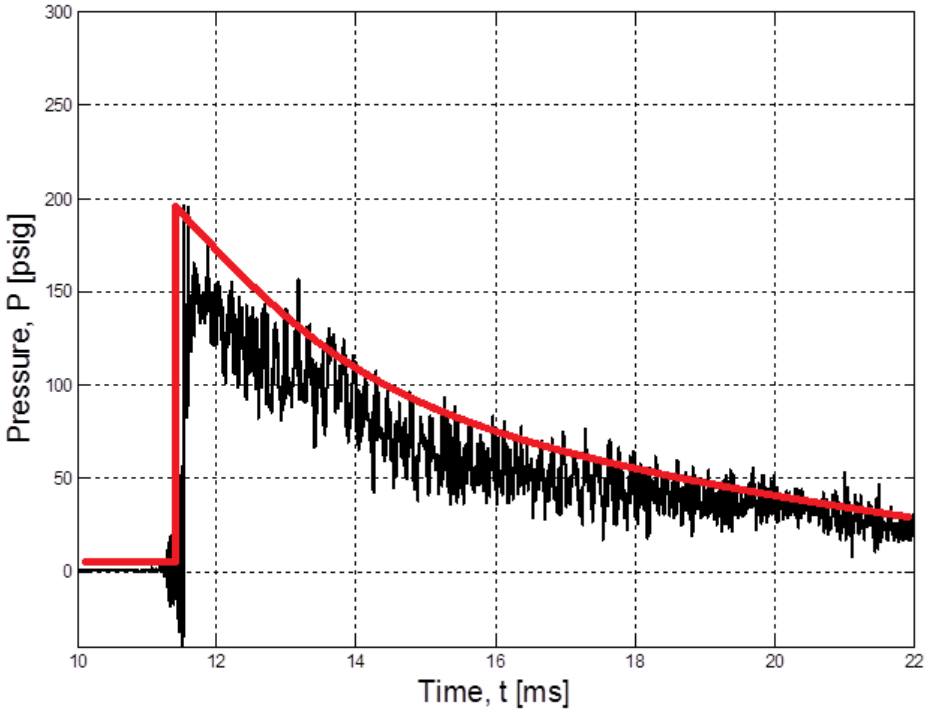

Figure 1.3. An experimental outlet pressure history of PDC. Experimental data is shown in black, general wave shape is shown in red.

Modern turbine sections are designed for steady operation and considered to be extremely valuable components of the gas turbine assembly. Among others, groups at GE Global Research and the Air Force Research Laboratory have successfully constructed and operated their own PDC-turbine hybrid systems. These systems used non-optimized turbocharger turbine sections used in pulsed flow applications, although not optimized for pulse detonation flow. Not surprisingly, their experiments demonstrated that actual cycle efficiencies are far lower than predicted values. Also, the operating histories of these prototype devices are severely limited, on

the order of hours [10–15]. As such, the mechanical reliability of the turbine sections under the highly unsteady detonation conditions is yet to be determined.

1.3 Project Scope, Objectives

The aim of the present work is to design, implement and experimentally evaluate a pulse detonation diffuser (PDD) which will spatially and/or temporally distribute the energy generated by a PDC. In doing so, the PDD will mitigate the stresses introduced to the turbine section, aid in work extraction, and minimize entropy generation during blowdown. The PDD will act as an inert extension to a pulse detonation device, analogous to a nozzle. This treatment of the problem places the emphasis on the wave dynamic manipulation of a decaying detonation. Effects such as combustion chemistry, heat transfer, and combustor-turbine interface are important factors, but will not be taken into consideration.

The current state of this application has exclusively used off-the-shelf turbine sections, mostly those found in turbochargers [10–14,16]. While measured stresses on these turbine sections were not alarmingly high, it should be noted that these turbines were non-optimized for pulse detonation flow [10]. To this end, it may be that an optimized turbine section could be vulnerable to the extreme pulse detonation conditions, necessitating a diffuser of some kind.

Goals for this project include:

- Design, construction and shakedown of a lab-scale PDC analogue
- Preliminary design of diffuser concepts using standard analytical techniques
- Computational evaluation of diffuser concepts using CFD
- Final design and construction of the most promising diffuser concept(s)
- Experimental evaluation of diffuser using the lab-scale PDC analogue

1.4 Literature Review

The literature review of this report will focus on application specific concepts and prior research efforts. It will cover theoretical, experimental and numerical treatments of the pulse detonation work extraction problem. It will also briefly discuss the differences between propulsive and work extraction pulse detonation applications, and highlight progress made toward understanding a partially filled PDC.

Hutchins and Metghalchi performed an ideal power cycle analysis comparing Humphrey and Brayton cycles. In this analysis, they computed thermal efficiency, η, and exergetic effectiveness, ε, assuming the same heat of reaction, the same initial compression, and isentropic expansion of combustion products. Their results suggest that the Humphrey cycle will outperform the Brayton cycle over wide range compression ratios $2 < \pi_C < 15$ for both Methane and JP-10 as fuels [4]. Following this approach, Bellini also performed a cycle analysis comparing the application of deflagrative and detonative combustion modes. In her analysis, she developed the ZND cycle which incorporates all elements of the ZND detonation model including adiabatic shock compression followed by heat addition to the Chapman-Jouguet state. Like Hutchins, Bellini also concluded that the ZND cycle outperforms the Brayton cycle over a wide range of pre-compression ratios and fuels. For a stoichiometric methane-air, the thermal efficiency of a Brayton cycle increased monotonically with initial compression, achieving $\eta_{th,max} = 59.4\%$ at $\pi_C = 25$. For the same mixture, the thermal efficiency of the ZND cycle demonstrated a negative concavity with respect to initial compression, achieving $\eta_{th,max} = 63.3\%$ at $\pi_C = 7$ [7]. Extending this analysis, Bellini and Lu also compared ZND and Brayton cycles by considering thermal efficiency and exergetic effectiveness, taking into account the potential effects of PDC frequency. As before, the ZND cycle was more efficient and effective than the Brayton cycle, and their analysis suggested that increases in PDC frequency will improve performance [8].

Despite the theoretical analysis, there is only a small body of work investigating experimental pulse detonation work extraction. A group at GE Global Research (GEGR) has built and tested two PDC-turbine hybrid systems to date [10–13]. The second of these two prototypes interfaced an array of 8 PDC's with a locomotive turbocharger designed for nominal flows of 8 lbm/s, 25000 rpm and 1000 hp. The flow was a combination of primary (PDC) and secondary (cooling, bypass) flow in an attempt to simulate conditions in a turbofan fan arrangement. This system ran on stoichiometric ethylene-air mixtures and has logged 96 minutes of run history. The primary focus of the GEGR work was to assess this system's performance level and mechanical response to detonation loading. They tested this hybrid over a wide range of operating frequencies, fill fractions and firing orders, and found that the system output 100 hp at 11000 rpm on average. At most, the system was pushed to an output of 350 hp at 18000 rpm

[11]. This group also instrumented the stator and rotor portions of the turbine to investigate the mechanical loading on these components. They found maximum strain to be 363 $\mu\varepsilon$ for simultaneous firing, 252 $\mu\varepsilon$ for co-rotating firing, and 206 $\mu\varepsilon$ for counter-rotating firing. They noted that the values were well under the yield limits of the turbine material, but did not rule out the possibility of dynamic excitation of the turbine section [10]. Also, pressure measurements made at the inlet and exit of the turbine indicated a 20 dB attenuation across the single turbine stage, indicating strong wave attenuation [12].

A similar group at the Air Force Research Laboratory (AFRL) also built and operated a simpler PDC-turbine hybrid. Their design consisted of only one tube that was interfaced with an automotive turbine [14]. Similar to GEGR, their work focused on measuring performance, but with their work they also computed thermal efficiencies of their system. With the PDC interfaced with the turbine over a wide range of operating conditions, the values for thermal efficiency were all low, ranging from η_{th}= 3.7 to 5.9%. They also noted that the effect of having a turbine as an end condition greatly increased the blowdown time of the tube, increasing it from ~2 ms to greater than 10 ms.

The underwhelming performance of these PDC-turbine hybrid systems has been elucidated by numerical studies investigating the nature of the flow field between PDC's and turbine sections. A GEGR group experimentally and numerically investigated how shock fronts and detonation fronts interact with two-dimensional turbine blade cascades. Their experiments and simulations both showed that a significant portion of a detonation front reflected from the blade cascade [17]. A study by Van Zante et al. was similar to that of the GEGR group. However, their geometry was more complex since they modeled a 1/8th annulus of a single stage turbine, incorporating stator passages and translating rotor passages. Their work also noted that the jet of mass flow provided by a PDC was too great to be accommodated by the passages between stator vanes, resulting in significant reflection and backflow. They also properly noted that the availability of pulse detonation flow is higher than that of steady, constant pressure flow, but the process of work extraction served as a major limitation [18]. A review paper by St. George and Gutmark highlights the complications in pulsed flow work extraction, discussing both conventional pulsed flow in turbochargers and extending the discussion to pulse detonation work extraction [9].

Pulse detonation as a pure propulsive means has been a point of interest dating back to the 1920's [19]. A comprehensive review of the latest developments in PDE research for aerospace applications has been provided by Kailasanath [20,21]. While the premises of pulse detonation in pure propulsion and work extraction applications are similar, the desired end goals are quite different. The fundamental difference between these fields is that propulsion applications seek to convert the detonation products' thermal energy into kinetic energy for momentum exchange [22].

Despite the differences in end use, several themes are common between pure propulsion and work extraction applications. Specifically, the practice of partially filling a detonation combustor involves filling a portion of the combustion tube with reactive mixture while the rest contains the inert purging gas. It has been shown both experimentally and numerically that partial filling is an effective means of throttling a PDC without changing the operating frequency [20,21]. Li and Kailasanath numerically investigated the wave dynamics of a partially filled PDE fueled with a stoichiometric mixture of ethylene and oxygen. They identified three types of waves which occur in a partially filled PDE: the detonation wave, interface expansion waves, and exit expansion waves. The interface expansions waves are generated as the detonation front meets the reactive-inert interface, whereas the exit expansion waves are generated at the decaying shock meets the tube exit. They noted that the strength of the transmitted shock/decaying detonation continually weakened as the wave traveled down the inert portion of the tube [23–25]. Similarly, Wintenberger et al. developed and verified an analytical model for detonation impulse generation based on one-dimensional wave dynamic theory. In their study, they showed that a detonation wave will always generate expansion waves when refracting into an inert medium. This conclusion assumes that the pressure of the reactive mixture is the same as the inert mixture [26,27].

Chapter 2: Theory Review

The current chapter of this paper is dedicated to theoretical treatments of important topics in compressible fluid dynamics. Much of the design and analysis employed in this project relies heavily on the concepts presented herein. The chapter begins by introducing the Rayleigh and Hugoniot Equations for a general wave front. These equations are then specialized and applied to steady, normal shocks (no heat release) and steady, normal detonations (heat release). The chapter concludes by introducing expansion waves and describing the wave dynamic processes at work in a partially filled PDC.

2.1 Rayleigh, Hugoniot Equations

The following section outlines the derivation of the Rayleigh Line and Hugoniot Curves. More details regarding the material presented here can be found in numerous texts [1,2,28].

Figure 2.1 illustrates the zero-dimensional control volume of a generic wave (detonation or shock) travelling from left to right. For now, the coordinate system will be wave-fixed, so that the analysis will be steady-state. As such, velocities are all measured relative to the wave.

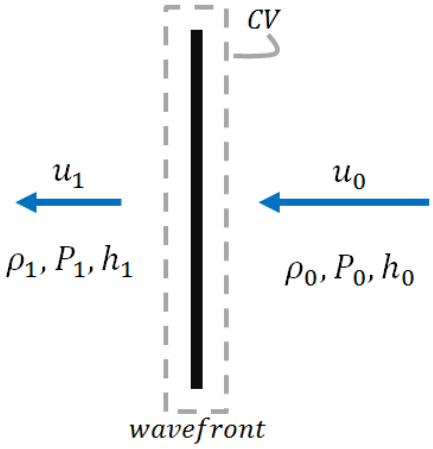

Figure 2.1. Control volume of 1-D, stationary wave.

For this one-dimensional system, conservation of mass, momentum and energy may be written as

$$\rho_0 u_0 = \rho_1 u_1 \qquad \textbf{2.1}$$

$$P_0 + \rho_0 u_0^2 = P_1 + \rho_1 u_1^2 \quad \textbf{2.2}$$

$$\sum_i^N x_i (h_{f,i}^0 + \Delta h_{s,i}) + \frac{u_0^2}{2} = \sum_j^M x_j (h_{f,j}^0 + \Delta h_{s,j}) + \frac{u_1^2}{2} \quad \textbf{2.3}$$

where it is assumed that the area is constant. Here, the subscripts 0 and 1 indicate reactants and products, respectively. The symbol *P* denotes pressure, u denotes velocity, ρ denotes density. In Equation 2.3, $h_{f,i}^0$ and $\Delta h_{s,i}$ indicate the formation enthalpy and sensible enthalpy of species *i*. Under the perfect gas assumption ($P = \rho RT$, $c_v, c_p = const.$) and using the relationships $R = c_v - c_p$ and $\gamma = c_p/c_v$, the sensible enthalpy, Δh_s, can be expressed as

$$\Delta h_s = \frac{\gamma}{\gamma - 1}\left(Pv - P_{ref} v_{ref}\right) \quad \textbf{2.4}$$

where $v = 1/\rho$.

With Equations 2.3 and 2.4, it is convenient to assume that state 0 and the reference state are equal, which is usually standard atmospheric conditions. Another useful parameter, Mach number of state 0, is defined as $M_0 = u_0/a_0$. Here, a_0 is the speed of sound in the reactant mixture and is defined as $c_0 = \sqrt{\gamma_0 R_0 P_0 v_0}$. Using this Mach number definition along with Equations 2.1 - 2.4, we may derive the following:

$$y = (1 + \gamma_0 M_0^2) - (\gamma_0 M_0^2) x \quad \textbf{2.5}$$

$$y = \frac{\frac{\gamma_0 + 1}{\gamma_0 - 1} - x + \frac{2}{P_0 \rho_0} * q}{\frac{\gamma_1 + 1}{\gamma_1 - 1} x - 1} \quad \textbf{2.6}$$

where the mass weighted difference in formation enthalpy is defined as $q = \sum_i^N x_i h_{f,i}^0 - \sum_j^M x_j h_{f,j}^0$. Equations 2.5 and 2.6 are commonly referred to as the Rayleigh Line and Hugoniot Curve. Here, the non-dimensional variables $x = v_1/v_0$ and $y = P_1/P_0$ are introduced for simplicity. For a given detonation or shock wave, the intersection of these equations in the *x*-*y* plane specifies the thermodynamic solution to a given problem. When $q = 0$, the solution describes a shock. When $q \neq 0$, the solution describes a detonation.

2.2 Shocks and Detonations

Normal Shock Relations

Again using Equations 2.1 - 2.3, and assuming no heat release, one may derive relations of thermodynamic properties across a normal shock. A shock is an infinitesimally thin discontinuity in a flowfield which causes finite changes in flow properties such as pressure, temperature, etc. [29]. Such a discontinuity arises in supersonic, compressible flow where pressure "information" of an event cannot be transmitted to upstream fluid elements before the event arrives. Unlike the Rayleigh Line and Hugoniot Curve, the normal shock relations describe changes in properties using only the upstream Mach number relative to the shock, M_0. These derivations are described in detail in numerous texts, but the derivations will not be shown here [29–31]. Once more assuming a perfect gas, we can derive the following:

$$M_1^2 = \frac{1 + [\frac{\gamma - 1}{2}]M_0^2}{\gamma M_0^2 - (\gamma - 1)/2}, \tag{2.7}$$

$$\frac{P_1}{P_0} = 1 + \frac{2\gamma}{\gamma + 1}(M_0^2 - 1), \tag{2.8}$$

$$\frac{T_1}{T_0} = \left[1 + \frac{2\gamma}{\gamma + 1}(M_0^2 - 1)\right]\left[\frac{2 + (\gamma - 1)M_0^2}{(\gamma + 1)M_0^2}\right]. \tag{2.9}$$

These equations are highly useful since they are strictly function of γ and M_0 only. In diffuser design, the use of absolute properties, as opposed to total properties, prove to be the most convenient option. Also, it should be noted that density, entropy, speed of sound etc. can be evaluated using these equations and perfect gas relations.

Ideal Detonation Wave Structure

Building on the definition of a shock, the ZND model of a steady detonation consists of three parts: a leading normal shock, the induction zone, and the reaction zone. An illustration of ZND Detonation is shown in Figure 2.2. The leading shock serves to compress and heat the reactants such that they begin to dissociate in the induction zone. The dissociated species then recombine and exothermically react via an auto-ignition process until the products reach the CJ state. Note that the detonation is a self-sustaining process like a deflagration. However, unlike a

deflagration, a detonation is by necessity a supersonic phenomenon since the reaction zone is coupled with a leading shock front [2].

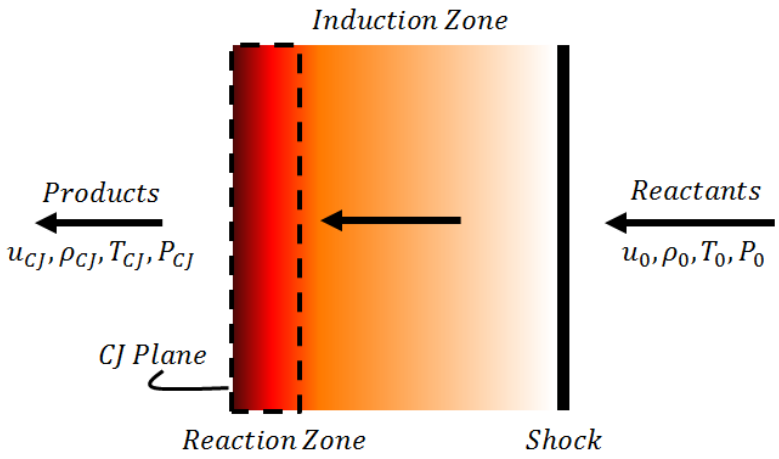

Figure 2.2. Illustration of the ZND Detonation Model.

Using a first order kinetics model, one may spatially resolve temperature, pressure, and velocity in the induction zone

Rankine-Hugoniot Detonation Relations

Take the ZND model introduced in the previous section. Let us simplify it from a one-dimensional to a zero-dimensional model where heat is instantaneously added to reactants, as shown in Figure 2.1. For a given heat release, q, the Rayleigh Line and Hugoniot Curve may intersect at two places, describing two possible solutions. This effect is illustrated in Figure 2.3. In the detonation quadrant, the upper intersection signifies a strong detonation and the lower intersection signifies a weak detonation. Another situation exists in which the Rayleigh Line is exactly tangent to the Hugoniot Curve. This solution is known as the Chapman-Jouguet (CJ) solution, or the tangency solution [1,2,28].

While strong and weak detonations are rarely observed experimentally, most experimental detonation wave speeds closely match the wave speed predicted under the CJ conditions. The reason for this agreement between the CJ theory and experiment and theory is a complex and is extensively discussed by Lee [2]. That said, it can be shown the CJ solution implies two important results. First, the Mach number downstream of a CJ detonation is exactly sonic relative to the wave front, that is $M_1 = M_{CJ} = 1$. Second, the CJ solution minimizes entropy for the detonation process [2].

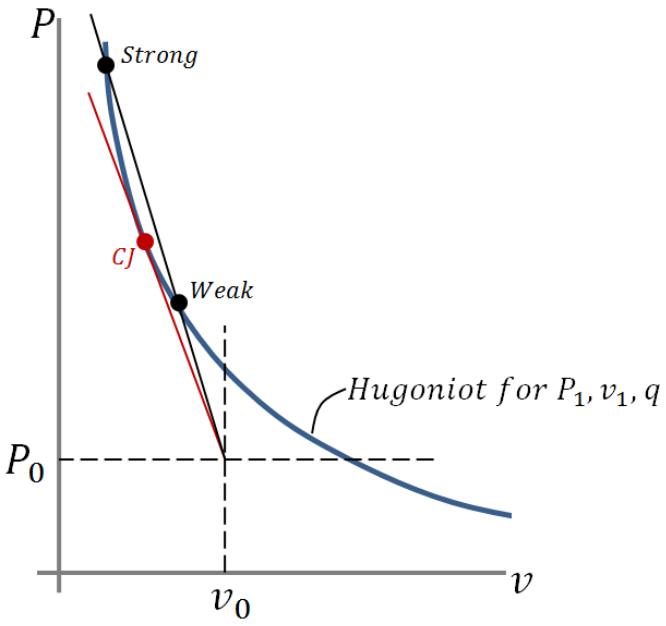

Figure 2.3. Rayleigh Line and Hugoniot Curve. The black Rayleigh line produces two detonation solutions, strong and weak. The red Rayleigh line is the tangency solution, yielding the CJ condition.

Similar to the normal shock relations, the Rankine-Hugoniot (RH) relations for a CJ detonation relates thermodynamic properties across the wave using the wave speed, M_{CJ}. The RH equations are given as:

$$\eta = \frac{1}{M_{CJ}^2} = \frac{\gamma_0}{\gamma_1}\left(1 - \frac{2}{1+\sqrt{1+4\gamma_0/K\gamma_1}}\right) \quad \textbf{2.10}$$

$$K = \frac{2\gamma_0(\gamma_1+1)}{\gamma_1^2}\left[\frac{\gamma_1-\gamma_0}{\gamma_0-1} + \gamma_0(\gamma_1-1)\frac{q}{P_0 v_0 \gamma_0}\right] \quad \textbf{2.11}$$

$$\frac{P_1}{P_0} = \frac{\gamma_0+\eta}{(\gamma_1+1)\eta} \quad \textbf{2.12}$$

$$\frac{T_1}{T_0} = \frac{P_1}{P_0}\frac{R_0}{R_1}\frac{\gamma_1(\gamma_0+\eta)}{\gamma_0(\gamma_1+1)} \quad \textbf{2.13}$$

where K is an intermediate value and R_0 and R_1 are the gas constants of the reactants and products. This model, unlike the normal shock relations, is a "*2 gamma*" model – it assumes different specific heat ratios for reactants and products. This assumption improves the model's accuracy, although it is not required.

It should be noted that Equations 2.9 - 2.12 are less accurate for readily detonable mixtures. Readily detonable mixtures contain less nitrogen and achieve higher temperatures and greater dissociation of products, skewing analytical estimates of the heat release, q. Because of this, calculations involving fuel-air mixtures tend to be quite accurate, whereas fuel-oxygen calculations are much less so [27]. Also, these formulae have been derived under the assumption of zero-dimensional, steady state wave propagation. As will be discussed, these assumptions are *highly* idealized when compared to a real detonation wave. Thus, the RH relations are useful primarily as estimating tools. More accurate estimates can achieved through the use of equilibrium solvers, such as NASA's Chemical Equilibrium and Applications (CEA) code. These solvers still assume steady propagation and zero-dimensionality, but account for dissociation of the products.

Real Detonation Wave Structure

As alluded to before, the ZND model of the detonation structure is highly idealized. In reality, a detonation wave is transient, three-dimensional front with complex, non-linear propagation mechanics. As summarized by Lee, a stable detonation front consists of a network of transverse shockwaves travelling along the diameter of the tube. These transverse waves create cellular patterns on the inside of the tube with a scale length that is characteristic to the particular mixture [1,2,32]. The detonation cell size is a commonly used length scale used to characterize another phenomenon, Deflagration-to-Detonation Transition (DDT). In general, a larger cell size indicates a less reactive mixture [2].

Wave-Fixed vs. Laboratory-Fixed Reference Frame

The Normal Shock and RH Detonation relations previously presented were all derived using a wave-fixed reference frame. In this frame, an observer is moving with the wave such that wave appears to be motionless to the observer. As such, the reactants are moving into the wave with some supersonic velocity, u_0 and $M_0 > 1$. This wave-fixed reference frame can be transformed into a laboratory-fixed reference frame in a simple manner. In a laboratory-fixed frame, an observer is motionless and the wave is propagating with some wave speed U into either a quiescent or non-quiescent mixture. Figure 2.4 illustrates this transformation, and further explanation of this transformation can be found in numerous resources [30,33].

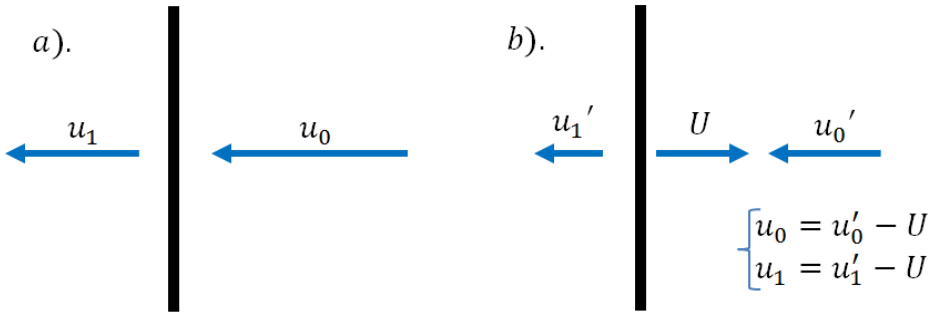

Figure 2.4. Wave-fixed to laboratory-fixed reference transformation.

A wave-fixed reference frame is most useful for steady, compressible flow analysis, such as in air-breathing engine diffuser design. Conversely, a lab-fixed reference frame is most useful in shock tube and detonation tube analysis. It should be noted that this transformation of coordinates has no effect on the computation of absolute thermodynamic properties. It only effects the computation of particle speeds and Mach numbers.

2.3 Expansion Waves

Expansion waves are another phenomenon found in shock tubes and detonation tubes. Unlike a sound wave, an expansion wave is of finite size and the fluid properties change throughout the wave. An ideal expansion wave isentropically drops pressure, density and temperature compared to downstream values. Also, the local fluid velocity and speed of sound are a function of wave position. As a result, the head and tail of an expansion wave travel at different total velocities. It is also important to note that expansion waves induce particle motion in the direction opposite their propagation [30,33].

The thermodynamic property distribution through an expansion wave can be approximated using the method of characteristics. Similar to Prandtl-Meyer flow in steady, two-dimensional flows, the method of characteristics as applied to unsteady, one-dimensional flows allows the wave to be discretized into n characteristic lines [29,30,34,35]. For a given characteristic, C_+ or C_-, the Riemann invariants, J_+ and J_-, remain respectively constant throughout. The Riemann Invariants are defined as

$$J_+ = u + \frac{2a}{\gamma - 1} = const.\,(along\ C_+\ characteristic) \qquad \textbf{2.14}$$

and

$$J_- = u - \frac{2a}{\gamma - 1} = const.\,(along\ C_-\ characteristic) \quad \textbf{2.15}$$

where u is the local particle velocity and a is the local speed of sound. If both Riemann invariants are known at any point, for any flow, then the local fluid velocity and speed of sound can be computed. Using the Ideal Gas equation of state, one could then compute any thermodynamic property at a given point in the flow.

Expansion waves which ideally originate from a single point are known as a centered wave. Centered waves are commonly found in detonation analysis as a Taylor Waves. Centered waves are also exist when shocks interact with discontinuities such abrupt area changes or changes in propagation medium (refraction) [35,36]. These flows will be discussed later as applied to detonation diffuser design and analysis. For centered waves, the Riemann invariants remain constant through the extent of the wave. With this, for left-running waves

$$J_- = constant\ through\ the\ wave \quad \textbf{2.16}$$

and for right-running waves

$$J_+ = constant\ through\ the\ wave. \quad \textbf{2.17}$$

From this fact, one will find that particle velocity and speed of sound vary linearly through an expansion wave, along with temperature, pressure and density.

2.4 Wave Dynamics of a Partially Filled PDC

Understanding the wave dynamics of a partially filled PDC is essential in understanding the mechanisms at work in an inert diffuser. In this section, a quasi-steady, one-dimensional refraction analysis and unsteady, pseudo one-dimensional simulations are presented. As will be discussed, the refraction analysis provides preliminary insight whereas the computational efforts paint a much more detailed picture of the mechanisms at work. The theory presented here utilizes concepts previously presented in the chapter.

Quasi-Steady, One-Dimensional Refraction Analysis

As stated previously, this problem will focus on the wave dynamics of a detonation decaying into an inert medium. The process of a detonation meeting an inert interface can be

treated as one-dimensional, quasi-steady wave refraction problem [26,27]. Refraction is the process by which a wave meets a material/medium interface and the transmitted wave speed does not equal the incident wave speed [36]. In this case, the downstream medium is atmospheric air and the upstream medium is the detonation products at the CJ state. Two possible solution types exist for this problem and Figure 2.5 illustrates the wave diagrams for each case. In both cases, a shock, M_t, is transmitted. However, depending on the CJ state, the reflected wave may either be a shock or expansion wave. Note that the Taylor wave which immediately follows a detonation front in a closed tube is not considered in the refraction solution. Also note the contact surface which forms, representing an ideal boundary between the air passing through the transmitted shock wave and the detonation products passing through the reflected wave. A contact surface is an idealized flow discontinuity across which no particles diffuse, but has equal pressures and velocities on either side. That said, other flow properties like density, entropy and temperature differ on each side [36].

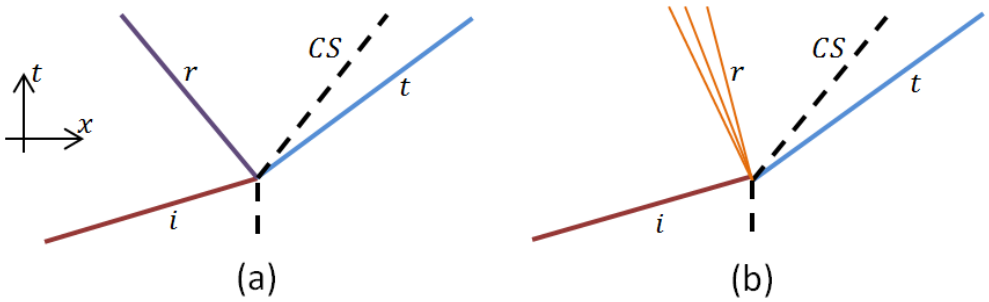

Figure 2.5. Wave diagrams for a detonation refracting into air.

The nature of the reflected wave depends on the CJ state relative to the shock adiabat. The shock adiabat, shown in Figure 2.6, is the curve which describes all possible post-shock pressures and velocities for all wave speeds. If the CJ state lies above the adiabat in Region 1, the reflected event will be an expansion wave. If the CJ state lies below the adiabat in Region 2, the reflected event will be a shock. With regard to pulse detonation engines, the reflected will always be an expansion front for any detonable hydrocarbon mixtures [26,27].

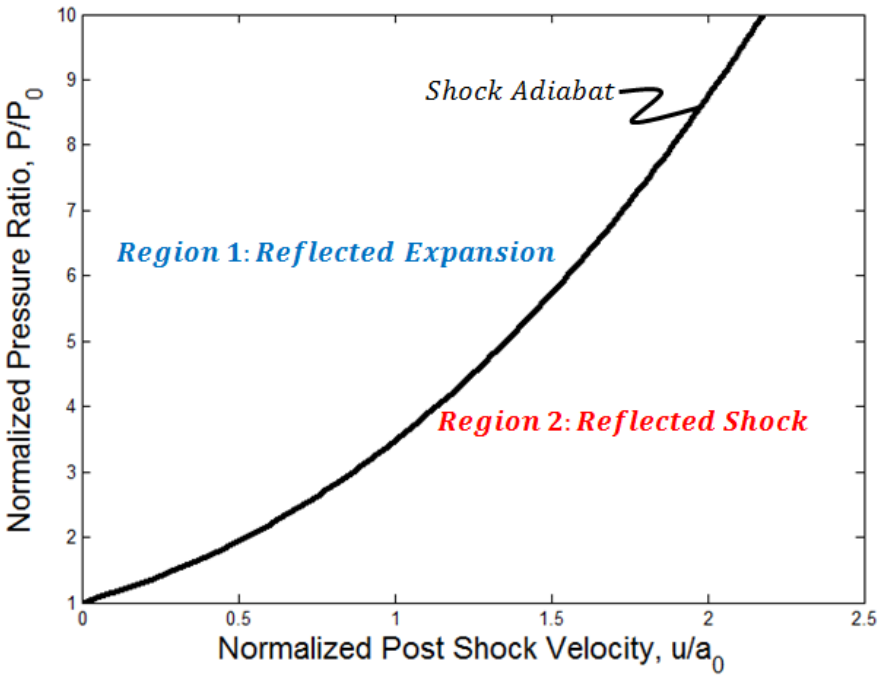

Figure 2.6. The shock adiabat indicates the induced particle velocity, u, for a given shock pressure ratio, P/P_0. If CJ conditions lie above the adiabat for a refraction analysis, the reflected wave is an expansion. If below, the reflected wave is a shock.

For most wave interaction problems, the solution is determined by satisfying the contact surface criterion, that is, equal velocities and pressures on either side. With a reflected expansion wave, the detonation products meet the wave and isentropically expand and decelerate. With the transmitted shock, air is compressed and accelerated. The solution for the refraction event is where the expansion wave expands/decelerates detonation products to the same pressure and velocity induced by the transmitted shock. It is convenient to graphically solve these problems in the pressure-velocity domain, as shown in Figure 2.7. The intersection of the curves represents the pressure and velocity unique to a certain shock wave speed and expansion wave. The speed indicated by this intersection is the velocity of contact surface, whereas the wave speed of the transmitted shock will be greater than this value.

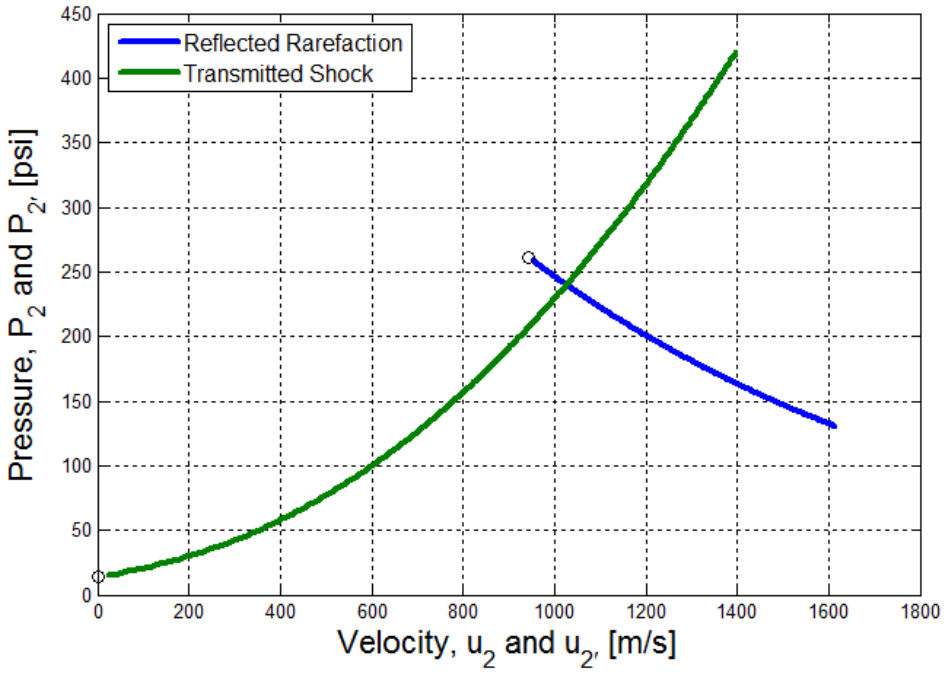

Figure 2.7. Refraction solution in the pressure-velocity domain.

Unsteady, Pseudo-One Dimensional Simulations

The previous refraction analysis assumes quasi-steadiness, meaning the waves are non-stationary but the solution is self-similar and scales with time. This sort of analysis is not suitable for an understanding of the unsteady interactions which occur in the combustor. That said wave diagrams are a useful tool for visually and qualitatively understanding unsteady wave interactions in quasi-one-dimensional systems. Although previously introduced in Figure 2.5, a more detailed example of such a diagram as applied to a detonation combustor is shown in Figure 2.8. These diagrams are oriented such that the time axis is vertical and the spatial axis is horizontal. In this example, a detonation is refracting into an inert medium, where the transmitted shock continually weakens by the remnants of the Taylor Wave. Exit expansion waves form when the detonation meets the reactive-inert interface located at L_{int}. While they can be drafted with quantitative, finite-difference schemes, this process is traditionally graphical and quite tedious. See references for methods describing wave diagram construction [30,33,35,36]. As such, this particular example is illustrative only and was not drafted using calculation.

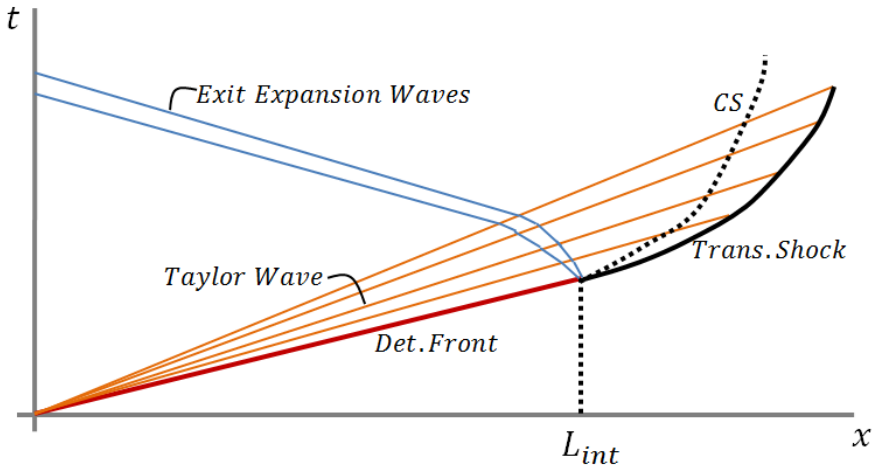

Figure 2.8. Sample wave PDC wave diagram depicting a detonation refracting into an inert medium. L_{int} refers to the reactive medium-inert medium interface.

With the advent Computation Fluid Dynamics (CFD), drafting wave diagrams has become antiquated. Pressure, temperature, density, and velocity centerline contours from CFD simulations are valid substitutes and offer intricate description of the system of interest. Example pressure and temperature contours from a CFD simulation are shown in Figure 2.9. This figure illustrates a model detonation interacting with a partial fill interface. In this simulation, an ideal detonation initial condition where the detonation front has just reached the reactive-inert interface was assumed. The basis for this initial condition will be discussed further in the Section 4.2. For reader orientation, $x = 0$ corresponds with the tube back wall, $x = 0.95\ [m], t = 0$ corresponds to the initial reactive-inert interface, and $x = 2\ [m]$ corresponds to the open end of the tube.

Numerous features of these plots are worthy of discussion. From the pressure contour:

- The strength of the transmitted shock continually decays as it travels down the tube. This is indicated by the continually decreasing slope of the shock contour/characteristic. It is also indicated by the magnitude (color) of the pressure behind the shock front. Immediately after refraction begins, the pressure is ~200 psi (red) and drops to ~100 psi (cyan) by the time the shock leaves the tube. This attenuation is caused by incident and re-reflection of the Taylor expansion waves from the original detonation event [23,24]. This wave exists as a result of the close wall boundary condition and is a physical necessity of the PDC system [37].

- A centered expansion fan originates at the original reactive inert interface. Kailasanath and Li called these “interface expansion waves” [23,24]. Similarly, expansion waves originate at the tube opening as the shock exits the tube. These expansion waves serve to drop the pressure in the tube and are the primary blowdown/exhaust mechanisms and are treated as isentropic processes within the tube. As such, the detonation products expand without loss as the detonation refracts into the inert section of the tube.

From the temperature contour:

- As discussed in the refraction analysis, a contact surface separating the shocked air and the expanding detonation products forms. The speed of the contact surface is slower than that of the transmitted shock. Figure 2.9 also shows that the contact surface is decelerating as it travels down the tube due to the effects of the Taylor Wave.
- The enthalpy difference between the shocked air and the detonation products is made clear. The shocked air is relatively low temperature ($< 1000\ K$, blue) whereas the detonation products are very high temperature ($\sim 2500\ K$, orange/red). As such, the region of lower enthalpy corresponds to the regions of higher pressure.

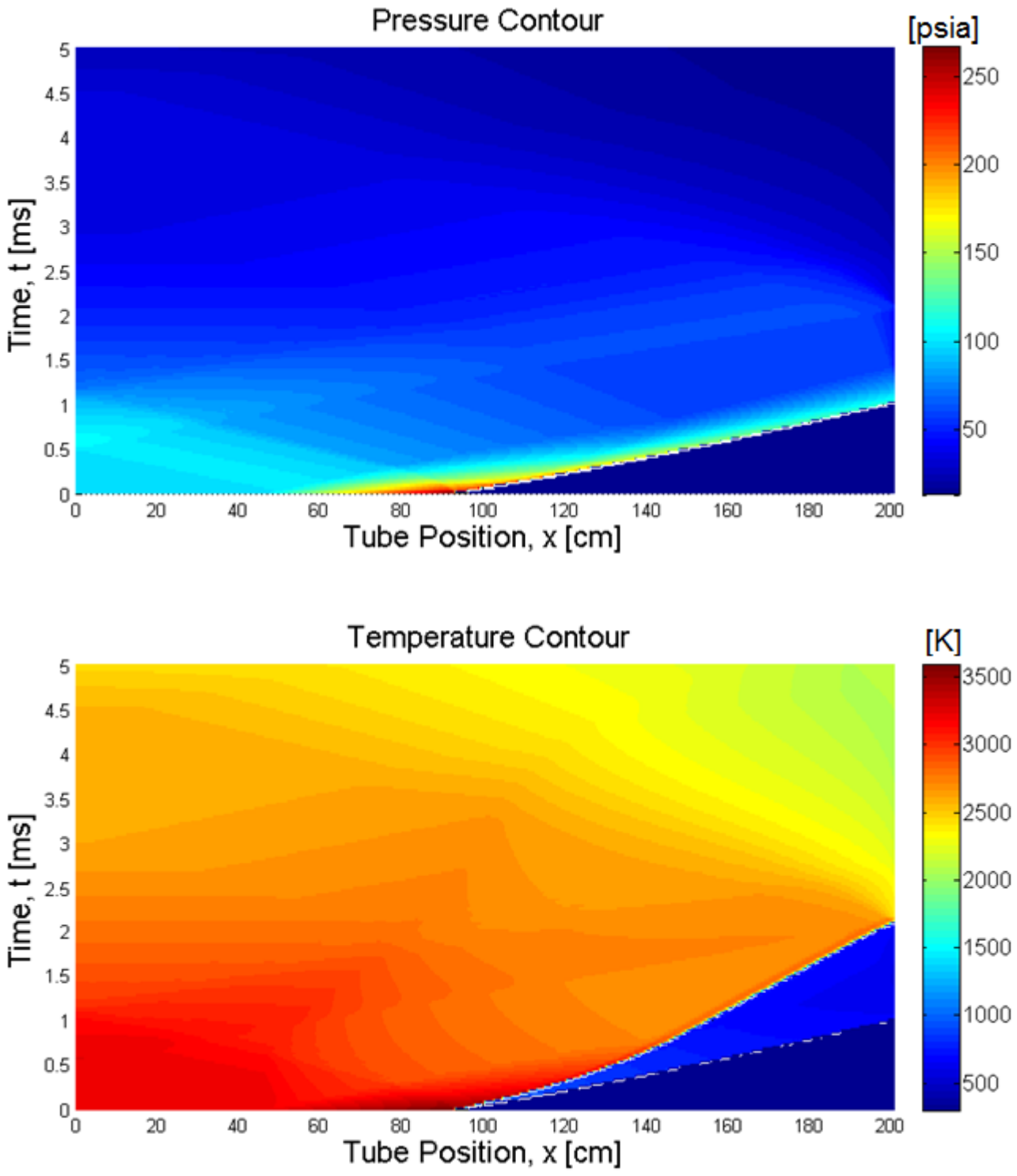

Figure 2.9. Centerline pressure and temperature contours of a partially filled PDC.

2.5 Thermodynamics of a Partially Filled PDC

It is the author's opinion that this problem lends itself particularly well to a thermodynamic availability analysis. For a detailed discussion on availability and thermoeconomics, the reader is encouraged to see a text by Moran [38]. Moran defines availability as "…the maximum work that can be extracted from the combined system of a control mass and environment as the control mass passes from a given state to the dead state." Unlike energy, which is always conserved under the First Law, availability is not a conserved quantity. Availability may be destroyed by irreversible processes within the control mass such as frictional losses, shock losses, and mixing. Simple examples where energy is conserved but availability is destroyed include throttling valves, heat exchangers, and mixers. Thermomechanical availability of a control volume can be computed by

$$A = [(E + KE + PE) - E_0] + P_0(V - V_0) - T_0(S - S_0) \qquad \textbf{2.18}$$

where E, KE and PE are internal, kinetic and potential energy. As usual, P, V, T and S denote pressure, volume, temperature and entropy. Here, quantities with a "0" subscript indicate the constant values taken on the by the environment of interest. Also, Equation 2.18 assumes the environment is at rest i.e. $v_0 = 0$. As this equation implies, the more a system deviates from the environment, the more work can be extracted from that system. The availability rate equation for an adiabatic, open system is expressed as

$$\frac{dA_{CV}}{dt} = -\left(\dot{W}_{CV} - P_0 \frac{dV_{CV}}{dt}\right) + \sum a_{fi}\, \dot{m}_i - \sum a_{fe}\, \dot{m}_e - \dot{I} \qquad \textbf{2.19}$$

where $\dot{W}_{CV}$ is the work done by the control volume, a_f is the flow availability, or exergy, $\dot{m}$ is the mass flow rate and $\dot{I}$ is the irreversibility generation within the control volume. The flow availability or exergy is a property used in open system analysis and incorporates the enthalpy of the flow. Exergy is defined as

$$a_f = (h - h_0) - T_0(s - s_0) + \frac{u^2}{2} \qquad \textbf{2.20}$$

where u is the velocity of the flow. Let us apply these concepts to a PDC control volume, as illustrated in Figure 2.10. The initial condition for this system will assume that all fuel has reacted at the detonation wave has reached the reactive-inert interface. Enthalpy, entropy and

velocity profiles along the tube length can be found assuming an ideal Taylor Wave follows an ideal, CJ detonation front. In this analysis, we will not consider the detonation propagation mechanisms and assume that the wave was instantly generated at the back wall. Given this control volume, one can simplify Equation 2.19 to

$$\frac{dA_{CV}}{dt} = -a_{fe}\dot{m}_e - \dot{I} \qquad \textbf{2.21}$$

where the first term on the right hand side accounts for the outflow and the second term accounts for entropy generation. Integrating Equation 2.21 and rearranging, we arrive at

$$A(t=0) = \int_0^{t_{BD}} a_{fe}\dot{m}_e dt + A(t=t_{BD}) + \int_0^{t_{BD}} \dot{I} dt \qquad \textbf{2.22}$$

where t_{BD} is the time at which combustor blowdown has finished. In words, Equation 2.22 can be described as

(Initial Availability in the Tube) = *(Exergy Advected thru the Exit)* + *(Final Availability left in the Tube after Blowdown)* + *(Availability Destroyed by Irreversibilities)*

In this case, blowdown is completed when the exergy flux leaving the tube approaches zero. This differs from an aerospace application, where blowdown is completed when the thrust surfaces have reached ambient pressure [27]. An effective configuration will seek to maximize the exergy which is advected through the tube opening by minimizing entropy generation and residual availability. Note that configurations in this study will have the same initial availability since the charged section is a constant.

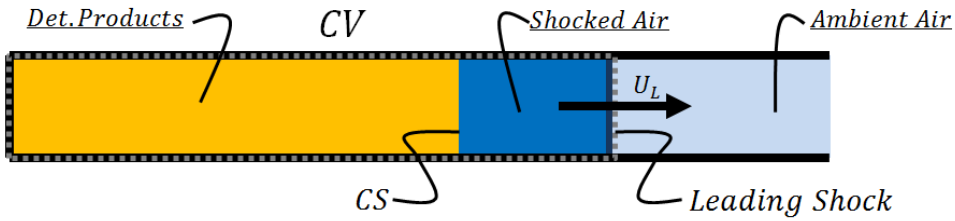

Figure 2.10. Control volume of a PDC. Contents of the CV include expanding detonation products separated from shocked air at the Contact Surface. Note that the leading shock is contained within the Control Volume.

By applying the availability rate equation to an ideal, partially filled tube, it can be shown that the availability within the tube decreases as the leading shock propagates out of the tube. Specifically, the author has proved the following result:

$$\frac{dA_{CV}}{dt}(t) = -\frac{P_0 a_0}{R_0} * Y * M_L(t) * \Delta s_L(t) \qquad \textbf{2.23}$$

where P_0 and a_0 are the ambient pressure and speed of sound, R_0 is the gas constant for air, Y is the cross sectional area of the tube, and $M_L(t)$ and $\Delta s_L(t)$ are the strength and entropy rise across the leading shock at time t. This result shows that partial filling alone destroys availability at a rate proportional to the leading shock strength.

Chapter 3: Analytical Modeling, Diffuser Design

This chapter details the first half of the design process surrounding the development of a diffuser for a PDC. It begins by clearly stating the problem/task at hand and highlights the design process as a whole. It then delves into the details of this design process, discussing concept generation, detailed design and analytical model development

3.1 Introduction

Problem Definition

For a given charge of fuel-oxidant mixture, the diffuser will aim to mitigate extreme pressure fluctuations without destroying high availability products generated during the detonation event of PDC. The diffuser will not contain reactive mixture and will serve as an inert extension of the charged combustor. As such, all configurations will have the same quantity of chemical energy as an input to the system. This steers the problem in the direction of wave and fluid dynamics as opposed to combustion chemistry. The primary focus of these designs will be the transient manipulation of the main shock since it the primary source of mass flux and hazard for a turbine section. The secondary and consequential focus will be the diffuser's effect on the high enthalpy blowdown process.

In general, a successful diffuser will accomplish four goals:

1) Attenuate the peak pressure of the leading shock.
2) Improve steadiness during the pulse event.
3) Elongate the pulse event.
4) Maintain the high availability of the blowdown process.

Design Process

Diffusers were developed using a four step design process. The first two steps, Concept Generation and Analytical Modeling/Detailed Design, are discussed in the current chapter. The last two steps, Computational Modeling/Evaluation and Diffuser Selection, are covered in the next chapter. A brief description of this process is as follows:

Chapter 3 (current):

Concept Generation – Concepts were generated as literature was reviewed and as a theoretical understanding was built. This process took place over a span of several months. Due to the novelty of this project, geometrically simple designs were selected to investigate possible pulse diffusion mechanisms.

Analytical Modeling, Detailed Design – Initial, analytical models were developed to augment understanding of the dynamics and to generate a geometric design envelope for the diffuser's key features. This step of the process required extensive study of unsteady, compressible flow topics such as shock reflection and refraction. This analysis estimates key timing and pressure attenuation parameters for each diffuser. Loss mechanisms were qualitatively considered but the effects of which were left unquantified.

Chapter 4 (next):

Computational Modeling, Evaluation – Unfortunately, due to the transient, un-steady nature of the problem, it was impossible to fully assess diffuser performance from hand calculations alone. To finalize performance estimates, designs were evaluated numerically using the commercial CFD code, ANSYS Fluent. These simulations are used to determine the overall efficacy of the intended diffusion mechanisms. They also provided estimates into several key performance metrics such as peak pressure attenuation, pulse elongation, steadiness, and availability preservation.

Diffuser Selection – Diffuser selection occurs in two stages. First, the optimal diffuser regime/type is selected based on the simulation results and other factors. Then, a specific design within the selected type is chosen for experimental investigation.

3.2 Concept Generation

As understanding of wave dynamics and compressible fluids dynamics improved, several concepts were generated. These concepts focused on geometric simplicity. Each design sought to employ a different pulse elongation mechanism in an effort to determine that which were effective. The three design concepts are summarized below.

Expansion Chamber Diffuser

This design uses a sudden area enlargement shortly followed by a sudden area reduction to create a series of pressure reflections which follow the initial decaying detonation wave. After the first enlargement, the shock partially reflects off the area reduction, and then re-reflects off the initial enlargement/reduction. This is a very simple design, essentially consisting of concentric, standard pipes which would provide the appropriate change in area. The initial area divergence attenuates peak pressure and series of reflections elongates the pulse event.

Diffraction-Reflection Diffuser

This design concept uses a diverging outlet to produce reflected disturbances intended to temporally distribute the energy carried by the decaying detonation front. The main shock will diffract at the corners of the diverging area and then reflect as the tube regains a constant area. The peak pressure is attenuated by the overall area change and the pulse is elongated by the reflection processes at the concave corners.

Bifurcating Duct Diffuser

This diffuser uses splitting flowpaths to divert and weaken the main shock. As the main shock meets the duct bifurcation, it diffracts and splits between the two ducts. After the initial bifurcation, different flowpath lengths stagger the arrival time of the shocks. This design attenuates peak pressure via the duct split and elongates the pulse by generating multiple shocks with delayed departure times.

3.3 Analytical Modeling, Detailed Design

The following section describes the detailed design process. A qualitative sequence of events, main geometric parameters, descriptions of pulse elongation and shock attenuation mechanisms, and discussion of loss mechanisms are given for each concept. With this process, basic analytical models are generated for each design in which timing parameters and overall pressure attenuation estimates are given. These models *do not* provide detailed, quantitative predictions of a diffuser's performance due to the temporally unsteady and spatially distributed processes involved with PDC operation. Instead, the analytical models yield simple metrics against which computational and experimental results can be compared. Further, these models mainly serve as tools used to drive the detailed design, allowing the author to select appropriate

values for a given geometric feature. The efficacy of a diffuser or diffusion mechanism can only be fully assessed with a computational effort.

To aid in analysis, many assumptions were made to simplify this complex, transient system. The assumptions used include:

- The detonation front will be a planar, spatially zero-dimensional discontinuity with ideal CJ properties such as wave speed, pressure, and temperature.
- The detonation front will be followed by an ideal Taylor Wave which isentropically expands and decelerates the detonation products to meet the back-wall conditions.
- Flow through expansion waves and area changes will be isentropic.
- The detonation will diffract into air with $\gamma = 1.4$.
- All gases will be treated as perfect gases.

Expansion Chamber Diffuser

Overview

Figure 3.1 illustrates a qualitative time sequence of events describing the expansion chamber diffuser. After traveling down a length of inert tube, the incident shock meets the area divergence and creates two transmitted shocks. The more downstream of these shocks partially reflects from the area divergence, and then re-reflects from initial area divergence. It then propagates toward the exit. Also note the contact surface in Figure 3.1 which separates shocked air and the detonation products. The ideal diffuser will generate the reflected waves before the contact surface reaches the expansion chamber. In this design, the initial divergence attenuates the peak pressure of the lead shock and the subsequent reflections aim to elongate the pressure event.

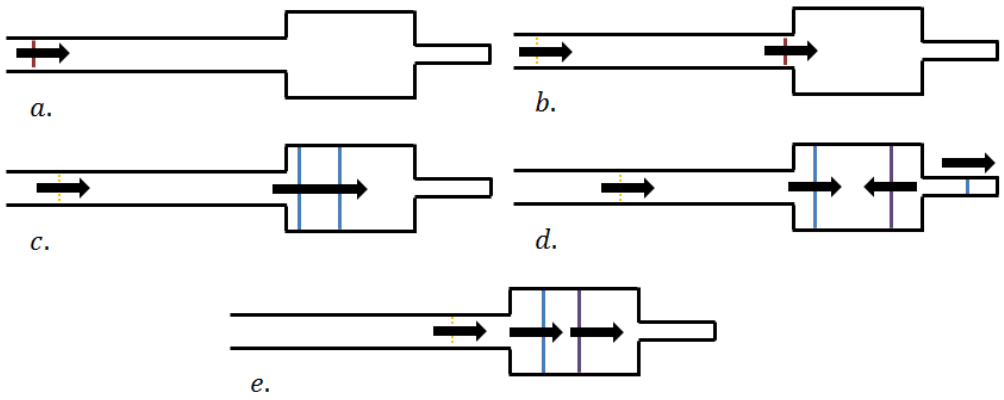

Figure 3.1. Time sequence of events of the expansion chamber diffuser. a) and b) Incident wave travels down the run up tube c) Incident wave meets area divergence and produces two transmitted shocks d) First transmitted wave transmits and reflects e). Reflected wave re-reflects and moves toward exit

A generic expansion chamber diffuser is shown in Figure 3.2. As noted in the diagram, the main design points are $L_{run}, L_{chamb}, \alpha_1$ and α_2. L_{run} is the length of pipe leading up to the chamber and dictates the distance between the leading shock and the detonation product contact surface behind it. Separating the expanding detonation products from the lead and reflected shocks is critical in preventing the detonation products and shocked air from mixing. Such mixing exacts a large penalty with regard to entropy generation and availability destruction. The area ratios, α_1 and α_2, determine the strengths of the transmitted and reflected shocks which will be discussed in the upcoming section. L_{chamb} is the length of the expansion chamber.

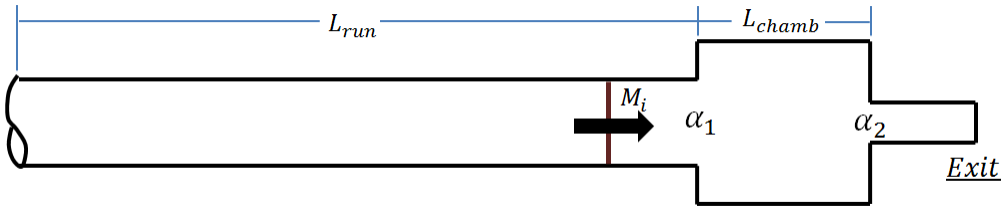

Figure 3.2. The main geometric features of a generic expansion chamber diffuser.

Pulse Elongation and Leading Shock Attenuation Mechanisms

The problem of a planar shock meeting a sudden area change can be treated as a quasi-one dimensional problem. The process of solving for the predicted flow field is known as Rudinger's Method [35,36,39]. With this method, one guesses what the expected self-similar flow field will be for a given area change, α, and incident shock strength, M_i. As discussed in the refraction analysis, the physical possibility of this flow field is checked against a solution criterion. In most cases, the flow field is correct if the contact surface condition is met.

Rudinger's method provides a prediction for the flow solution in whole, and does accommodate any time resolution or description of intermediate features [39].

For a strong shock meeting a sudden area divergence ($\alpha < 1$), the solution of interest is shown in Figure 3.3. Although many solutions are possible for a given diverging area ratio and shock strength, this flow field is the most probable in this application since decaying detonations are often stronger than $M_i = 2.068$ [39]. As shown in the figure, the incident shock results in two transmitted shocks. The more downstream transmitted shock, M_{t1}, is a conventional shock which is weaker than the initial shock i.e. $M_{t1} < M_i$. The second transmitted shock, M_{t2}, is a backward facing shock. As the flow isentropically expands through the area change (region 2 to 5), the pressure and velocity both rapidly decrease. In order to meet the post-shock conditions of M_{t1}, this backward facing shock forms and increases particle speed and pressure so that it can match that of the main transmitted shock (region 5 to 4). This flow which expanded through the area change and passed through M_{t2} is separated by the flow induced by M_{t1} by the contact surface.

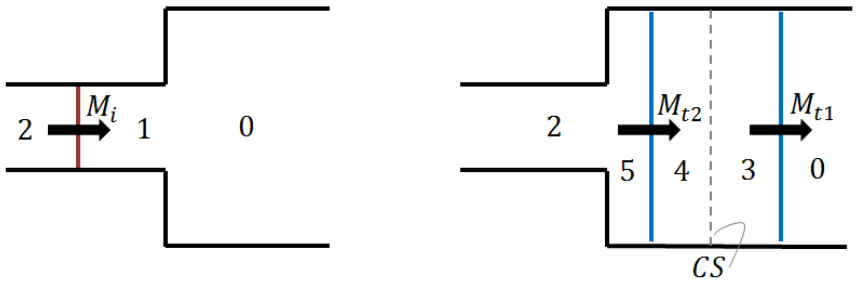

Figure 3.3. A strong shock (M_i > 2.068) meeting an area divergence ($\alpha < 1$).

As before, a shock meeting a sudden area contraction ($\alpha > 1$) can generate numerous flow solutions. For this particular case, we are interested in the solution which results in a reflected shock. This solution occurs for larger values of α and where $M_i' > 2.068$ [39]. Figure 3.4 illustrates the features of this flow. This diagram assumes that the area contraction follows an area divergence, so that $M_i' = M_{t1}$. The reflected shock, M_r, decelerates the flow to subsonic conditions as it approaches the area contraction (region 3 to 6). Assuming isentropic flow, the flow is then accelerated to a choking point (region 6 to 7), and then further accelerated by an expansion wave to meet the pressure and velocity conditions upstream of the transmitted shock,

M_{t3} (region 7 to 8). The flow passing through the area change is separated by the flow induced by M_{t3} by the contact surface.

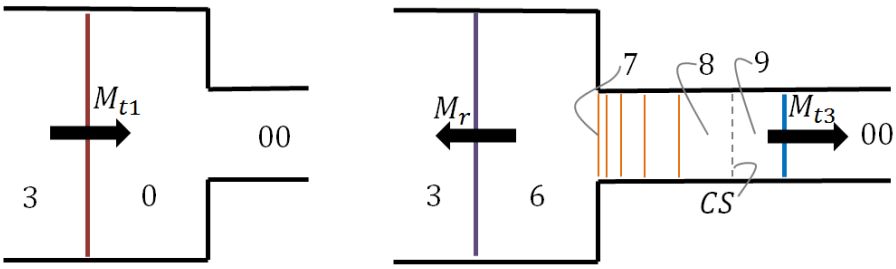

Figure 3.4. A strong shock (M_{t1} > 2.068) meeting an area contraction ($\alpha > 1$).

Detailed Design

In order for a shock to reflect off of the area contraction of the expansion chamber, M_{t1} must produce supersonic post-shock flow and the area ratio must be sufficiently large. As such, M_{t1} > 2.068 and M_3 > 1.05. The strength of M_{t1} is determined by the incident shock strength, M_i, and the area divergence ratio, α_1. In this application, the incident shock strength is dependent on run up duct length to the chamber. As discussed, the leading shock front is continually weakened by the remnants of the Taylor Wave as both travel down the inert section of the tube. Estimates for the value of M_i were made based on L_{run} and from experimental data, partial fill data.

Figure 3.5 is a plot of the first transmitted shock strength, M_{t1}, over a range of $\alpha_1 < 1$ for $M_i = 2.75, 3.0, 3.25$. As shown in this plot, M_{t1} strongly increases over the range of α_1 for all M_i. Inspection of this plot as indicates that all incident strengths are approaching a limiting value of $M_{t1} = 1$ as $\alpha_1 \to 0$. That is the shock degrades to a Mach wave as it is transmitted to an unconfined volume. Regardless, values of $\alpha_1 < 0.3$ produce a transmitted shock weaker than the required threshold strength of $M_{t1,\min} = 2.068$. Thus, area divergences $\alpha < \alpha_{1,min} = 0.3$ can be eliminated from consideration. The upper limit of the area divergence, $\alpha_{1,max}$, must be selected knowing that the this feature must also act the re-reflection area convergence, $\alpha_3 = {\alpha_{1,max}}^{-1}$. With this in mind, we will select $\alpha_{1,max} = 0.8$, meaning $\alpha_{3,min} = 1.25$.

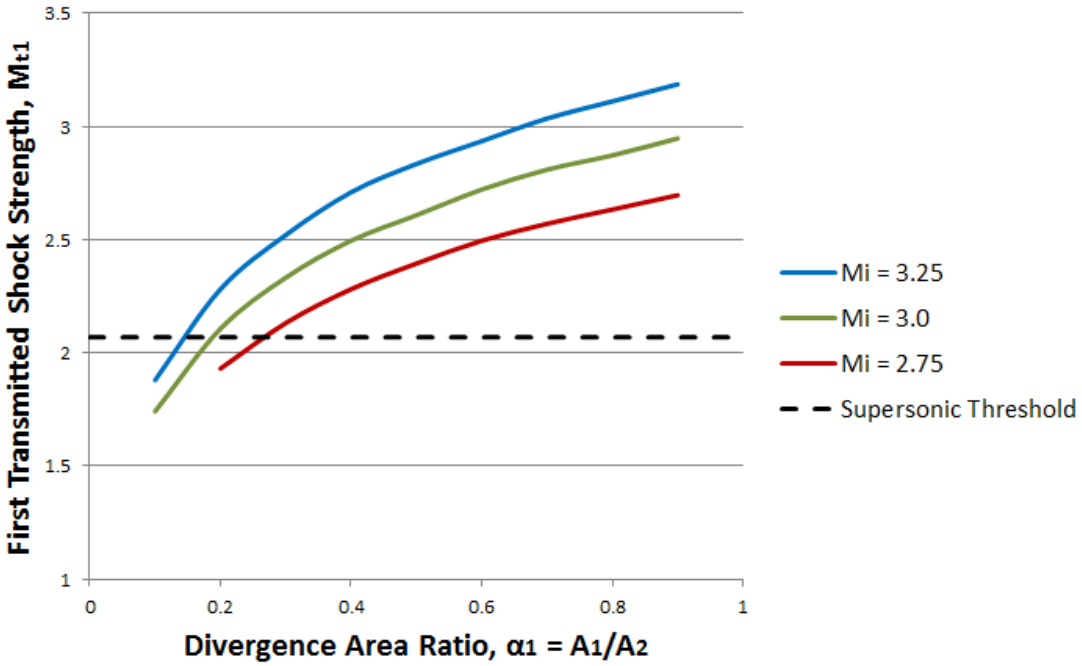

Figure 3.5. First transmitted shock strength, M_{t1}, vs. divergence area ratio, α_1.

Now let us turn our attention to the area contraction. Figure 3.6 is a plot of the third transmitted shock strength M_{t3} versus area convergences $\alpha_2 > 1$ for $M_{t1} = 2.1, 2.6, 3.1$. Similar to before, M_{t3} increases with α_2 for all M_{t1}. In all cases, the transmitted shock strength is demonstrating a negative concavity with respect to area ratio. Unfortunately, this plot does not provide much insight with regard to selecting an area contraction.

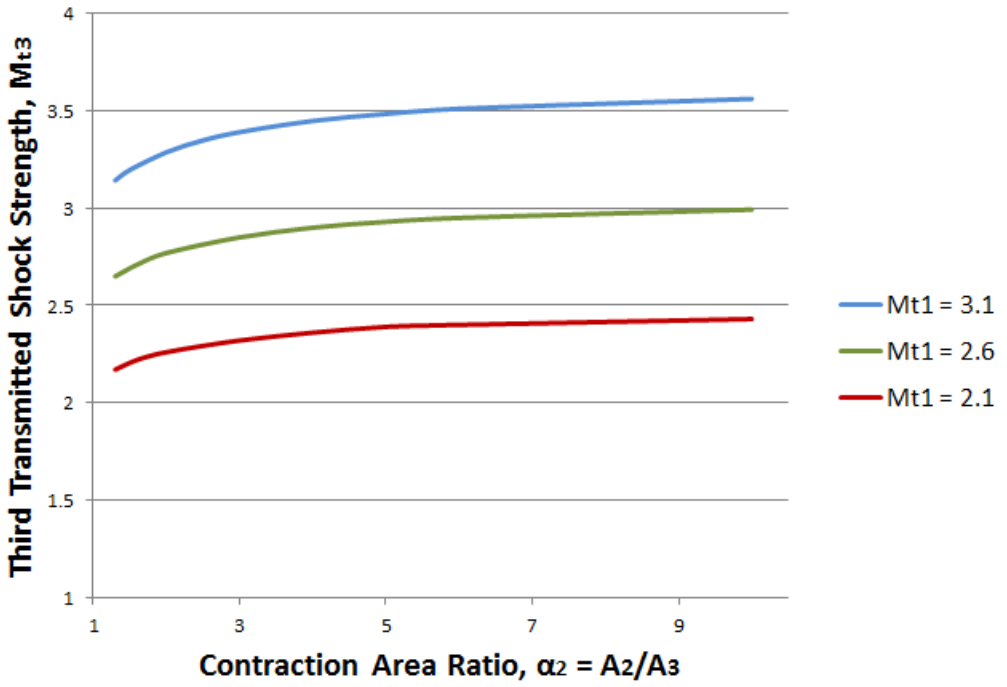

Figure 3.6. Third transmitted shock strength, M_{t3}, vs. divergence area ratio, α_2.

To aid in selecting an area contraction, a useful parameter to introduce is the entropy generation ratio, ζ. This parameter measures the entropy generated by the reflection event at the area contraction. The entropy generation ratio is defined as

$$\zeta \equiv \frac{\dot{m}_{r1} * \Delta s_{r1} + \dot{m}_{t3} * \Delta s_{t3}}{\dot{m}_{t1} * \Delta s_{t1}}, \qquad \textbf{3.1}$$

where $\dot{m}$ is mass flow rate of the respective wave and Δs is the specific entropy change caused by the respective wave. The mass flow can be computed by

$$\dot{m} = \rho * A * U, \qquad \textbf{3.2}$$

where ρ is the density of downstream medium relative to the shock wave, A is the area of the duct and U is the velocity of the gas entering the shock relative to the shock wave. Entropy gain across a shock wave can be computed by

$$\Delta s_{A\to B} = c_p \ln\left(\frac{T_B}{T_A}\right) - R \ln\left(\frac{P_B}{P_A}\right), \qquad \textbf{3.3}$$

where T is temperature, P is pressure, $c_p = \frac{\gamma R}{\gamma - 1} = const$ and $R = R_u / MW_{air}$.

Entropy generation as a function of area contraction ratio, α_2, and first transmitted shock strength, M_{t1}, is shown in Figure 3.7. As is shown in the figure, an area contraction increases entropy generation, meaning $\zeta > 1$ in all cases. Also shown in this figure as the dashed lines are the theoretical limits of the entropy generation ratio corresponding to a regular reflection, that is as $\alpha_2 \to \infty$. The maximum entropy generation demonstrates a definite negative concavity with respect to incident shock strength. Note the peculiar result that $\zeta_{max}|_{Mt1=2.6} > \zeta_{max}|_{Mt1=2.1}, \zeta_{max}|_{Mt1=3.1}$. In terms of narrowing the design envelope, the author chose to investigate contraction area ratios corresponding with approximately half the maximum gain in entropy, that is $\zeta \approx 1.3$ where $\zeta_{max} \approx 1.6$. To achieve this, contraction area ratios in the range of $3 < \alpha_2 < 5$ will be investigated.

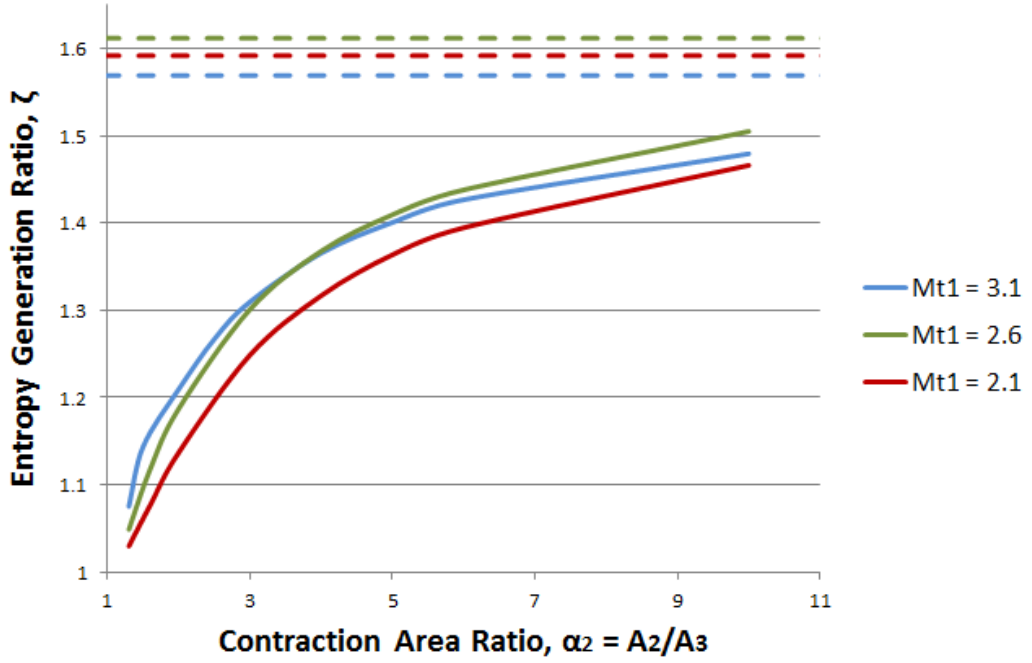

Figure 3.7. Entropy generation ratio, ζ, vs. contraction area ratio, α_2.

A wave diagram summarizing the reflection process is shown in Figure 3.8. At this point in the analysis, the behavior in the re-reflection process is unknown. Predicting the interaction between M_r and M_{t2} exceeds the accuracy of this idealized one-dimensional analysis. Although the efficacy of this diffuser hinges on this re-reflection event, the nature of the re-reflection can only be determined through computational studies. Because of this, no estimates with regard to reflection delay times can be accurately be given.

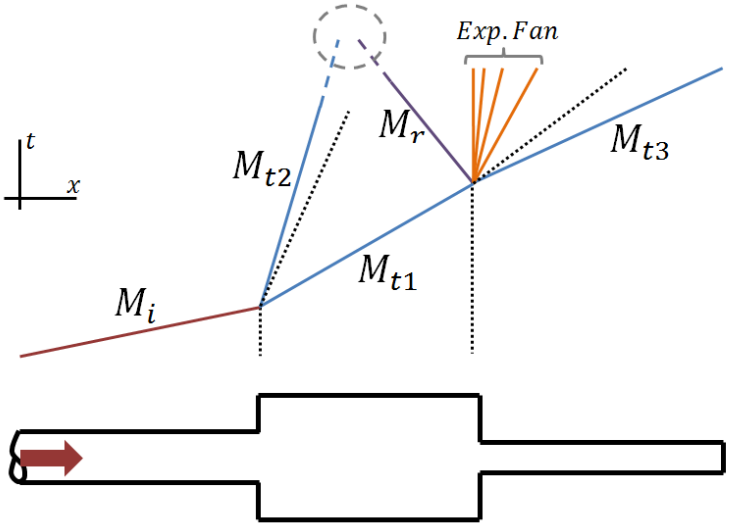

Figure 3.8. Qualitative wave diagram of the expansion chamber diffuser reflection process.

Using this analysis, an iterative design scheme was employed to investigate the effects of the different geometric parameters. The incident shock strength, M_i, was selected for each design based on experimental measurements and the value for L_{run}. The first three iterations seek to investigate the effect of L_{run} on the diffuser performance. This parameter affects both the incident shock strength, losses due to mixing and also blowdown time. The last of these designs will choose the optimal run up length and looks at a different set of area ratios. The design iterations are summarized in Table 3.2. This table suggests that the leading shock attenuation may be independent of the run up length. The pressure attenuation given in this table does not account for natural effects of the Taylor Wave. As such, real attenuation values will be greater than the estimates provided. Also note that area ratios were chosen based on standard pipe sizes to observe manufacturability requirements.

Table 3.1. Geometric parameter ranges for the expansion chamber diffuser. Estimates for the peak pressure attenuation likely underestimate actual attenuation due to the neglected effects of the Taylor Wave.

Iteration	L_{run} *[cm]*	M_i	α_1	α_2	P_{max}/P_{CJ}
1	39.4	3.25	0.284	5.44	0.477
2	106.7	2.75	0.284	5.44	0.344
3	76.2	2.9	0.284	5.44	0.380
4	*Optimal*	--	0.519	4.83	--

Discussion of Loss Mechanisms

Despite its simplicity, the expansion chamber diffuser presents several sources for availability destruction during the Pulse Detonation cycle. Let us first focus on the sudden area expansion. Such an expansion will promote shear and vortical losses and also promote mixing between the detonation products and shocked air. The backward-facing shock, M_{t2}, is a flow feature which will also serve a point of entropy generation.

The area contraction is also a source for irreversibilities in this system. As illustrated in Figure 3.7, a reflected shock necessarily will increase the entropy generated in this system. Whether or not these reflected waves affect the detonation products is dictated the run up length to the expansion chamber, L_{run}. A sufficiently long run-up distance will provide a large enough gap between the main contact surface and the leading shock. This gap acts as a sort of "cushion" in which the reflected phenomena can propagate in shocked air without refracting into the detonation products. However, as discussed in Section 2.5, natural expansion due to partial filling also serves as a point of irreversibility. Hence, it is crucial to use a minimum value for the run up length to prevent unnecessary losses.

Diffraction-Reflection Diffuser

Overview

A qualitative sequence of events for this diffuser is given in Figure 3.9. As the shock enters the diffuser, it meets the top ramp and begins to diffract around the convex corner. Soon after, this portion of the shock meets the concave corner and generates a reflected disturbance. A similar sequence of events takes place for the bottom ramp. Overall, the reflected disturbances seek to elongate the pulse event and the overall area change attenuates the leading shock.

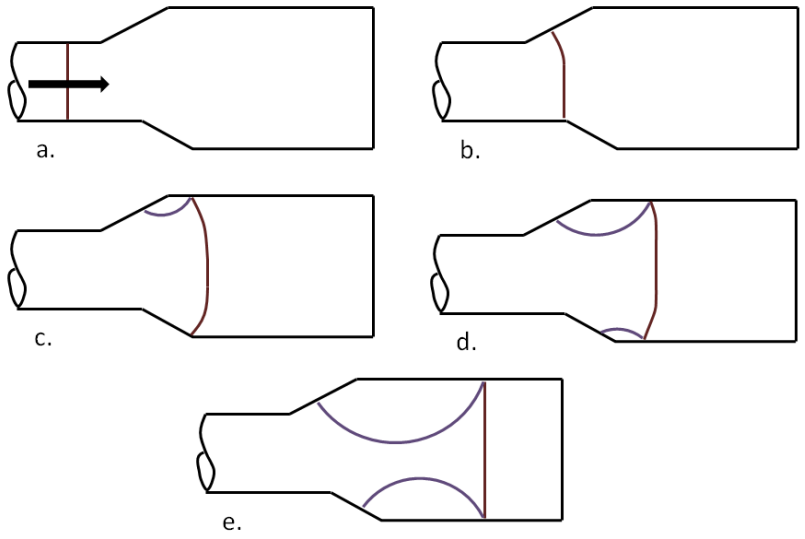

Figure 3.9. Qualitative time sequence of the diffraction-reflection diffuser. a) Shock enters b) Top ramp diffraction c) Top ramp reflection d) Bottom ramp diffraction e) Bottom ramp reflection f) End propagation

The key geometric features of a generic diffraction-reflection diffuser are highlighted in Figure 3.10. These features are the diffraction/reflection angles, θ_1 and θ_2, ramp lengths, L_1 and L_2, ramp stagger, Δx, final length, L_3. Using these features, one can define three different regimes of diffuser: single reflection ($\theta_2 = 0$), simultaneous double reflection ($\Delta x = 0$), and staggered double reflection ($\Delta x \neq 0$). The staggered regime is intended to delay the creation of the reflected disturbances the most. In this design, the diffraction angles are assumed to be the same as the reflection angles for each ramp. The length and angle of each ramp dictates the delay between pulses and the overall area ratio dictates the peak pressure attenuation.

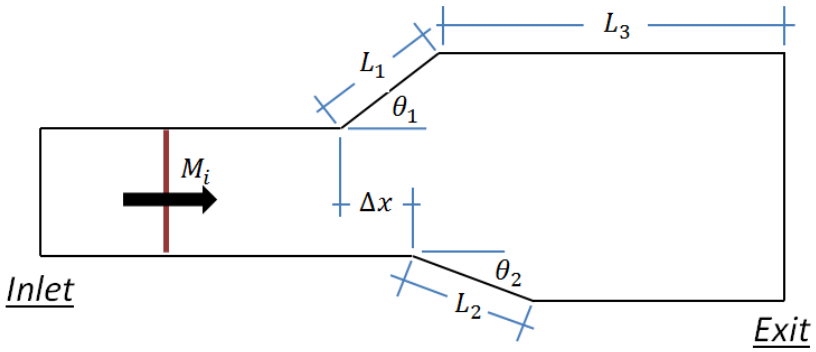

Figure 3.10. Generic diagram of Diffraction-Reflection Diffuser.

Pulse Elongation Mechanism

The diffraction-reflection diffuser seeks to elongate the pressure pulse by generating reflected disturbances at concave corners. This mechanism consists of initial diffraction around a convex corner followed by the reflection of the shock at the end of the area change.

The nature of a non-stationary, planar shock diffracting around a sharp, convex corner has been the study of many researchers [40,41]. An illustration of this event is shown in Figure 3.11. The shock shape and propagation dynamics are dependent only on the corner angle, θ', and the incident shock strength, $M_0{}'$. In essence, as the shock reaches the corner, it generates pressure disturbances which propagate radially at the local speed of sound, a_1, with the propagation center moving at the local particle velocity, v_1. These disturbances, or characteristics, serve to change the shape of the shock in a region near the wall and decrease the wave speed in this same region. The wave speed at the wall is $M_w < M_0{}'$.

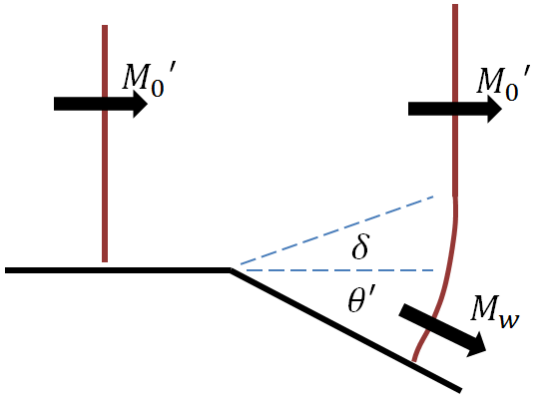

Figure 3.11. Shock diffraction around a sharp, convex corner.

Similar to diffraction, the nature the reflected shock is dependent on the angle of the ramp, θ, and the strength of the incident shock, M_0. A brief overview is provided here, but many texts detail this complex event [36,42,43]. As illustrated in Figure 3.12, reflected pressure disturbances are generated once the shock meets the ramp. The disturbances propagate radially at the post-shock speed of sound, a_1, with the propagation center travelling at the post-shock particle speed, v_1. For shocks where the post-shock products are sub-sonic ($M_i < 2.068$), the disturbance is entirely circular (as in Figure 3.12). For shocks where the post-shock products are supersonic ($M_i > 2.068$), the disturbance is circular near the point where it attaches to the main shock [44].

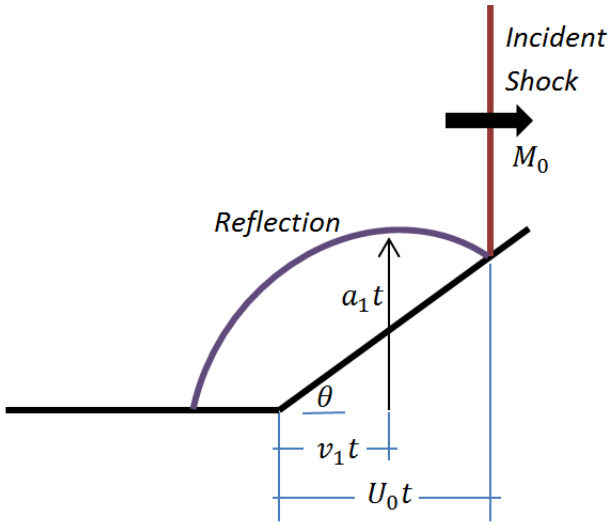

Figure 3.12. Shock reflection at a sharp, concave corner where M_0 < 2.068.

Leading Shock Attenuation Mechanism

As discussed in the expansion chamber diffuser section, the flow solution to a shock meeting an abrupt area change can be estimated using Rudinger's Method. The area change in this diffuser, although not instantaneous, may still be considered discontinuous and abrupt. As such, one can expect the same flow solution illustrated in Figure 3.3. Lead shock attenuation will occur as the shock passes this diffuser and can be estimated the total area ratio, α.

Detailed Design

If one assumes a planar shock enters the diffuser, and the diffuser geometry is specified, one can reasonably predict the propagation of the reflected disturbances. As the incident shock meets the first convex corner of the top ramp, the strength of the shock weakens to M_{w1} along L_1. The shock travels along the top ramp until it meets the concave corner, where a reflection begins to propagate. One can approximate the center velocity and radial velocity of this reflection by considering the post-shock velocity and speed of sound caused by a shock of strength M_{w1}. This is an approximation since the strength of the shock meeting the "ramp" will be constantly changing. A similar approach can be used to model the disturbances along the bottom of the duct.

One can treat the diffraction and reflection of each wedge as independent events as long as the steepest characteristic lines do not intersect. The steepest characteristic indicates the point

on the incident wave where wave shape begins to curve, as shown in Figure 3.11. The angles of these characteristics, δ, will be the same for each ramp and depends only on the incident shock strength, M_i [40]. The time at which these characteristics intersect, t_{char}, can be estimated by the equation

$$t_{char} = \frac{\Delta x + [\frac{D_i}{2} * \tan\delta - \frac{\Delta x}{2}]}{M_i a_0}, \quad \textbf{3.4}$$

where Δx is the stagger between ramps, D_i is the diameter of the inlet pipe, δ is the angle of characteristic, a_0 is the ambient speed of sound, and M_i is the incident shock strength. The incident strength is assumed to be constant through this process. This is an idealization of the real physics since the decaying detonation/shock front continually weakens as it travels along the inert section of the tube.

The transit times for each ramp are defined as the time taken for the shock to travel from the first convex corner on the top ramp to the respective concave corners. The top ramp, ramp 1, is always stipulated to start first whereas the bottom ramp, ramp 2, starts at the same point (simultaneous, $\Delta x = 0$) or some distance after (staggered, $\Delta x \neq 0$). The transit times for ramp 1 and ramp 2 can be estimated by

$$t_1 = (M_{w1} * a_0)^{-1} * L_1 \quad \textbf{3.5}$$

and

$$t_2 = (M_i * a_0)^{-1} * \Delta x + (M_{w2} * a_0)^{-1} * L_2. \quad \textbf{3.6}$$

In order for the diffraction processes for each ramp to be considered independent, the transit times must satisfy the condition $t_{char} > t_1, t_2$. In addition, the delay between the start of the reflected disturbances can be estimated by

$$t_{delay} = t_2 - t_1. \quad \textbf{3.7}$$

Using this logic, a MATLAB code was generated which plotted parametric diagrams illustrating predicted shock and reflection propagation for a given incident shock strength and geometry. An example of an output plot is shown in Figure 3.13. For the purpose of this analysis,

the incident shock strength was assumed to be $M_i = 3.0$. This assumption is based on experimental measurements and analytical estimates from the refraction analysis.

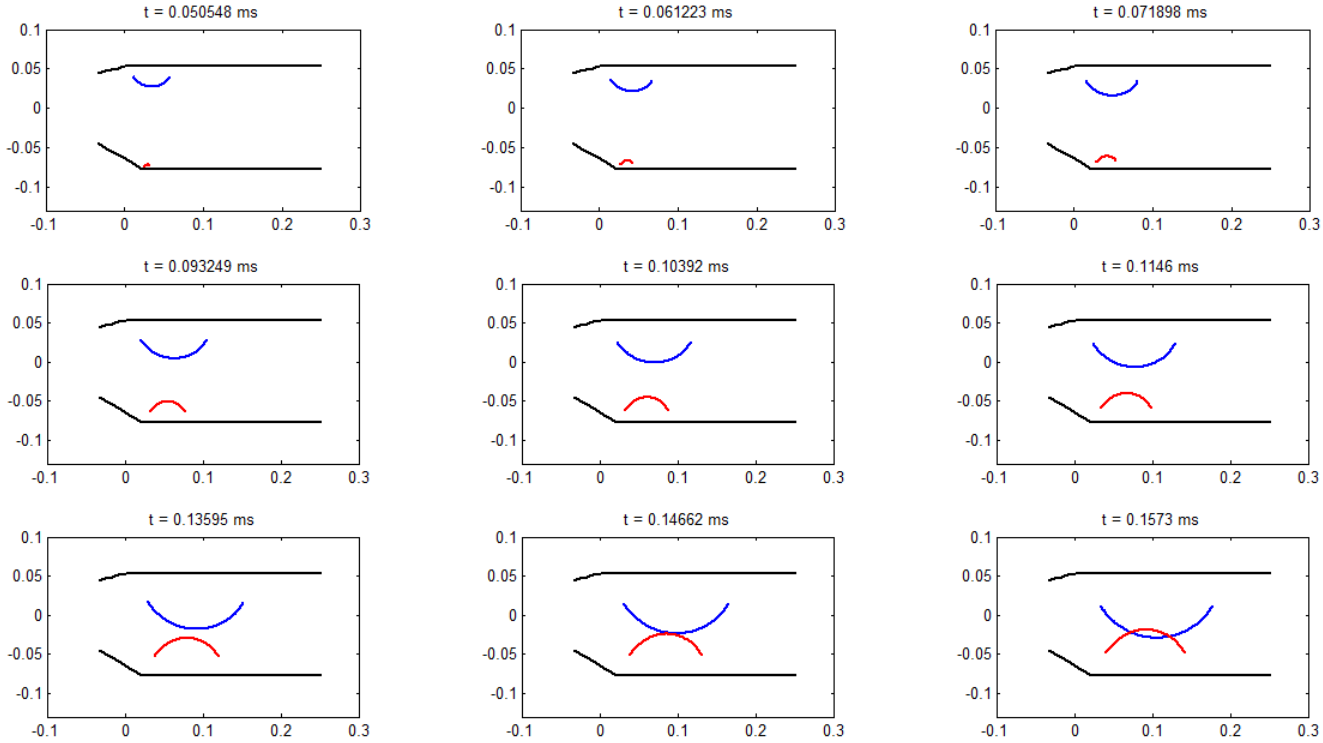

Figure 3.13. Example plot from the Diffraction-Reflection visualization code.

The overall area divergence provides insight into the peak pressure attenuation this diffuser provides. The overall area divergence is computed by

$$\alpha = \frac{A_1}{A_2} = \frac{D_1}{D_1 + L_1 \sin\theta_1 + L_2 sin\theta_2} \qquad \textbf{3.8}$$

where D_1 is the diameter of duct leading into the diffuser. For this study, this diameter will be the inside diameter of a NPS 3" Schedule 40 Pipe, meaning D_1= 3.068 inches = 7.79 cm. Using Rudinger's Method, one can approximate the transmitted shock strength and peak pressure attenuation due to the area divergence. Note that the attenuating effects of the Taylor Wave are not considered in these estimates. As such, the author expects that simulated attenuation to be greater than the analytical estimates given here.

Using this methodology, six different geometries were selected for numerical investigation. Since the focus of this study was the nature of the reflected disturbances, the

transmitted shock strength was not sensitive to the geometries selected since the overall area divergence varied slightly. With respect to pulse elongation, more drastic designs estimate a larger delay between the reflection initiations. Table 3.2 summarizes the geometries, time delays and pressure attenuation, P_{max}/P_{CJ}, for each design. The delay between reflection initiations was not large for any cases, suggesting that this design may only provide slight pulse elongation. The pressure attenuation estimates do not account for natural attenuation caused by the Taylor Wave. As such, one can expect greater attenuation in a computational model.

Table 3.2. Design summary for diffraction-reflection diffuser. Estimates for the peak pressure attenuation likely underestimate actual attenuation due to the neglected effects of the Taylor Wave.

Design	*Regime*	t_{delay} *[ms]*	P_{max}/P_{CJ}
1	Simult. ($\Delta x = 0$)	0.054	0.477
2	Simult. ($\Delta x = 0$)	0.058	0.448
3	Simult. ($\Delta x = 0$)	0.062	0.441
4	Stag. ($\Delta x \neq 0$)	0.062	0.486
5	Stag. ($\Delta x \neq 0$)	0.070	0.485
6	Stag. ($\Delta x \neq 0$)	0.089	0.481

Discussion of Loss Mechanisms

As with the expansion chamber diffuser, the overall area divergence serves a serious source of irreversibility in the system of interest. Although the area change in this design is not instant, supersonic flow through the divergence will still create a backward-facing shock. As discussed previously, this shock is a source of entropy generation and availability loss. Also, the overall area divergence will also promote mixing between detonation products and shocked air.

Bifurcating Duct Diffuser

Overview

A qualitative sequence of events for a generic bifurcating duct diffuser is shown in Figure 3.14. In this diffuser, the leading shock meets the duct branch and begins to diffract along the area divergence. The lead shock then splits into two weaker shocks which travel down separate ducts and exit the diffuser at staggered times. The shocks weaken as they transit their respective tubes.

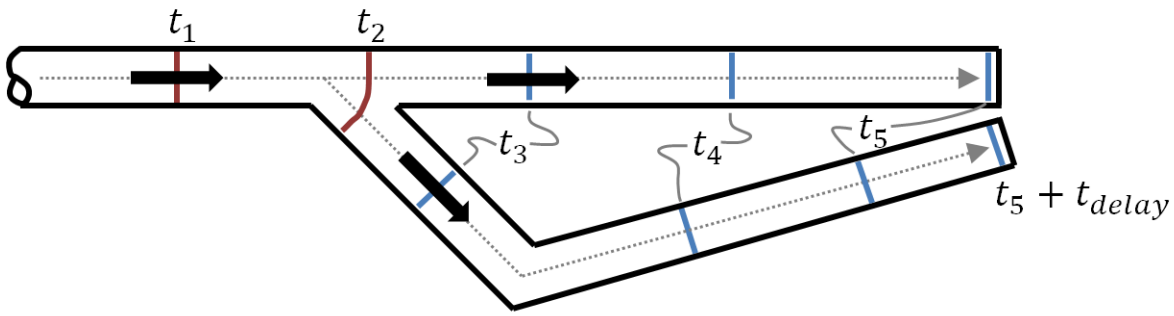

Figure 3.14. A qualitative time sequence of events for the bifurcating duct diffuser.

Figure 3.15 illustrates potential generic diffusers to be considered for this design, with a). a true wye bifurcation, b). a lateral wye bifurcation, c). a lateral tee bifurcation. In the interest of simplicity, only a single flowpath bifurcation will be investigated, although it could be possible to bifurcate the duct multiple times. As the illustrations indicate, the main parameters to be determined will be the duct path lengths, L_1 and L_2, and the type of bifurcation. The type of bifurcation dictates the initial strengths of the resultant shocks in each duct. For example, a true wye will generate shocks of equal strength in each duct, whereas a lateral wye or lateral tee will generate shocks of unequal strength. The selection of bifurcation type is important when estimating the stagger between shock exit times and also when considering design for manufacture. Similarly, the path length also dictates staggering between pulses. As will be quantified, the strength of the shock weakens as it travels down the tube. In each of these examples, the ducts are directed to the same local exhaust region.

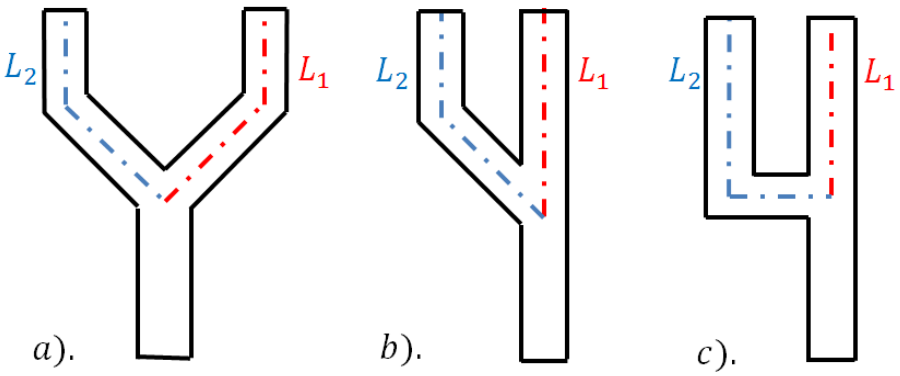

Figure 3.15. Generic bifurcating duct diffusers illustrating important geometric features, specifically bifurcation type and path lengths.

Pulse Elongation and Leading Shock Attenuation Mechanisms

With this concept, pressure pulse elongation is achieved by splitting the lead shock and staggering the exit of the resulting shocks. The initial bifurcation and subsequent transit serve to attenuate the peak pressure compared to incident wave.

The propagation of shocks in channels is of particular interest to safety engineers and major concepts are covered in a review text [36]. The strength of the shocks in the bifurcated ducts can be determined by considering the geometry of the bifurcation and the incident shock strength. Considering a 2-dimensional event shown in Figure 3.16, the incident shock, M_i, diffracts as it meets the bifurcation. Without discussing mathematical rigor, the shock-induced energy increase of the diffracted shock at extent A is equal to the energy increase of the resulting shocks, M_{t1} and M_{t2}, in each branch. To aid in convenience, one may assume that no energy is lost due to viscous effects as the shock splits. This conservation of energy approach may be applied to any bifurcation geometry for any incident strength.

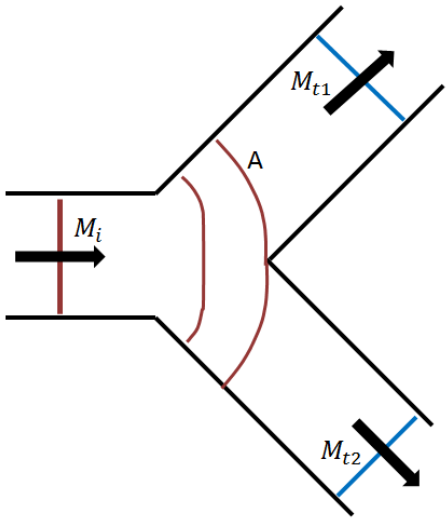

Figure 3.16. A planar shock meeting a channel bifurcation. The shock diffracts as the area diverges and then splits into two transmitted waves.

Heilig and Igra graphically summarized the results from these calculations for a number of bifurcation types (true wye, lateral wye, four-way tee, lateral tee) over a large range of incident shock strengths ($1 < M_i < 9$). The analytical results are compared against experiments with good agreement, especially for weaker incident shocks. In general, the analytical estimates overestimated transmitted shock strengths, with the overestimation becoming more egregious for stronger incident shocks [36]. Hammit and Carpenter added a loss term which provided

additional accuracy when computing the resulting shock strengths in each channel; however, they did not elaborate the basis of this term [45].

Discussed previously, the remnants of the Taylor Wave from the detonation event continually weaken the leading shock as it travels down the inert section of the tube. This expansion wave naturally attenuates the leading shock and also plays a key role in this diffuser concept with regard to timing.

Detailed Design

We will begin by selecting the type of bifurcation to investigate. Considering loss potential and design for manufacturability, the lateral wye has been chosen as the ideal branching type. This type of branching generates unequal resultant shocks which will aid in the pulse elongation process compared to a true wye. Also, the work from Heilig and Igra imply that a lateral wye suffers fewer viscous losses than a lateral tee [36]. As shown in Figure 3.17, shock which is transmitted through the straight portion of the lateral will be the main shock, M_m, and the shock which is transmitted through the branch will be termed the secondary shock, M_s. Because of the asymmetry of the shock diffraction, the transmitted shock strengths will be unequal such that $M_m > M_s$ for all M_i.

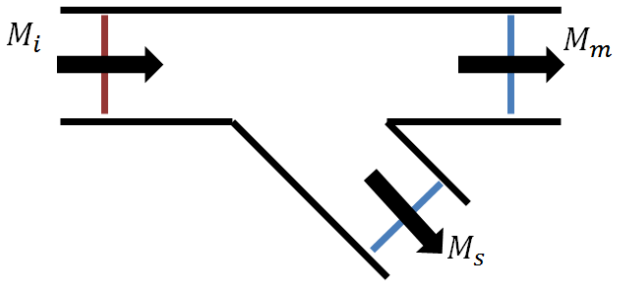

Figure 3.17. Diagram of the lateral wye bifurcation, including wave labeling convention.

For weaker incident shocks ($PR_i < 15,\ M_i < 3.5$), we can estimate the initial transmitted shock pressure ratios as

$$PR_{m,0} = 0.896 * PR_i + 0.104 \quad \textbf{3.9}$$

and as

$$PR_{s,0} = 0.52 * PR_i + 0.48 \quad \textbf{3.10}$$

where PR_0 is the initial static pressure ratio across the respective shock wave. These linear relationships were graphically inferred from the summary plot provided by Heilig and Igra [36]. Note that these are distinguished as "initial" pressure ratios since the Taylor Wave will attenuate the transmitted shocks as they travel out toward the exit. Using Equations 3.9 and 3.10, one can compute the initial transmitted shock strengths by

$$M_0 = \sqrt{(PR_0 - 1)\frac{\gamma + 1}{2\gamma} + 1.} \quad \textbf{3.11}$$

Note that this formula is just an algebraic rearrangement of Equation 2.8. Using the definition of Mach Number, we can compute the initial wave speed by $U_0 = M_0 * a$, where a is the speed of sound of the downstream medium. In this case, the downstream medium is air and the speed of sound is assumed to be $a = 343$ [m/s].

Let us estimate the natural attenuation of the shock along the duct using an exponential decay model taking the form of

$$U(x) = U_0 * e^{-A(x - x_0)} \quad \textbf{3.12}$$

where x is the linear displacement of the shock along the duct centerline, U_0 is the initial wave speed, A is the decay rate, and x_0 is the initial linear displacement from the assumed origin. While Equation 3.12 is not derived from physical principles, an exponential curve fits both experimental and computational wave speed measurements with high correlation. These results will be discussed further in Chapter 3 of this paper. Taking from the experiments and simulations, we will use decay rates $A_{exp} = 0.00393$ [1/cm] and $A_{CFD} = 0.00309$ [1/cm] for both the main and secondary shocks in the present analysis. Integrating Equation 3.12, one can compute the transit time of the wave along a duct using

$$t_{duct} = \frac{1}{U_0 * A}\left[e^{A(L - x_0)} - 1\right] \quad \textbf{3.13}$$

where L is the total length of the duct along the centerline and τ is the transit time [46]. Note that Equation 3.13 does not account for the reflection events at the duct elbows in the secondary branch.

Consider the centerline paths of a diffuser shown in Figure 3.18. In this analysis, the origin of the linear displacement is considered to be the centerline intersection between the main and secondary branches. First let us assume that $x_0 = 0$. Under this assumption we are stipulating that the incident shock instantly splits at the origin, which is physically not the case. This assumption would lead to overestimating transit times, pulse exit delay, and overall attenuation. Instead let us assume that the initial position is some distance from the centerline intersection. This assumption is physically more realistic since it accounts for the diffraction and splitting of the incident shock. For the purpose of this analysis, we will assume that the initial position for each shock corresponds to the centerline extent of a standard lateral. In this case, the lateral to be used will be an NPS 3" standard wye lateral, meaning $x_{0,m} = 7.75" = 19.7$ [cm] and $x_{0,s} = 8.5" = 21.6$ [cm].

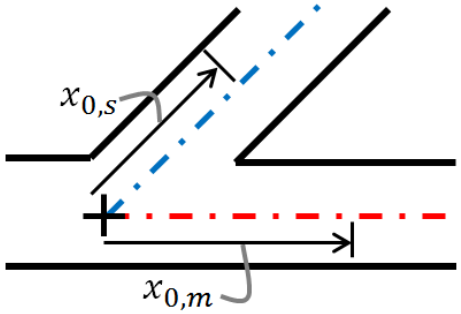

Figure 3.18. Diagram showing the origin of centerline displacement for the bifurcating duct analytical models.

As with the other design concepts, emphasis was placed on investigating physically feasible geometries. To this end, a MATLAB code was generated to compute physical geometric parameters which account for the finite size of the lateral and pipe to be used. Using standard wye lateral dimensions, the code provided useful parameters such as total centerline distances, physical pipe lengths, and pipe miter angles. For this analysis, the author chose to investigate the effects of the secondary to main path length ratio, $L_{s,tot}/L_{m,tot}$, while keeping the secondary path length constant, $L_{s,tot} = const$. As this ratio approaches unity, one can expect no stagger

between pulses. This ratio is also an indicator of the acuteness of the elbow in the secondary duct.

In the end, two bifurcating duct diffusers were selected for numerical investigation. These designs and their estimated performance are summarized in Table 3.3. The incident shock strength was based on experimental estimates and chosen to be $M_i = 3.0$. The first design employs a smaller length ratio ($\frac{L_{s,tot}}{L_{m,tot}} = 1.16$) compared to the second ($\frac{L_{s,tot}}{L_{m,tot}} = 1.40$). Stagger between pulses, t_{delay}, differed from Design 1 to Design 2 by approximately $t_{delay} \approx 0.1$ [ms]. Considering the slow decay and the relatively small differences in duct length, this small difference is not surprising. The author anticipates that these delay estimates will underestimate computationally determined delay times since the present model does not account for secondary shock attenuation at the duct elbow. The analysis suggests that this design could provide substantial peak pressure attenuation. Note that these attenuation estimates account for both the splitting and subsequent weakening during transit. Also note the performance estimates for each decay rate are given and only differ slightly, once again owing to the relatively small differences in duct length from Design 1 to Design 2.

Table 3.3. Design summary for the bifurcating duct diffuser. Performance estimates given for decay rates observed experimentally and numerically. Pressure attenuation accounts for the effects of the bifurcation and subsequent weakening during transit.

Design	$L_{s,tot}/L_{m,tot}$	$L_{m,tot}$ *[cm]*	*A [1/cm]*	t_{delay} *[ms]*	$P_{m,max}/P_{CJ}$	$P_{s,max}/P_{CJ}$
1	1.16	56.8	0.00393	0.269	0.312	0.258
			0.00309	0.259	0.344	0.292
2	1.40	46.0	0.00393	0.366	0.341	0.264
			0.00309	0.353	0.369	0.297

Discussion of Loss Mechanisms

The area divergence associated with the duct bifurcation presents the same type of loss mechanisms discussed with the other design concepts. If the incident shock is strong enough, a backward facing shock will form in the main branch [36,39,45]. As in the other cases, this shock serves as an entropy generating feature. As in the other designs, the area divergence will also compromise the ideality of the main contact surface and promote mixing between the detonation

products and the shocked air. More than the other concepts, this design will be adversely affected by the losses exacted during natural, partial fill expansion (Section 2.5).

Chapter 4: Computational Modeling, Diffuser Selection

4.1 Introduction

A series of single-cycle, non-reactive simulations were run using the commercial CFD software, ANSYS Fluent. These simulations assumed an ideal initial pressure, temperature, and velocity profile derived using the CJ state of a fuel-air mixture filled to $P_{fill} = 14$ [psia]. The same detonation driver was used in each case. Pressure, enthalpy, entropy and velocity data was gathered from each of these simulations and used to compute metrics quantifying the performance level of each configuration. In addition to assessing diffused configurations, fully filled (baseline) and half-filled configurations were also simulated to form a basis of comparison. Using the results from these simulations along, a diffuser regime (Diffraction-Reflection, Expansion Chamber, Bifurcating Duct) is selected, from that regime a specific design is selected for fabrication and experimental evaluation.

4.2 Computational Modeling, Evaluation

Description of Numerical Methods

ANSYS Fluent v14.0 was used to solve the unsteady, compressible, Navier-Stokes equations that describe the transient blowdown and shock propagation processes involved in the experiment. The gases were treated as an ideal gas mixture of calorically perfect constitutive species including N_2, O_2, CO_2, and H_2O. The molecular weights and specific heats of these species were taken directly from the default Fluent material properties library. The shock-propagation and blowdown processes were assumed to be approximately inviscid and no turbulence model was used. The chemistry of the flow was assumed to be frozen and no chemical reactions between the species were considered [18]. The momentum and energy equations were discretized using a bounded, second-order central scheme, the equations were integrated in time using a bounded, second-order implicit scheme, and the pressure and velocity equations were coupled using the block-coupled solver. The simulations' boundaries consisted only of adiabatic wall and pressure outlet type boundaries. The outlet boundaries were treated with Fluent's "Pressure Outlet" type of boundary condition which applies a fixed-value, Dirichlet-type boundary condition to the pressure field when the flow adjacent to the boundary is subsonic. When the flow is supersonic, the solver applies a zero-slope, Cauchy-type boundary to

the pressure equation. In both cases the momentum equations assume zero-slope normal to the boundary.

The physical geometry used for the computational domain was defined and meshed using ANSYS ICEM-Hexa structured grid generator. The completed meshes were then translated into Fluent-compatible unstructured mesh formats using ICEM's internal mesh conversion tool. For all simulations the meshes were made with near uniform grid spacing of $\Delta x = 0.002$ [m] in the direction of the propagating shock and $\Delta y = 0.001$ [m] in the perpendicular direction(s). The size of the time steps was held constant at $\Delta t = 1\ e - 6$ [s] such that waves propagating in the anticipated direction at up to $U = 2000$ [m/s] could still propagate properly without having to translate more than one cell width per time step.

Definition of Initial Conditions

The initial pressure, temperature, and velocity conditions are shown in Figure 4.1a. These profiles assume that a CJ detonation is instantly generated at the back wall of the combustor and has propagated at a constant rate up to the reactive-inert interface at $x = L_{int}$. In this case, it is assumed that the reactive portion is a stoichiometric acetylene-air mixture at an atmospheric fill pressure. The assumed fill conditions and associated CJ state are listed in Table 4.1. These profiles are non-uniform since the detonation is followed by a centered, Taylor expansion fan, as illustrated in Figure 4.1b. This expansion fan serves to isentropically expand and decelerate the detonation products such that the back wall zero velocity condition can be met. The exact distribution of flow parameters was derived using the Riemann Invariant relations described in Equations 2.14 2.17. The molecular composition of the detonation products was determined using the major product assumption i.e. all products constitute CO_2, H_2O and N_2. All conditions within a diffuser or straight extension are that of quiescent, atmospheric air at room temperature.

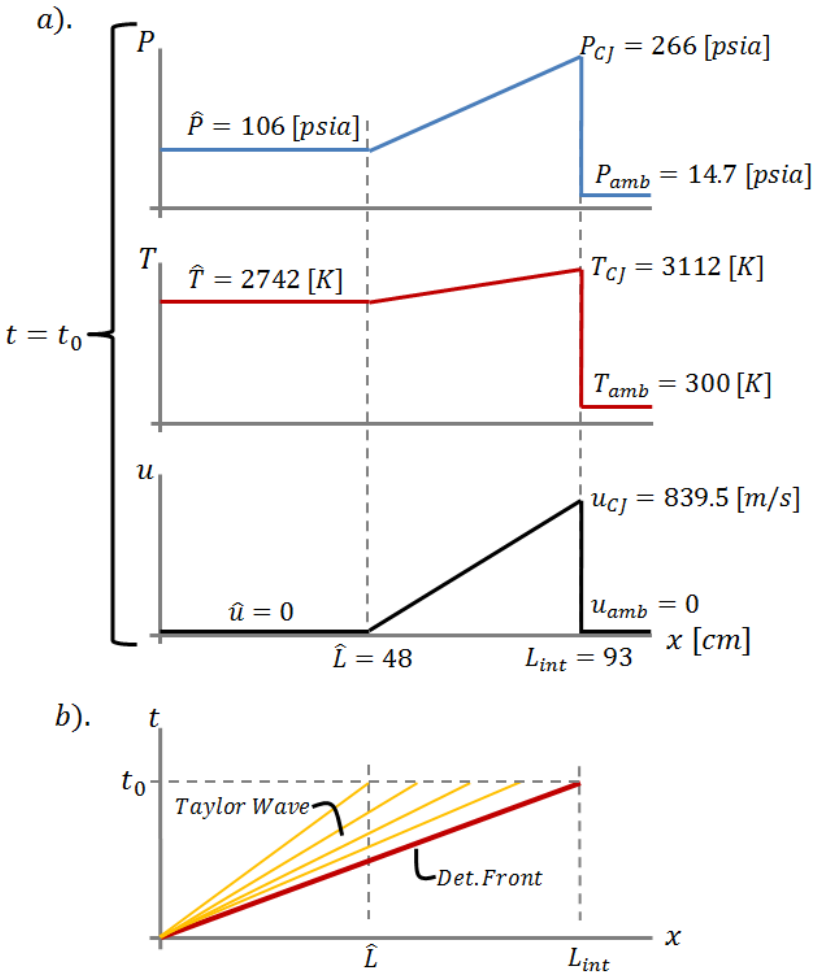

Figure 4.1. a). Initial pressure, temperature, and velocity profiles for the simulations. b). Wave diagram of the detonation and accompanying Taylor expansion wave which causes the spatially uniform profiles.

Table 4.1. Assumed fill conditions for and associated CJ detonation state. An acetylene-air mixture was assumed to improve analogy with a practical, multi-shot device.

Mixture	P_{fill} [psia]	14.7
	Oxidant	Air
	ϕ	1
CJ Conds.	P_{CJ} [psia]	279
	U_{CJ} [m/s]	1866
	a_{CJ} [m/s]	1026

Definition of Baseline

To serve as a point of comparison between diffusers, a baseline PDC configuration was defined and characterized. All diffused configurations added an inert extension to this baseline, undiffused configuration. For this study, this baseline was assumed to be a "fully" filled tube with a convergent neck, as illustrated in Figure 4.2. Note that a small section of air exists between the detonation front and the exit, hence making it slightly less than fully filled. A convergent neck is added to all designs to improve the analogy between single shot simulations and experiments. In many practical, multi-shot PDC configuration, a convergent neck is used to generate back pressure during filling and helps prevent loss via over-filling [47]. An area contraction of $\alpha = 1.55$ was used in these simulations and subsequent experiment, corresponding to an area transition from NPS 4" Sch 80 pipe to NPS 3" Sch 40 pipe.

Figure 4.2. Illustration of baseline configuration shown with initial temperature contour. Note that it is nearly full with a convergent neck at the outlet.

Computational Model Performance Metrics

The diffused simulations will be compared to the baseline case using four performance characteristics:

1) *Peak Pressure Attenuation* – A diffuser should weaken the strength of the leading shock as to prevent damage from a turbine section. The peak pressure, P_{max}, at the outlet of the diffuser will be normalized by the Chapman-Jouguet pressure, P_{CJ}. Hence, the metric will defined as

$$\Pi \equiv \frac{P_{max}}{P_{CJ}}.$$

Figure 4.3 is a sample outlet pressure history from an Expansion Chamber simulation. The pressures shown are the area weighted averages across the outlet span. For the Bifurcating Ducts, the peak pressure used to compute the parameter was overall peak pressure of the two outlets.

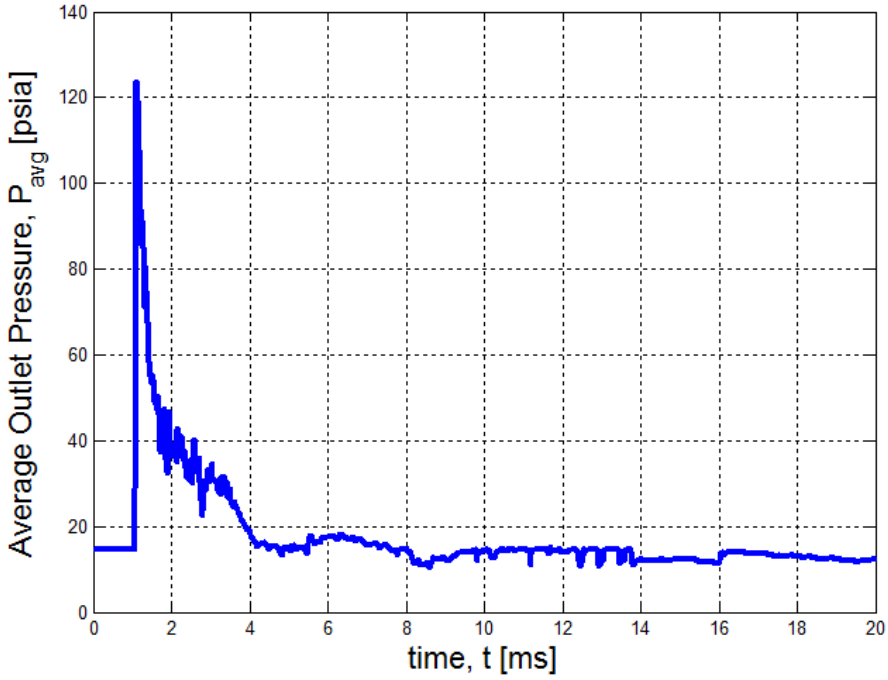

Figure 4.3. Sample pressure history from Expansion Chamber simulation. Note the large pressure peak at start of the pulse event.

2) *Steadiness* – The steadiness of a diffuser will be judged using the exergy flux per unit length at the outlet, $\dot{A}_f{}' = a_f * \dot{m}'$ for a two-dimensional simulation. Steadiness will be quantified by the coefficient of variation, CoV, of the exergy flux,

$$CoV(\dot{A}_f{}') \equiv \left[\frac{\sigma(\dot{A}_f{}')}{\mu(\dot{A}_f{}')}\right]_{t1\to t2},$$

where σ indicates the standard of deviation of the exergy flux, $\dot{A}_f{}'$, and μ indicates the mean. The CoV will be computed on a particular time, $t_1 < t < t_2$, interval which contains the pulse event. The time t_1 corresponds to the time when the pulse arrives at the exit and the time t_2 corresponds to the time when 75% of the total, cumulative advected exergy exits the configuration. This upper threshold is considered to be the end of the pulse event. This point is illustrated in Figure 4.4. The lower time bound was chosen so that initial delay would not skew the CoV by decreasing the mean and increasing the standard of deviation. Similarly, the upper time bound was chosen since all configurations demonstrated a slow, exponential blowdown. Inclusion of this feature would skew results in a way similar to the initial delay.

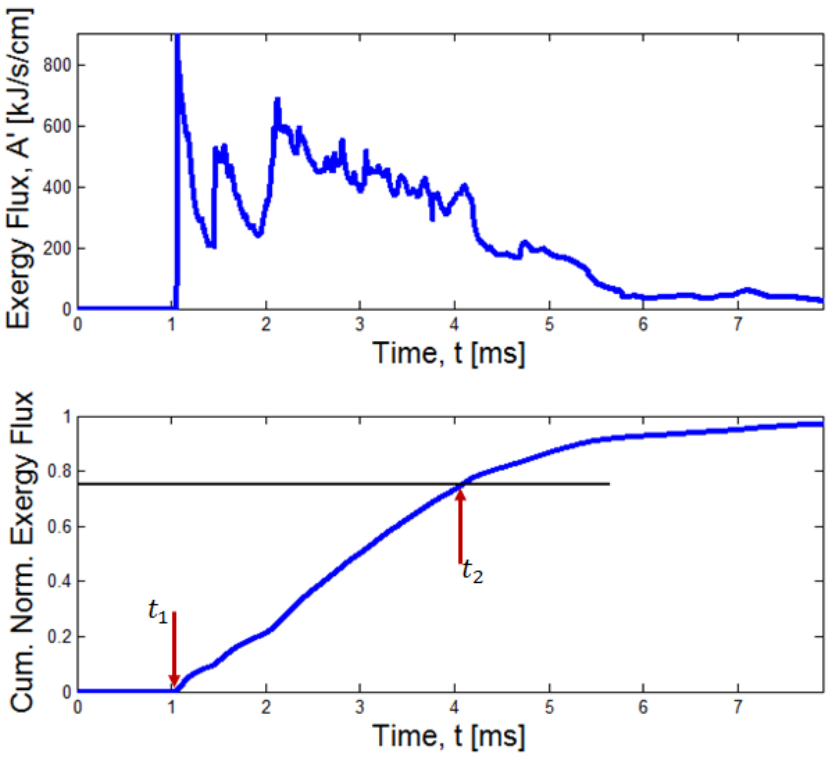

Figure 4.4. Exergy flux versus time and cumulative, normalized exergy flux versus time. t_1 is the start of the pulse and t_2 is the end of the pulse, corresponding the 75% accumulation of total advected exergy.

An ideal diffuser will have a coefficient of variation $CoV(\dot{A}_f{}') \rightarrow 0$ over the interval of interest. Note that metric aims to measure the steadiness during the active duration of the exhaust flow, *not the steadiness over the entire pulse detonation cycle*.

3) *Pulse Duration* – As stated in the project scope, one of the aims of the diffuser was to take the energy contained in the pulse detonation exhaust and extend its duration. To quantify this, a pulse duration ratio is defined as

$$\tau \equiv \frac{\Delta t_{pulse,diffused}}{\Delta t_{pulse,undiffused}} = \frac{(t_2 - t_1)_{diffused}}{(t_2 - t_1)_{undiffused}},$$

where t_1 and t_2 correspond to the start and end of the pulse as illustrated in Figure 4.4.

4) *Availability Preservation* – As discussed in Section 2.5, an inert extension necessarily destroys the availability of detonation products by way of entropy generation. Availability preservation will be measured by the ratio of diffused, advected exergy over the baseline, advected exergy,

$$\epsilon \equiv \frac{A'_{f,total}\big|_{diffused}}{A'_{f,total}\big|_{undiffused}}$$

where $A'_{f,total} = \int_0^{t_{BD}} a_f(t) * \dot{m}(t)\, dt$ across the outlet(s) up until the end of blowdown. A diffuser will seek to have to have an effectiveness $\epsilon \to 1$.

Simulation Results – Time Sequence Images

Expansion Chamber Diffuser

A time sequence of still images taken from the last design iteration of the Expansion Chamber simulations is shown in Figure 4.5. These images feature Schlieren type contours which depict density gradients in the flow, where red is a large gradient and blue is zero gradient. These gradients are most useful for flow visualization and clearly depict shock reflection events. From the figure, frames b). and c). show the leading shock as the rightmost disturbance and the contact surface trailing behind it. A reflected shock is also seen propagating toward the back wall. This shock is a result of the converging nozzle/neck feature common in all configurations. Frames d). and e). show the leading shock traveling through the expansion chamber and propagating toward the exit. Also during this time, the main reflected shock is seen forming at the expansion chamber's area contraction. Although difficult to discern, the re-reflected shock can be discerned in the last two frames, exiting the configuration.

Diffraction-Reflection Diffuser

Figure 4.6 is a time sequence of Schlieren contours for a design 6 of Diffraction-Reflection regime. As in Figure 4.5, note the separation of the leading shock and the contact surface behind it. Frames d). and e). depict the reflection events from the top and bottom surfaces of the diffuser, qualitatively confirming the intended diffuser mechanism. The last two frames show the contact surface and detonation products propagating toward the exit. Various stationary shocks can be seen forming during the quasi-steady blowdown process. These shocks form to direct the supersonic sonic flow characteristic of a PDC.

Bifurcating Duct Diffuser

Figure 4.7 is a time sequence of temperature contours for design 2 of the Bifurcating Duct concept. Here, a temperature contour was used to better illustrate the behavior of the

contact surface separating the shocked air (blue) from the detonation products (orange). Frames a). through c). depict the leading shock propagating and then diffracting as it meets the area change associated with the duct bifurcation. An interesting flow feature develops in frame d). where an attached bow shock forms at the sharp corner of the duct bifurcation. This shock forms since the leading shock was strong, inducing supersonic post-shock flow. While the shock splits fairly cleanly, the contact surface does not. Significant, turbulent mixing can be seen in the secondary branch of the configuration. Along with losses incurred by the bow shock or reflected shocks, mixing processes also exact a large penalties with respect to entropy generation.

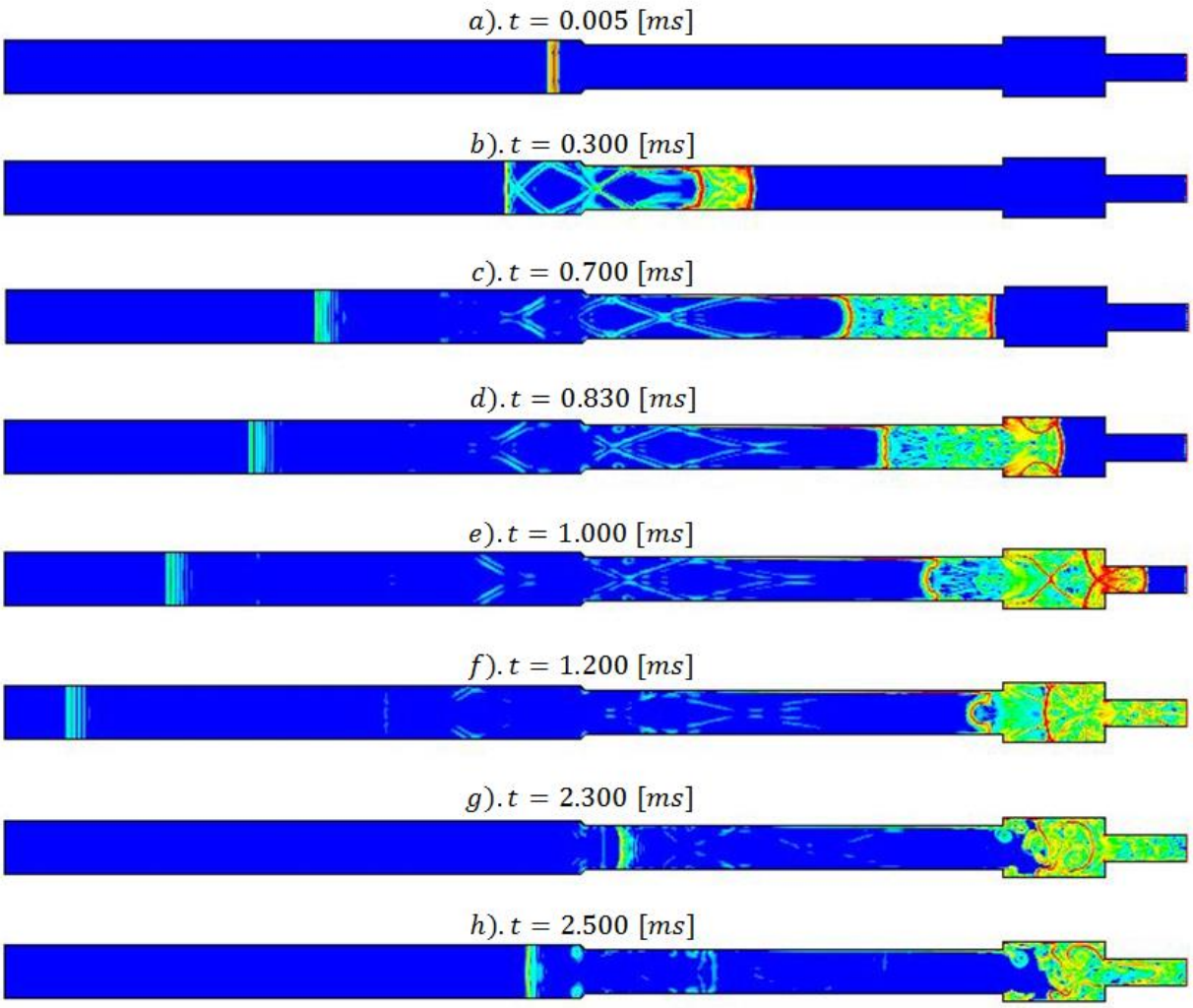

Figure 4.5. Schlieren contour sequence of design 4 of the Expansion Chamber concept. Contours indicate gradients in density, red corresponding to a large gradient and blue corresponding to zero gradient.

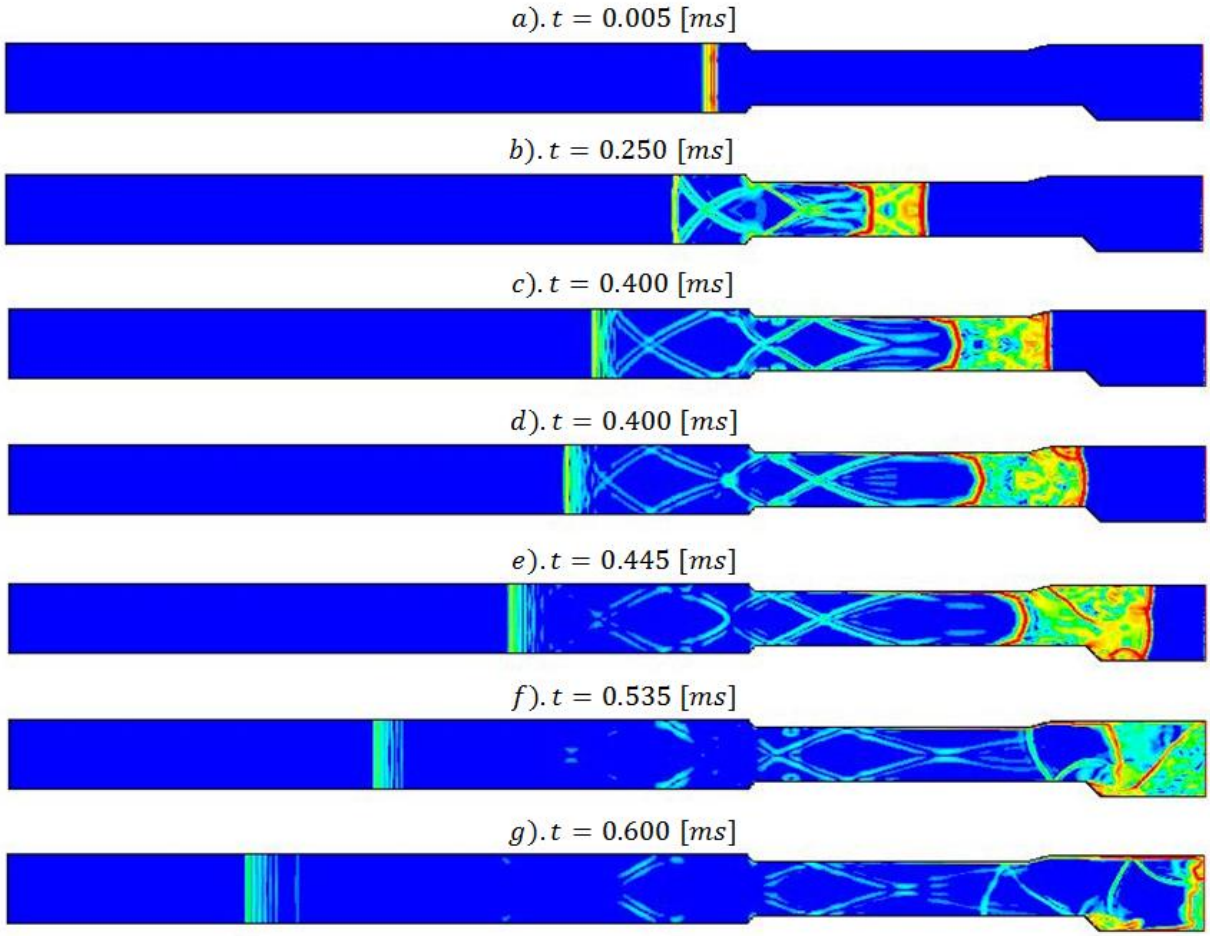

Figure 4.6. Schlieren contour sequence of design 6 of the Diffraction-Reflection concept. Note the circular disturbances reflecting from the top and bottom surfaces of the diffuser.

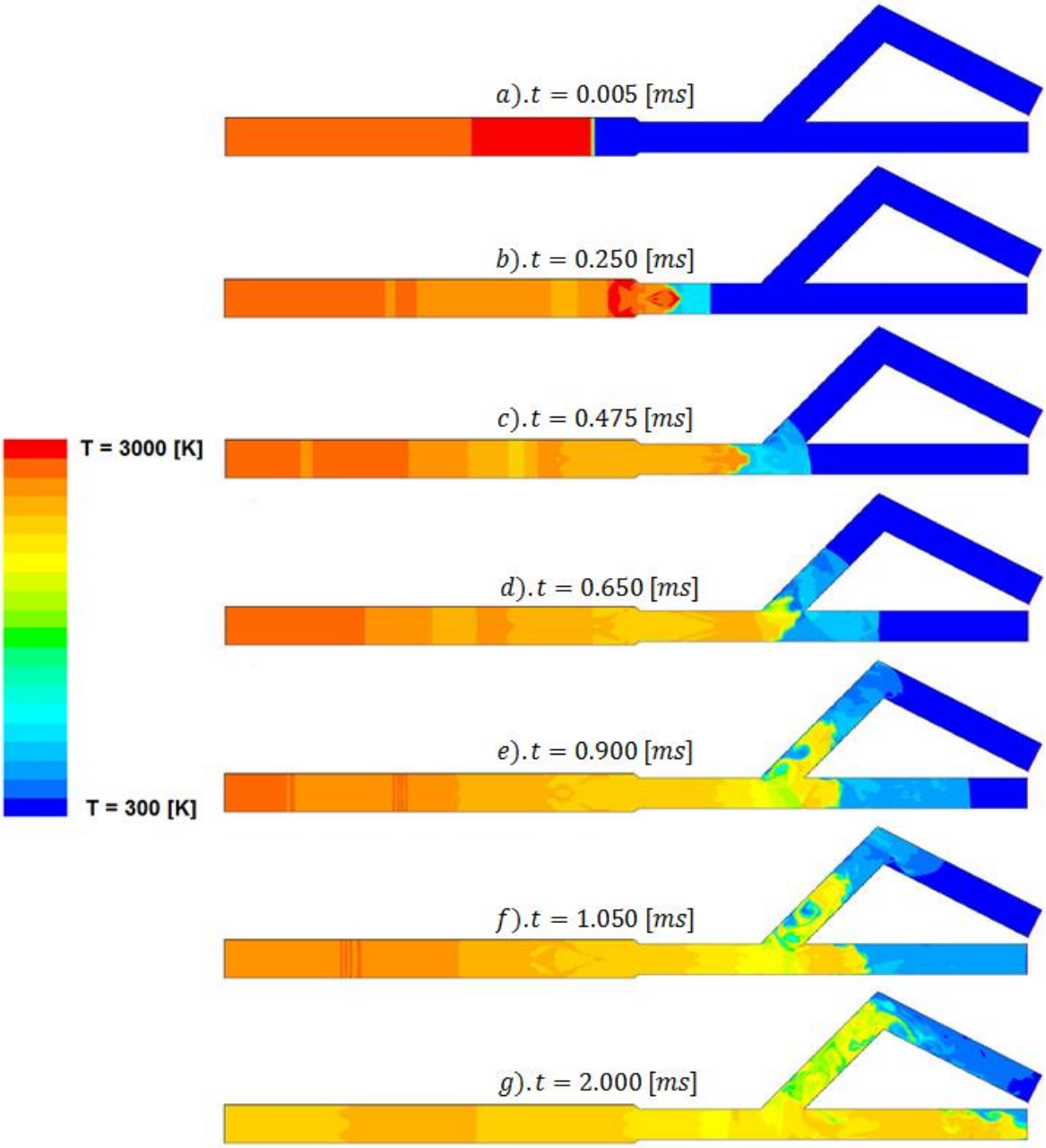

Figure 4.7. Temperature contour sequence of design two of the Bifurcating Duct concept. Note the bow shock in frame d). and the general mixing in the secondary branch.

Simulation Results – Comparison to Analytical Performance Metrics

Expansion Chamber Diffuser

For the expansion chamber designs, the only performance parameter which could be estimated was the peak pressure attenuation, Π. The results of the simulations are compared against the analytical attenuation prediction in Table 4.2. Recall that designs 1 thru 3 investigated the effects of the run up length, L_{run}, and design 4 investigated the effect of the area ratios, α_1 and α_2. Design 4 used the same the same run up length as in design 3, but used a more gentle area divergence ratio ($\alpha_1 = 0.284$ for designs 1 thru 3, compared to $\alpha_1 = 0.519$ for design 4). Overall, the attenuations predicted analytically were quite close to those determined computationally. This accuracy can be attributed in part to the values used for incident wave strength, M_i, determined from experiment.

Table 4.2. Comparison of analytical and computational pressure attenuation ratios for the expansion chamber designs. In all, the analytical estimates were quite close. Note that this accuracy is due in part to the accurate estimates for incident shock wave strength, M_i.

				$\Pi = P_{max}/P_{CJ}$		
Iteration	L_{run} *[cm]*	α_1	α_2	*Anal.*	*Comp.*	***% Diff.***
1	39.4	0.284	5.44	0.477	0.452	***5.4***
2	106.7	0.284	5.44	0.344	0.383	***10.7***
3	76.2	0.284	5.44	0.380	0.402	***5.6***
4	*76.2*	0.519	4.83	0.493	0.453	***8.5***

Diffraction-Reflection Diffuser

The analytical model for the diffraction-reflection diffuser included a timing parameter, t_{delay}, and an overall pressure attenuation, Π. Of the six designs chosen, only designs 4 and 6 were computationally evaluated. The simulation results for these two designs suggested that shock reflection is an ineffective pressure diffusion mechanism. To this end, the most influential feature of the diffuser was the overall area change, with the intermediate ramp geometries playing no role. This point is elaborated on further in the discussion section. Despite this fact, Table 4.3 compares t_{delay} and Π as determined both analytically and experimentally. Note that the computational values for t_{delay} determined by examining still images taken from the simulation. As such, the resolution to this parameter is limited. Regardless, it is clear that

analytical delay times overestimate those seen experimentally. This fact can be attributed to the lack of spatial resolution in the region of the diverging ramps. As before, the pressure attenuation values estimated during analysis proved to be quite close to the simulated attenuation.

Table 4.3. Comparison of analytical and computational performance parameters for diffraction-reflection diffusers. For both designs, analytical attenuation estimates were quite close. However, computational delay times were lower than predicted owing to lack of grid resolution in the diverging regions.

		t_{delay} *[ms]*		$\Pi = P_{max}/P_{CJ}$		
Design	*Regime*	*Anal.*	*Comp.*	*Anal.*	*Comp.*	***% Diff.***
4	Stag. ($\Delta x \neq 0$)	0.062	~0.060	0.486	0.491	***1.0***
6	Stag. ($\Delta x \neq 0$)	0.089	~0.070	0.481	0.469	***2.5***

Bifurcating Ducts Diffuser

The analytical models for the bifurcating duct designs provided more comparison metrics than the offer models developed. Three timing parameters (τ_m, τ_s, $\Delta\tau$) and two pressure attenuation parameters (Π_m, Π_s) are compared between the computational and analytical models. Table 4.4 and Table 4.5 summarize the results for these parameters. With regard to timing (Table 4.4), the analytical models did a strong job of predicting overall transit times and pulse delay times. The least accurate feature of the analytical models proved to be prediction for pulse delay, $\Delta\tau$, and estimation of secondary duct pressure attenuation, Π_s. The analytical efforts do not account for the diffraction/reflection processes which occur at the elbow of the secondary duct. Especially in the case of Design 2, where the elbow is closer to the tube exit, these transient diffraction/reflection processes have a much stronger effect on the outlet profiles.

Table 4.4. Comparison of analytical and computational timing parameters for the bifurcating duct diffusers. The analytical model overestimates pulse delay times since it does not account for diffraction/reflection processes in the secondary duct's elbow.

		τ_m *[ms]*			τ_s *[ms]*			$\Delta\tau$ *[ms]*		
Design	*LR*	*Anal.*	*Comp.*	***% D.***	*Anal.*	*Comp.*	***% D.***	*Anal.*	*Comp.*	***% D.***
1	1.11	0.634	0.624	***1.6***	0.893	0.866	***3.1***	0.259	0.270	***4.2***
2	1.32	0.504	0.492	***2.4***	0.857	0.862	***0.6***	0.353	0.394	***11.0***

Table 4.5. Comparison of analytical and computational pressure attenuation parameters for the bifurcating ducts diffusers. Once more, the analytical model over predicts the pressure attenuation in the secondary duct by virtue of neglecting diffraction/reflection processes at the duct elbow.

		$\Pi_m = P_{m,max}/P_{CJ}$			$\Pi_s = P_{s,max}/P_{CJ}$		
Design	*LR*	*Anal.*	*Comp.*	***% Diff.***	*Anal.*	*Comp.*	***% Diff.***
1	1.11	0.344	0.348	***1.2***	0.292	0.266	***9.3***
2	1.32	0.369	0.381	***3.2***	0.297	0.225	***27.6***

Simulation Results – Comparison to Baseline

Diffusers were judged against the baseline with the use of Pareto-type comparison plots. Using the four performance metrics previously outlined (peak pressure attenuation, steadiness, blowdown duration, availability preservation), these plots illustrate the strengths and weaknesses of each design compared to one another and compared to the baseline performance. Data points were grouped by design since designs of the same regime performed comparably. Also included in the comparison plots are the results from a partial fill case with the fill fraction $ff = 0.5$. The black dotted lines indicate the maximum or minimum boundary for a given parameter. Here:

- $\Pi_{min} = 0$ and $\Pi_{max} = 1$
- $\epsilon_{min} = 0$ and $\epsilon_{max} = 1$
- $\tau_{min} = 1$
- $CoV_{min} = 0$

The use of four parameters implies a maximum of six combinations of parameters, making a maximum of six plots. Four of the six combinations are presented here.

In the first metric comparison, Figure 4.8 plots effectiveness (availability preservation) against the coefficient of variance of the exergy flux (steadiness). As mentioned before, data points are grouped by design. This plot shows that the Diffraction-Reflection diffusers offer the best effectiveness of all designs/concepts. Conversely, the Expansion Chamber design exacts the largest penalty with respect to entropy generation and availability preservation. With regard to steadiness, the Bifurcating Duct design is the strongest concept. This plot illustrates the fact that the Expansion Chamber design is non-optimal since the Diffraction-Reflection concept achieves similar steadiness but preserves more pulse availability.

Figure 4.9 plots effectiveness as a function of pulse duration ratio. A general trend is immediately clear: a shorter pulse ($\tau \to 1$) leads to improved preservation of availability in the exhaust stream. This result is logical since a longer residence time (larger τ) allows for more irreversible processes to take hold. The graph illustrates that Diffraction-Reflection and Bifurcating Duct concepts offer only offer modest improvements with regard to pulse duration. In fact, this result suggests that the pulse elongation mechanisms with the Diffraction-Diffuser regime were completely ineffective and ill-conceived. The Expansion Chamber concept obviously provide the best pulse elongation by far. As mentioned, this elongating effect comes at the expense of entropy generation and availability destruction.

Figure 4.10 shows maximum pressure attenuation versus pulse duration ratio for all configurations. At first glance, all diffusers offer similar peak pressure attenuation compared to the baseline performance, with $\Pi_{median} \approx 0.45$. When comparing diffusers with one another, the Bifurcating Ducts concept offers the best peak pressure attenuation, with the Expansion Chamber concept performing comparably. However, this graph illustrates that the Diffraction-Reflection concept is non-optimal with respect to the parameters of interest. It provides the shortest pulse length and the worst attenuation of all regimes.

Figure 4.11 compares the peak pressure attenuation ratio versus the steadiness for each configuration. This plot also illustrates a clear trend and important result. Note the possibly linear relationship between the pressure attenuation and the steadiness parameter. This result implies that the steadiness is dictated by the strength of the of the leading shock, and the large exergy flux which it creates.

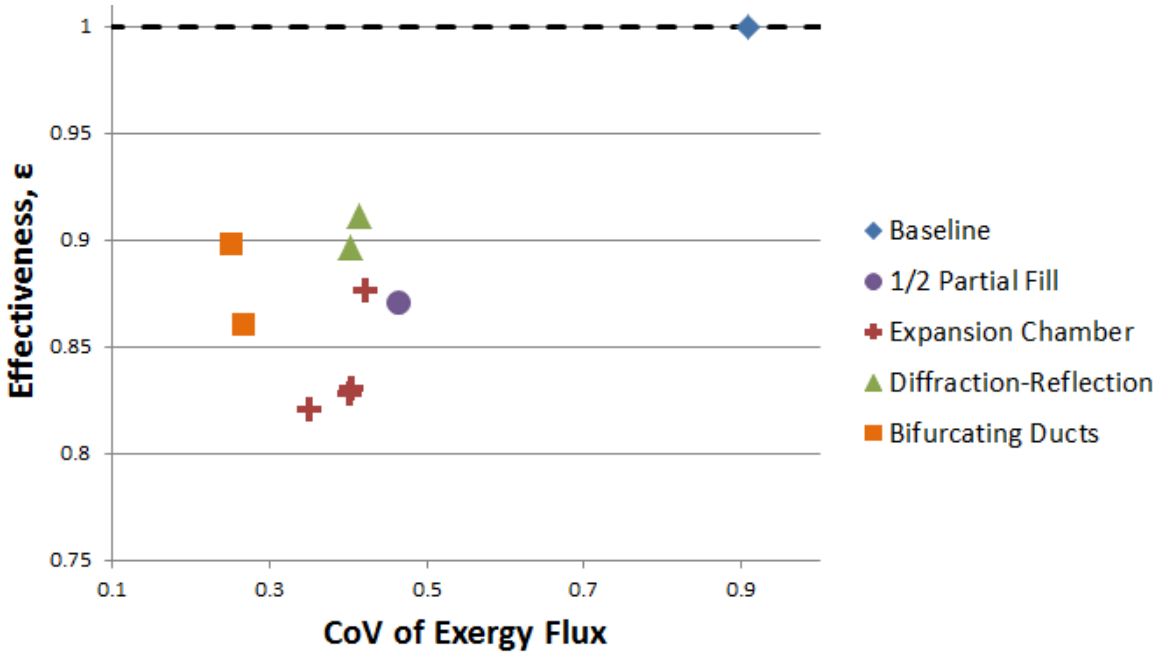

Figure 4.8. Comparison plot of effectiveness, ϵ, versus CoV of exergy flux. This plot demonstrates that the Bifurcating Duct concept is the most steady, and that the Expansion Chamber concept is non-optimal.

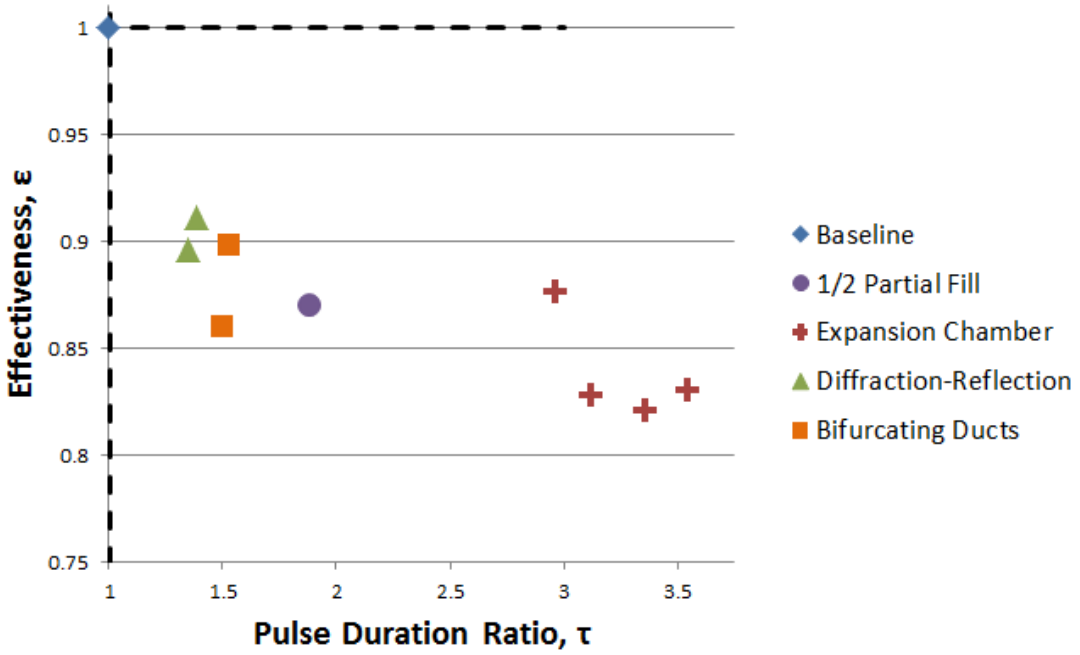

Figure 4.9. Comparison plot of effectiveness, ϵ, versus blowdown duration ratio, τ. This graph suggests an inverse relationship between blowdown duration and availability preservation.

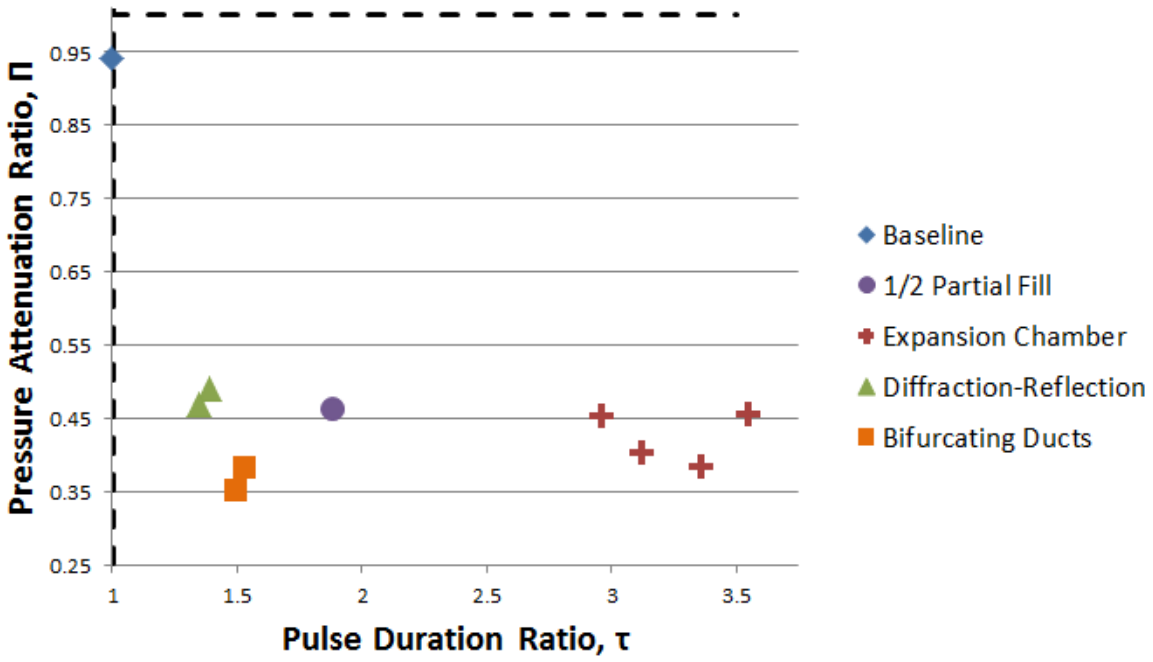

Figure 4.10. Comparison plot of peak pressure attenuation ratio, Π, versus blowdown duration ratio, τ. The Bifurcating Ducts concept offers the best attenuation, while the Expansion Chamber concept once again is non-optimal.

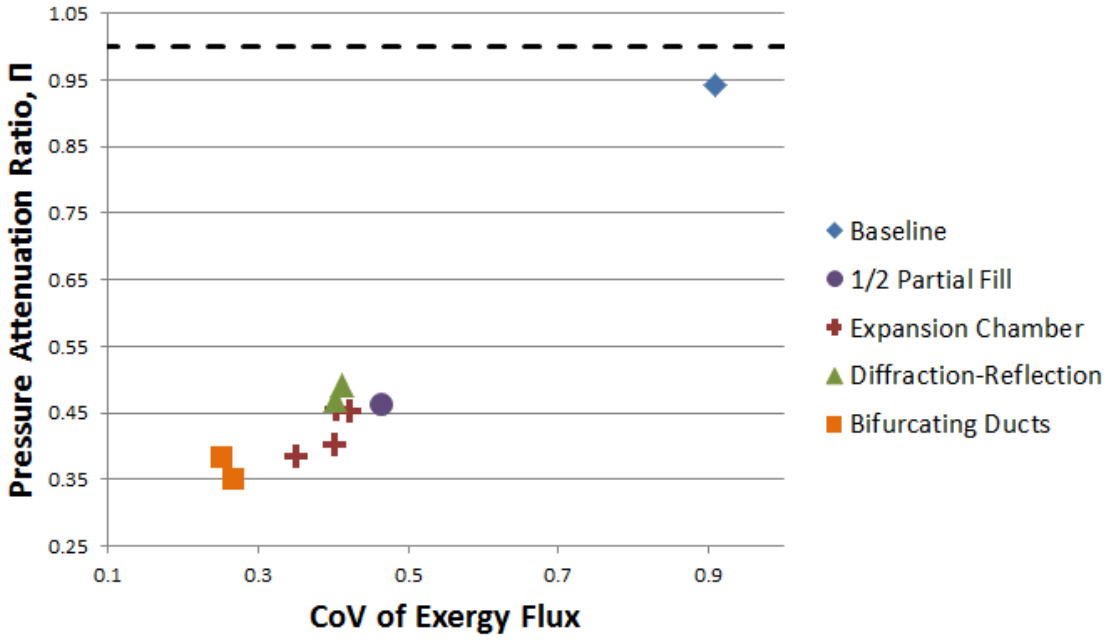

Figure 4.11. Comparison plot of peak pressure attenuation, Π, versus CoV of exergy flux. Note the suggestion of a linear relationship between the strength of the leading shock and the steadiness

Discussion

Expansion Chamber Diffuser

Despite uncertainty during the detailed design phase, the reflection processes proved to be an effective pulse diffusion mechanism. Figure 4.12 depict the exergy flux histories for the baseline, Diffraction-Reflection, Bifurcating Ducts, and Expansion Chamber configurations. For the Expansion Chamber exergy trace (green), this plot shows clear reflected events exiting the tube after the main peak. As such, the addition of an expansion chamber significantly increased the pulse duration by ~ 200% and also provided excellent peak pressure attenuation. However, as expected, the reflection and expansion processes of this concept exacted a significant penalty via entropy generation, advecting ~10% less exergy compared to the Diffraction-Reflection regime and ~15% less than the baseline.

The success design raises questions regarding the benefit of elongating the detonation pulse. While distributing the energy of a detonation over time may be helpful with regard to work extraction and turbine reliability, pulse elongation necessarily increases the pulse detonation cycle (Figure 1.1), thus decreasing the maximum operating frequency of a tube. However, the detonation and blowdown processes represent a small fraction of the total pulse detonation cycle time, with the majority being dominated by the filling and purging processes. Thus, increases in pulse duration may be considered acceptable to system designers if such an increase presents more extractable energy at the cost of a small decrease in operating frequency. Using numbers, a tube operating at $f_{op} = 20$ [Hz] corresponds to a cycle time $t_{cycle} = 50$ [ms]. Assume, the addition of a diffuser increases the cycle by 8 [ms], as suggested by the current results. This increase in cycle time would decrease the maximum operating frequency by 15%.

Diffraction-Reflection Diffuser

Unfortunately, the Diffraction-Reflection design concept proved to be an ineffective pulse diffusion solution. While the overall area divergence was relatively effective in attenuating the lead shock, decreasing the peak pressure by more than half. That said, the timed reflection events had no effect on the exhaust flow. Although their propagation can be reasonably predicted, the reflected disturbances only affect flow near the site where it attaches to the leading shock [48]. Figure 4.12 shows how the exergy flux history of this diffuser regime (black) closely

mirrored the history of the baseline case, providing strong initial attenuation and pulse elongation of only 30%.

Bifurcating Duct Diffuser

The Bifurcating Duct concept functioned as anticipated and proved to be an effective design. Adding to its success in the simulated domain, it offered the most descriptive analytical design tools which could be used in a design setting. The flowpath bifurcation generates minimal entropy, advecting only ~12% less exergy than the baseline. The bifurcation combined with the natural expansion process also provides an effective pressure attenuation mechanism, decreasing the lead pressure spike by ~60% and outperforming all other configurations in this regard. Also, this design was the most stead of all designs due to its strong lead shock attenuation and pulse staggering technique. However, the bifurcating duct concept only modestly increased the pulse duration by ~50%.

4.3 Diffuser Selection

Concept Selection

We shall begin by selecting a diffuser concept to experimentally investigate since each diffuser concept demonstrates similar performance and characteristics. Previously introduced, Figure 4.12 plots the exergy flux histories of all configurations and provides an excellent tool for qualitative comparison. Of the three general design concepts, the intended pulse diffusion mechanisms in the Bifurcating Duct and Expansion Chamber were the most successful. However, in the case of the Diffraction-Reflection concept, the intended pulse diffusion mechanism turned out to be physically ill-founded, making the concept little more than a diverging area. As such, the Diffraction-Reflection concept is deemed unsuccessful and will not be considered further.

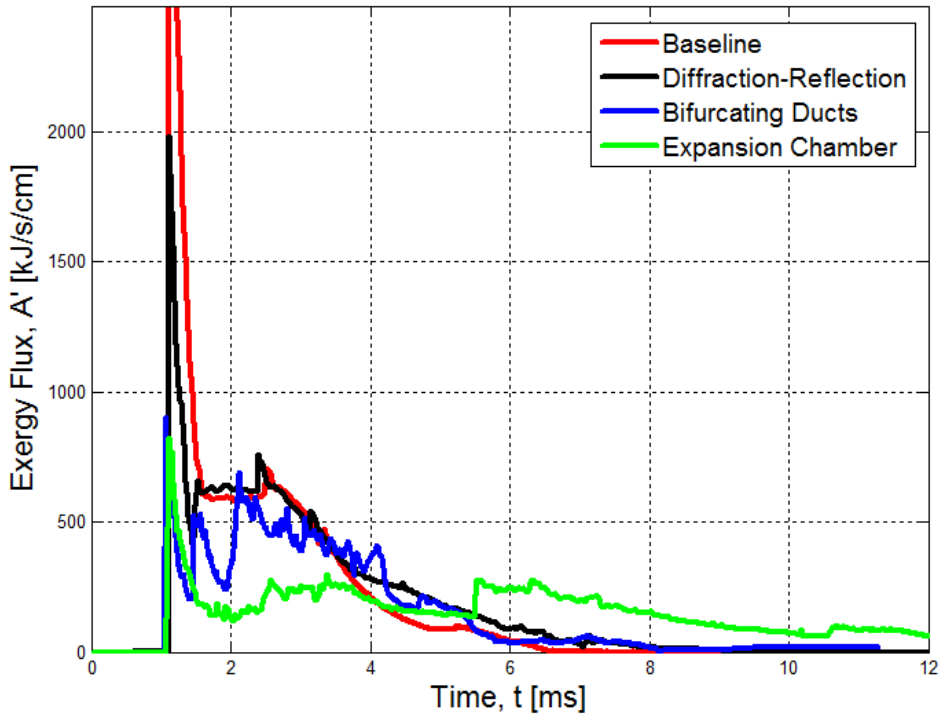

Figure 4.12. Comparison of exergy flux histories for baseline, Diffraction-Reflection, Bifurcating Duct, and Expansion Chamber configurations.

Let us revisit the four diffuser functions initially outlined earlier:

1) *"Attenuate the peak pressure of the leading shock"* – All designs of both concepts proved to effectively complete this function.
2) *"Improve steadiness during the pulse event."* – Using the defined metric, the bifurcating duct concept provides the steadier flow. However, this steadiness is the result of the superposition of two pulses weaker than the baseline pulse.
3) "*Elongate the pulse event."* – The Expansion Chamber concept clearly provides an advantage here, as shown quantitatively by the metric and qualitatively by the exergy flux history in Figure 4.12.
4) *"Maintain the high availability of the blowdown process."* – The simulation results indicate that the Bifurcating Duct concept generates less entropy than the Expansion Chamber. This result agrees with what one would expect, since an expansion chamber necessitates several shock reflection processes which necessarily generate entropy.

Other aspects to consider include:

- *Manufacturability* – Both remaining concepts are extremely simple with respect to geometry. Additionally, simulated models have already taken into account standard sizing of pipes and laterals.
- *Analytical Modeling* – The analytical model for the Bifurcating Duct concept was the most descriptive of all concepts, although it could be improved upon. This type of simple model could be useful for a designer in the future with respect to computing timing and pressure attenuation of pulses in a full PDC array. Comparatively, the reflection processes of an expansion chamber and the inaccuracy of a quasi-one-dimensional model make simple, analytical development more difficult.

All things considered, the Bifurcating Duct concept will be experimentally investigated due to its simplicity, ease of manufacture, and strong simulated performance. This concept is considered to be more viable since it generates fewer losses and provides the strongest wave attenuation. Also, such a concept lends itself well to a design process if to be integrated into a full, multi-shot PDC-turbine array.

Design Selection

Within in the bifurcating ducts regime, two designs were generated and simulated. The geometric parameters of simulated performance of each are summarized in Table 4.6. and qualitative illustrations of each design are shown in Figure 4.13. Recall that these designs varied primarily by the ratio of the different path lengths while keeping the secondary path length constant. Design 1 featured a shorter stagger in pulse departure but featured greater lead shock attenuation in the main duct. Conversely, Design 2 featured a longer stagger but less shock attenuation. However, the largest difference between the two is with respect to entropy generation/availability preservation. Since design 2 features a shorter main duct length, less availability is destroyed during blowdown. Although availability cannot be experimentally measured (to be discussed further in the next chapter), design 2 has been selected for experimental investigation since it theoretically provides this advantage in performance.

Table 4.6. Summary of simulated Bifurcating Duct designs. Designs varied only by ratio of path lengths while secondary path lengths are held constant. Design one offers an edge in shock attenuation, but design two offers a greater pulse width and better availability preservation.

Design	$L_{s,tot}/L_{m,tot}$	$L_{m,tot}$ *[cm]*	Π	τ	CoV	ϵ
1	1.16	56.8	0.35	1.50	0.267	0.859
2	**1.40**	**46.0**	**0.38**	**1.54**	**0.254**	**0.897**

***Bold** row indicates selected design.

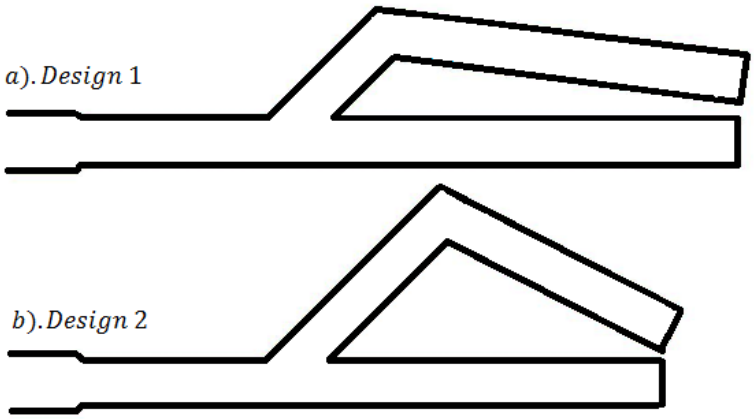

Figure 4.13. Scale illustrations comparing the geometric differences between Bifurcating Duct a) Design 1, $L_{s,tot}/L_{m,tot}$ = 1.11 and b) Design 2, $L_{s,tot}/L_{m,tot}$ = 1.32.

Chapter 5: Experimental Methods

The final chapter of this report discusses the experimental techniques employed with this work. The overall goal of the experiments is to devise a lab-scale, pulse detonation apparatus which can be used to test physical diffuser prototypes.

To this end, the experimental efforts unfolded in three major phases and each will be discussed in detail:

Phase 1 – Initial Baseline Design and Characterization

Phase 2 – Baseline Modification and Characterization

Phase 3 – Diffuser Design for Manufacture and Experimental Evaluation

5.1 Phase 1 – Design of Initial Baseline

Detonation Tube as PDC Analogue

A single shot detonation tube was chosen as the lab-scale analogue to a fully functioning, multi-shot PDC. The physical principles of a detonation tube are identical to that of a PDC: a combustion volume is filled with a detonable mixture and ignited from the closed end, generating a detonation wave which propagates out of the open end. The most obvious difference is that a detonation tube is filled only once per experiment in a very controlled manner. It does not require high-speed valving, control, and repeated ignition like many multi-shot apparatus. To this end, a single shot tube is advantageous with regard to cost and time efficiency.

Of course, the disadvantage of using a single shot experiment is the loss of fidelity in replicating the physics of interest. Table 5.1 summarizes the boundary and initial conditions for both single shot detonation tube and a multi-shot PDC-turbine array. One of the most important differences between configurations arise with the initial conditions, specifically with the treatment of the reactive-inert interface. In the present analyses, simulations, and experiments, the reactive-inert interface is characterized by a sharp gradient between the reacting mixture and air. However, the filling process of a multi-shot device will result in a gradient separating the reactive and inert regions within the tube [49].

With this fact, the question becomes how the omission of a gradated interface influences the wave dynamics of this problem. Sanders compared experimental pressure, temperature and water concentration histories against those predicted by a simple, single shot, method of characteristics (MoC) model. This MoC model is essentially synonymous to the quasi one-dimensional CFD simulations presented previously. His results indicated strong agreement between pressure and water concentration histories. For temperature, however, the MoC results slightly overestimated the measured temperature, probably owing to the fact that the model does not account for heat transfer [49,50]. That said, given this overall agreement, one may assume that the same wave dynamics govern both the idealized, single shot model and the realistic, multi-shot apparatus.

Table 5.1. Summary of boundary and initial conditions for single and multi-shot apparatuses.

	Single Shot Detonation Tube	*Multi-shot PDC-Turbine Array*
Boundary Conditions	▪ Closed back wall, unrestricted opening ▪ Room temperature walls	▪ Closed back wall, opening interfaced with turbine array ▪ Walls in thermal equilibrium
Initial Conditions	▪ Quiescent detonable mixture ▪ Diaphragm generates clearly defined reactive-inert interface	▪ Non-quiescent detonable mixture ▪ Reactive-inert interface not clearly defined ▪ Potential backflow from reflections, pressure disturbances

In general, the author acknowledges the differences between single shot and multi-shot apparatuses, but does not believe that the limitations of the single-shot methodology will compromise results. The wave dynamics will remain comparable in both cases, and any differences will not significantly affect the diffusion mechanisms at work. Other effects, such as model overestimation of temperature or open end boundary effects on blowdown, will systematically affect all cases in this study. While their presence certainly would influence results, they will not be accounted for owing to the assumed scope of the project. As stated previously in the project scope, the emphasis for this project was placed on wave dynamic

manipulation of a decaying detonation, with no consideration for heat transfer or combustor-turbine interface.

Detonation Tube Facility

A schematic of the detonation tube installation at the Combustion Systems Dynamics Laboratory is shown in Figure 5.1. The facility is organized such that the detonation tube and data acquisition hardware are kept in one room while the experiment is monitored and controlled from a separate room. Vacuum, vacuum relief, oxidant, and fuel are the four main lines which interface with the tube. Each connects with the tube at a shut-off valve and connect to the control area via flexible tubing. Note that the oxidant line carries both O_2 and air flows into the tube. Static and dynamic pressure signals interface with the data acquisition hardware (power supplies, signal conditioners, DAQ). The sampled data is transferred to the control computer by way of USB bus.

In the control area, evacuation and filling processes are monitored using a LABVIEW on the control computer. Oxidant and acetylene addition is manually modulated using needle valves. Oxygen, acetylene and air supplies are all equipped with pressure regulators, while the acetylene supply is also situated with a check valve and flame arrestor for precautionary purposes. The ignition signal is also manually activated once the filling procedure is complete. This signal both ignites the test section and triggers the DAQ for high-speed data acquisition to capture the detonation event and blowdown. The detonation products exhaust to the ambient conditions of the test area.

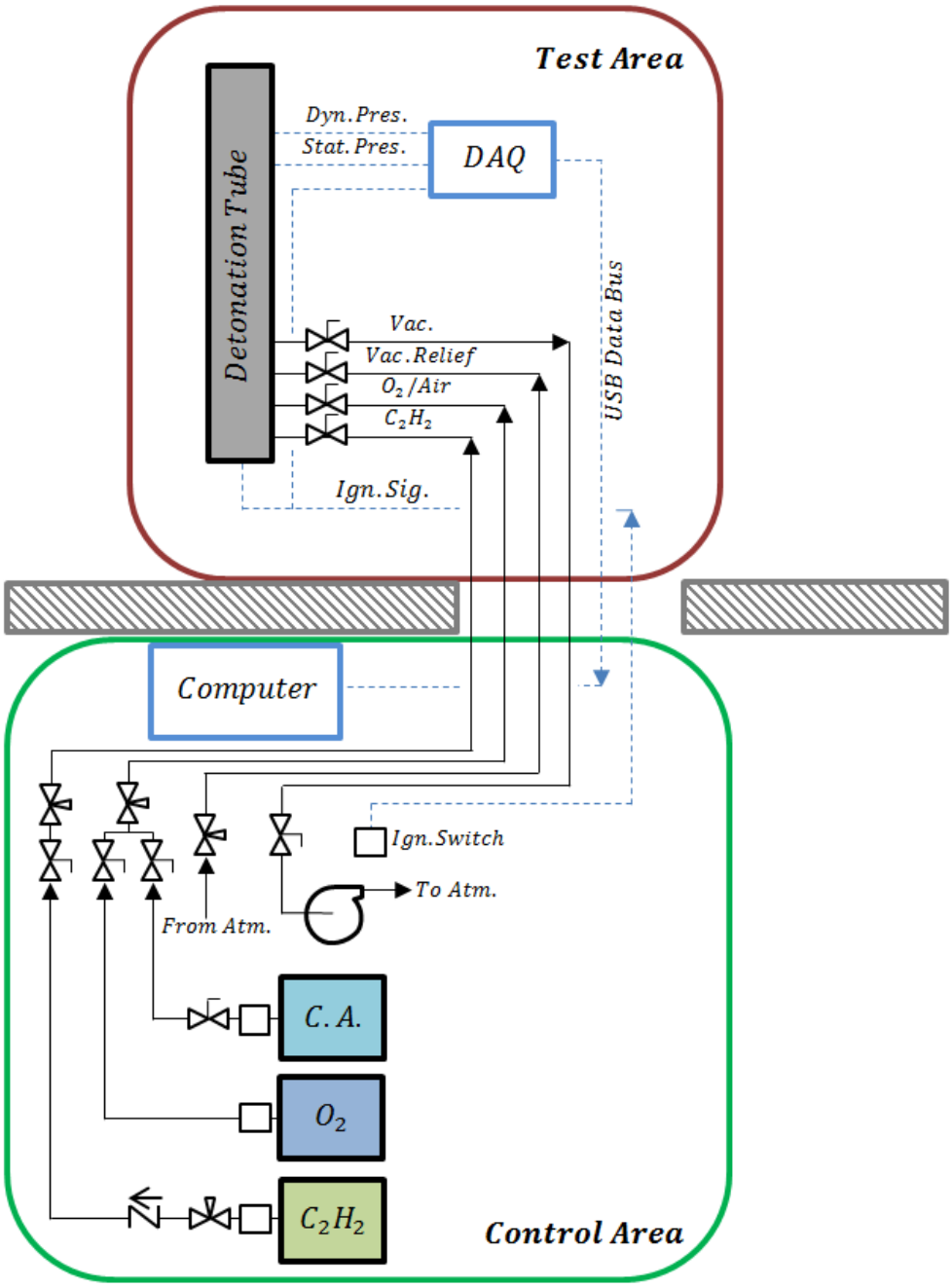

Figure 5.1. Detonation tube facility schematic. The facility is divided into two main areas – test and control.

Operating Procedure Overview

The test process begins by installing a thin plastic diaphragm which is used to separate the reactive section from ambient conditions. The diaphragm material used was 0.001" transparent Mylar sheet. This material was selected since it robust enough to not rupture during evacuation but will present minimal disturbance to the flow during the detonation event, and is in common use with many similar experiments [26,51,52]. Once the diaphragm is installed, the reactive volume is evacuated of ambient air using a rocking piston type vacuum pump (Ulvac Model DOP-80S). The reactive section was typically evacuated to a very coarse vacuum, $P_{evac} \approx$ 1 psia, which allowed for adequate control of detonable mixture composition. This evacuated section was then manually refilled with C_2H_2, O_2, and air to attain the desired fill pressure (P_{fill}), equivalence ratio (ϕ), and nitrogen content (N_2/O_2) using a partial pressure method [53–56]. The test section was ignited using a modified automotive ignition circuit built from off-the-shelf parts. As mentioned before, this ignition circuit also served as a trigger for a finite, high-speed data sampling to capture the detonation event.

Note that no mixing procedures are used to ensure homogeneity of the detonable mixture. Some sort of mixing mechanism is common in many single shot experiments [26,53,56]. However, it was omitted from the present work due mainly to cost restrictions. The effects of no mixing will be discussed fully in Section 5.2.

Design of Baseline Detonation Tube

To reiterate, a detonation tube is an apparatus which consists of a tube which is filled with a detonable mixture, ignited at a closed end, and generates a detonation wave which travels out through an open end. When ignited, the reaction begins as a deflagration but transitions to a detonation due to the reaction's confinement within the tube, with this process being known as Deflagration-to-Detonation Transition (DDT). The distance time taken to transition depends on the mixture and tube geometry (diameter, length, wall roughness) [57].

With this in mind, the original vision of the baseline detonation tube was to have a relatively large diameter, smooth tube with modular interfaces to accommodate the addition of a diffuser. This baseline configuration could be self-standing experiment used for shakedown and characterization. A larger diameter tube was desired since it would place emphasis on wave

dynamics and minimize frictional effects. The baseline tube would consist of two sections of tube to mate at a flange interface, such that one or both could be filled with detonable mixture. This would allow for investigations of a fully filled or partially filled tube.

Machine drawings for the Phase 1 baseline are shown in Figure 5.2, illustrating that the Phase 1 baseline consists of two sections of lengths $L_1 \approx 36$ [in] and $L_2 \approx 42$ [in]. Transducer ports for the dynamic pressure transducers are spaced throughout these sections. Also, these sections have sundry butt welded, compression tubing access ports for evacuation, fuel-oxidant addition, and pressure relief. Sections will be interfaced using standard pipe flanges. In the present case, all flanges are of the weld neck type. High temperature graphite gasket material is used to provide a seal between flange faces. A photograph of the apparatus is shown in Figure 5.3.

Acetylene was chosen as the fuel for the present work since it is one of the most notably detonable hydrocarbon fuels [57,58]. Also, it has been included in many detonation research efforts over the years, meaning it has a large body of work surrounding its use and performance. Acetylene has been to shown to be a flexible fuel with regard to its detonation limits. That is, it is capable of detonating with larger concentrations of nitrogen, such as that of found in air, along with small concentrations. To this end, this experiment employs an evacuation pump and a pure oxygen supply to provide simple control of the oxidant composition. A common scale used to describe a detonable mixture is the detonation cell size, λ. A detonation cell refers to the pattern traced out by the transverse shock waves along the vessel containing the detonation front [1,2]. This parameter is useful since it indicates relative reactivity of a mixture, meaning smaller cell indicates a more reactive mixture. For stoichiometric acetylene-oxidant mixtures, the cell size varies from $\lambda_{air} = 11$ [mm] and $\lambda_{pure\ O_2} = 1$ [mm] [59].

Guidelines for selecting tube diameter and length are suggested by Chao et al. [60]. With regard to detonations confined in a tube, there only exists a lower diameter bound beneath which a detonation cannot be sustained. The conservative rule of thumb for this lower bound is $D_{min} = \lambda$, making the lower bound for the current work $D_{min} = \lambda_{air} = 11$ [mm]$= 0.433$ [in] [58,60,61]. Due to its availability, the author chose to use NPS 4" schedule 80 pipe made from 304 stainless steel. The diameter of this pipe far exceeds the minimum diameter requirement, $D = 3.826$ [in] $> D_{min}$. For length, Chao et al. suggest that the rule of thumb for DDT distance

is $L_{DDT} \approx 10\lambda$. However, perusal of the literation suggests that this is a vast generalization, and that DDT run-up distances are highly dependent on mixture composition and tube geometry [57,58,61,62]. That said, the author chose extremely conservative lengths compared to the general rule, such that $L_1 \approx 85\lambda$ and $L_2 \approx 100\lambda$.

Finally, let us consider the structural requirements for such an apparatus. Once more, the author followed the design guidelines suggested by Chao et al. [60]. Since a detonation provides a spatially and temporally non-uniform load on a pipe, using the static, hoop stress formulation is not quite suitable. Instead, the guideline incorporating the dynamic hoop stress is given as

$$\sigma_H = \Phi \frac{\Delta P_{CJ} * R}{t} \leq \frac{\sigma_Y}{SF}, \qquad \textbf{5.1}$$

where σ_H is the hoop stress in the pipe, Φ is the dynamic amplification factor, $\Delta P_{CJ} = P_{CJ} - P_{fill}$ is the difference in CJ and fill pressures, R is the mean radius of the tube, t is the thickness of the tube, σ_Y is the yield strength of the tube's material, and SF is the factor of safety. Beltman and Shepherd showed that the amplification factor can at most achieve $\Phi = 4$ for a detonation exciting the structure at resonance [63]. Using this value and the reference values for $R, t, \Delta P_{CJ}$, and σ_Y, the factor of safety for the current apparatus was a conservative $SF = 4.75$. Also note that this is not a true multi-shot PDC, thus making fatigue loading of minimal concern.

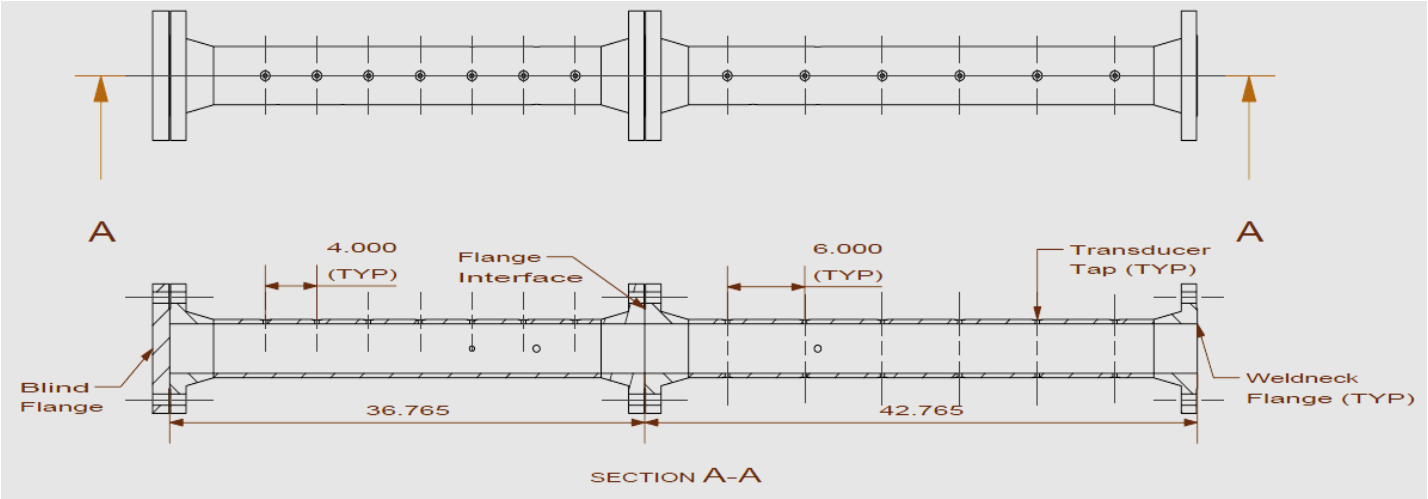

Figure 5.2. Machine drawing of the Phase 1 baseline. Dimensions in inches.

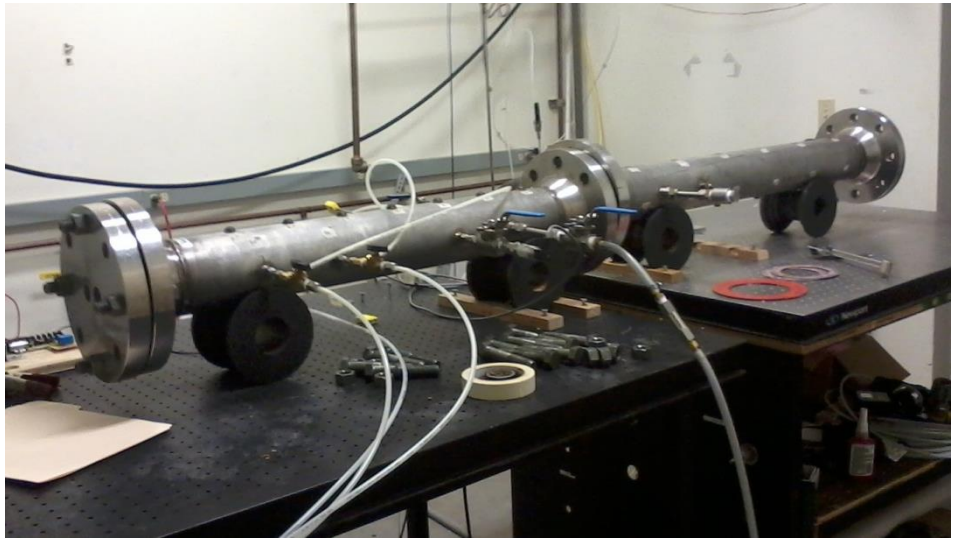

Figure 5.3. Photograph of the Phase 1 baseline apparatus. The device rests on rollers to aid in assembly and disassembly procedures. Photo by author, 2014.

Instrumentation, Data Acquisition

The National Instruments USB 6356 DAQ was used for all data sampling in the present work. This device can simultaneously sample eight analogue inputs at a maximum sampling frequency of $f = 1.25$ MHz, using a 2 MS onboard memory as a buffer. This device is also equipped digital/analogue data acquisition triggering. This DAQ was interfaced with two different LabView Virtual Instruments (VI's): one for the evacuation and filling processes (low-speed sampling), the other for the detonation event (high-speed sampling).

For the evacuation and filling processes, the pressure within the test section was monitored using a conventional, strain gage type, static pressure transducer (Omega PX319-030A5V). The Omega model used has a 0 – 30 psia range and a 0 – 5 V output signal. The filling pressure within the test section was monitored and recorded at a sampling rate $f = 50$ Hz. The recorded data could later be post-processed to estimate the amount of air leaked into the section during the sub-atmospheric filling process.

For the detonation event and subsequent blowdown, pressure was measured using high-speed, piezoelectric, dynamic transducers (Dytran Model 2300V). The dynamic transducers used have a 0 – 500 psi dynamic range and a 0 – 5 V output signal range. Their response characteristics include a resonant frequency $f_n = 500$ kHz and a response time $t_{resp} < 1\ \mu s$, ideal for detonation measurement scenarios. That said, piezoelectric transducers are notably susceptible to negative signal bias caused by high temperatures. High temperatures influence both the pyroelectric response of the transducer crystal and the pre-set stress on the crystal [64]. That is, high temperatures cause the transducer casing to expand, relieving the pre-set stress on the crystal pressure-sensing element. To help combat this effect, transducer faces are coated with nylon electrical tape. This simple solution is endorsed by the manufacturer and noticeably improves the fidelity of the pressure signal [65]. As an obvious illustration of the effects, Figure 5.4 is a plot comparing dynamic pressure signals with (black) and without (red) the protective coating. PCB Model 482C signal conditioners were used to both power and remove the DC component to the dynamic pressure signals. These dynamic pressure transducers are dual purpose: they provide both pressure histories at a given location and can be used in measuring average wave speed between measurement points i.e. Time of Flight (TOF). Post processing methods are discussed along with results in the next section.

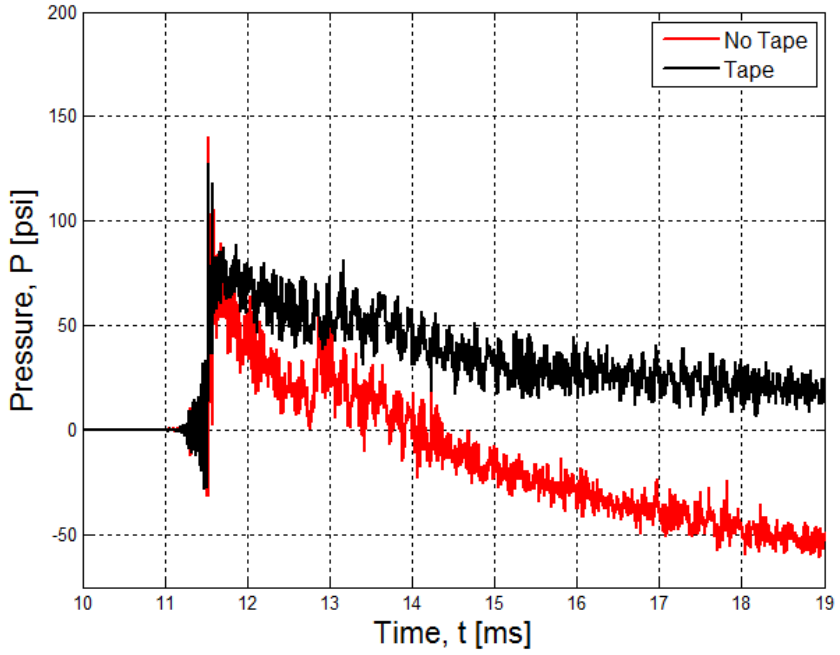

Figure 5.4. Plot comparing pressure signals which have (black) and have not (red) been covered with a layer of nylon tape.

Omission of Temperature Measurements

Unfortunately, given the extreme conditions created by the pulse detonation event, implementing an accurate, cost-effective temperature measurement scheme is impossible. Figure 5.5 illustrates a sample temperature profile (black) at the outlet taken from a Diffraction-Reflection CFD simulation. Note the short time scale (< 1 ms) and wide range of high temperatures (800 < T < 2000 K) characteristic of this type of flow. Shown for comparison is the model response of an ideal thermocouple (blue). This model assumes an unchanging time constant which was derived based on convective heat transfer to a sphere and a lumped capacitance model. Even though this plot depicts idealizations in true and measured profiles, it clearly illustrates the fact that a single thermocouple does not possess the dynamic characteristics to accurately measure the flow. This point is furthered by the fact that the literature rarely makes mention of temperature measurement in pulse detonation research, with the exception of Tunable Diode Laser Absorption Spectroscopy (TDLAS) and time-averaged thermocouple temperature measurements [11,49,50].

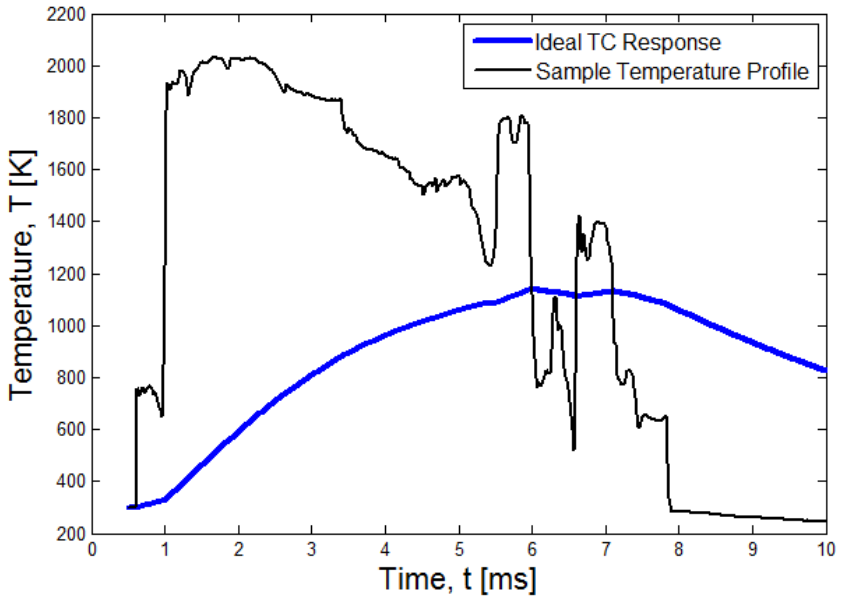

Figure 5.5. Ideal thermocouple response to a sample temperature profile taken from a Diffraction-Reflection diffuser CFD simulation.

To improve the dynamic response, several studies have investigated using multiple thermocouples of different size to reconstruct the temperature field using a real time Kalman filter. Such schemes make no assumptions a priori about the probe's time constant. Although these techniques can drastically improve the dynamic response of a thermocouple, they require a start-up period and still do not meet the temperature range requirements of a pulse detonation flow field [66–68]. That said, it is possible that these compensated thermocouple schemes could be implemented in a multi-shot experiment, but are not suited for the single shot experiment presented here.

Partial Filling Methodology

Mixture composition was determined by measuring the partial pressures of air, oxygen, and fuel injected in the tube. In this application, since the oxidant is not naturally occurring air but a comparatively oxygen-rich oxidant, the equivalence ratio is defined using pure oxygen content,

$$\phi = \frac{\frac{n_{fuel}}{n_{oxygen}}}{\overline{f_{st}}}. \qquad 5.2$$

In Equation5.2, n is the number of moles of fuel or oxygen and $\overline{f_{st}}$ is the stoichiometric molar ratio of fuel to oxygen. In this case, $\overline{f_{st}} = 0.4$. By assuming ideal gas relations and constant volume and temperature, the nominal equivalence ratio can be computed by partial pressures according to

$$\phi_{nom} = \frac{\frac{n_{f,nom}}{n_{O_2,nom}}}{\overline{f_{st}}} = \frac{1}{\overline{f_{st}}} \frac{PP_{f,nom}}{PP_{O_2,nom}}, \qquad \textbf{5.3}$$

where PP is the partial pressure of fuel and oxygen. In this case, the only fuel in the system is that which is added, meaning $PP_f = P_{f,add}$. However, oxygen is both found in the residual vacuum pressure and added to the system. As such, $PP_{O_2} = 0.21 * P_{evac} + P_{O_2,add}$, where P_{evac} is the final evacuation pressure. This experiment was designed such that $P_{evac} \approx 1\ psi$, meaning the residual oxygen and nitrogen content cannot be discounted. Oxygen can be added either as pure molecular oxygen or as a portion of air. To this end,
$P_{O_2,add} = P_{pure\ O_2,add} + 0.21 * P_{air,add}$.

The nitrogen content of the system is measured by the nitrogen to oxygen ratio, $(\frac{N_2}{O_2})$. Obviously, for air as an oxidant, $\left(\frac{N_2}{O_2}\right) = 3.76$. However, in these experiments, an oxygen-rich oxidant will be used. Similar to the equivalence ratio, the nominal nitrogen-to-oxygen ratio can be computed using partial pressures by

$$\left(\frac{N_2}{O_2}\right)_{nom} = \frac{n_{N_2,nom}}{n_{O_2,nom}} = \frac{PP_{N_2,nom}}{PP_{O_2,nom}} \qquad \textbf{5.4}$$

where PP once more denotes partial pressure. Nitrogen content is controlled via the final evacuation pressure and by the amount of air added to the system, meaning
$PP_{N_2} = 0.79 * (P_{evac} + P_{air,add})$.

Figure 5.6 is a sample pressure history taken from a Phase 1 filling process. Noted in this figure are the evacuation pressure (P_{evac}), added oxygen partial pressure ($PP_{pure\ O_2,add}$), added fuel partial pressure (PP_f), and the final fill pressure of the test section (P_{fill}). Also noted are the

durations for oxygen addition (τ_{O_2}), fuel addition (τ_f), and the resting time after filling has finished (τ_{rest}). These durations play a role in the filling error analysis presented next.

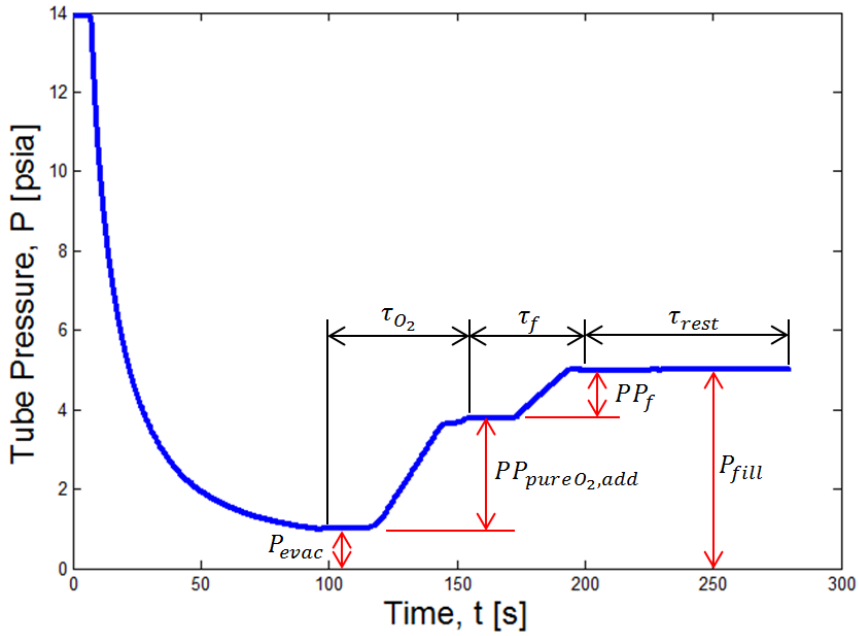

Figure 5.6. Typical pressure filling history of a Phase 1 experiment.

5.2 Phase 1 – Initial Baseline Shakedown, Characterization

Phase 1 – Test Conditions

Nominal Conditions

The nominal test conditions for Phase 1 are summarized in Table 5.2. The CJ detonation solution from the NASA CEA code are also listed for the mixture [69]. Since this was the initial phase of experiments, a low pressure, easily detonable mixture was selected. This mixture uses oxygen-rich oxidant which contains only residual nitrogen from the evacuation process ($(N_2/O_2)_{nom} = 0.263$, compared to $(N_2/O_2)_{air} = 3.76$). Note that the CJ pressure is relatively low ($P_{CJ} \approx 150$ [psi]) and well within in the range of the dynamic pressure transducers (0 to 500 [psi]).

Table 5.2. Mixture compositions and corresponding CJ detonation conditions.

		Phase 1
Mixture	P_{fill} ***[psia]***	5
	(N_2/O_2)	0.263
	ϕ	1
CJ Conds.	P_{CJ} ***[psia]***	147
	U_{CJ} ***[m/s]***	2272
	a_{CJ} ***[m/s]***	1231

Mixture Composition Error Analysis

Unfortunately, the mixture and CJ Conditions listed in Table 5.2 are nominal values which represent a perfect partial filling process with no error. In reality, error is introduced into the system by way of atmospheric air leakage and non-constant filling volume. Atmospheric air leakage occurs anytime the filling volume is at sub-atmospheric pressures. As such, air displaces a small portion of the added fuel and pure oxygen and acts as a source of nitrogen to the system. Also, in the derivation of the partial pressure method, the system was assumed to be constant volume. This is an idealization of the actual system due to the flexibility of the containment diaphragm. When the filling volume is at sub atmospheric pressures, the diaphragm stretches corresponding to the overall pressure difference which exists between the filling the volume and ambient conditions. The greater the pressure difference, the more diaphragm will deflect, and more of the tube volume it will displace. To this end, not only is the tube volume not constant, but it also changes as a function of the filling pressure.

Corrected equivalence and nitrogen-to-oxygen ratios incorporate these error sources. Corrected equivalence ratio is defined by

$$\phi_{corr} = \frac{1}{\overline{f_{st}}} \frac{n_{f,nom} + e_f}{n_{O_2,nom} + e_{O_2}} \qquad \textbf{5.5}$$

where e indicates the error in the moles of fuel and oxygen. Similarly, corrected nitrogen-to-oxygen ratio is

$$\left(\frac{n_{n_2}}{n_{O_2}}\right)_{corr} = \frac{n_{N_2,nom} + e_{N_2}}{n_{O_2,nom} + e_{O_2}}. \quad \textbf{5.6}$$

The error in the moles of fuel added, e_f, is described by

$$e_f = -\frac{V_{nom}}{RT}\int_{\tau_f} \dot{P}_{leak}\, dt - \frac{V_{dent,f}}{RT} PP_{f,nom} \quad \textbf{5.7}$$

where V_{nom} is the nominal tube volume, τ_f is the filing duration of the fuel, $\dot{P}_{leak}$ is the leakage rate into the tube, $V_{dent,f}$ is the volume displaced by the stretched diaphragm after fuel has been added, R is the universal gas constant, and T is the temperature in the test section. The first term in Equation 5.7 accounts for air which displaces fuel during the fuel addition period and the second term account for the fuel which is not added to the volume displaced by the stretched diaphragm. For this analysis, the leakage rate was assumed to be constant, $\dot{P}_{leak} = 5 * 10^{-4}$ [psi/s]. This value is characteristic of the apparatus during Phase 1 testing and was experimentally determined. The error in the number of moles of oxygen added, e_{O_2}, takes the form of

$$e_{O_2} = \frac{V_{nom}}{RT}\left[0.21\int_{\tau_f} \dot{P}_{leak}\, dt - 0.79\int_{\tau_{O_2}} \dot{P}_{leak}\, dt + 0.21\int_{\tau_{rest}} \dot{P}_{leak}\, dt\right] - \left[0.21\frac{V_{dent,evac}}{RT}P_{evac} + \frac{V_{dent,O_2}}{RT}PP_{O_2,nom}\right] \quad \textbf{5.8}$$

where τ_{rest} is the resting during of the experiment, and $V_{dent,evac}$ and V_{dent,O_2} are the volumes displaced by the diaphragm after evacuation has been completed and after oxygen has been added to the test section. As before, the first bracketed term represents oxygen which is gained or displaced by air which has leaked in the test section and the second term represents oxygen which is displaced by the stretched diaphragm. Similar to Equations 5.7 and 5.8, the error in the number of moles present in the test section can be computed by

$$e_{N_2} = 0.79\frac{V_{nom}}{RT}\int_{\tau_{total}} \dot{P}_{leak} dt - 0.79\frac{V_{dent,evac}}{RT}P_{evac} \quad \textbf{5.9}$$

where τ_{total} is the entire filling duration. As before, the first term corresponds to the nitrogen which leaks in with air and the second term accounts for the nitrogen displaced by the stretched diaphragm at the beginning of the filling process. One difference with Equation 5.9 compared to the others is that nitrogen is continually leaked into the test section, hence integrating over total time in the first term.

Applying the error terms to the definitions of corrected equivalence and nitrogen-to-oxygen ratios and simplifying, we arrive at

$$\phi_{corr} = \frac{1}{\overline{f_{st}}} \frac{PP_{f,nom} - \dot{P}_{leak} * \tau_f - VR_f * PP_{f,nom}}{PP_{O_2,nom} + \dot{P}_{leak}\left[0.21 * \left(\tau_f + \tau_{rest}\right) - 0.79 * \tau_{O_2}\right] - \left[0.21 * VR_{evac} * P_{evac} + VR_{O_2} * PP_{O_2,nom}\right]} \quad \textbf{5.10}$$

and

$$\left(\frac{N_2}{O_2}\right)_{corr} = \frac{PP_{N_2,nom} + 0.79 * \dot{P}_{leak} * \tau_{tot} - 0.79 * VR_{evac} * P_{evac}}{PP_{O_2,nom} + \dot{P}_{leak}\left[0.21 * \left(\tau_f + \tau_{rest}\right) - 0.79 * \tau_{O_2}\right] - \left[0.21 * VR_{evac} * P_{evac} + VR_{O_2} * PP_{O_2,nom}\right]}. \quad \textbf{5.11}$$

Here, the term VR is used the volume ratio of the volume displaced by the diaphragm to the nominal section volume at a given point in the filling process, meaning $VR = V_{dent}/V_{nom}$. It was also assumed that the temperature in the test section was constant during the filling process. The order of events for the Phase 1 filling process was evacuation, oxygen addition, then fuel addition. As such, the magnitude of the volume ratios correspond to this order, meaning $VR_{evac} > VR_{O_2} > VR_f$. In this analysis, it was assumed that $VR_{evac} = 0.050, VR_{O_2} = 0.037$, and $VR_f = 0.032$, where these values were based on observation and linear scaling according to pressure differential across the diaphragm.

This analysis has been applied with a post-processing approach using the recorded filling histories from each run. The corrected results are summarized in Table 5.3 and compared against nominal values. The corrected value for P_{fill} corresponds to the final pressure measured in the section after the filling process. Due to slight leakage, the actual final pressure was always greater than the nominal final pressure. It can be seen that the corrected fill pressure and equivalence ratio were quite close to the nominal values; however, the nitrogen ratio differed by a larger margin. Despite this difference in nitrogen content, the computed detonation parameters are insensitive to these corrected initial conditions. The corrected CJ conditions are so close to the nominal conditions that this slight difference exceeds the accuracy of the instrumentation

used. As such, this analysis suggests that the actual (corrected) test conditions are practically indistinguishable from the nominal test conditions, and thus will be treated as the same for the remainder of the analysis.

Table 5.3. Comparison of nominal and corrected mixture composition and CJ conditions. The error analysis suggests that the corrected CJ conditions would be indistinguishable from nominal conditions.

		Phase 1		
		Nominal	***Corrected***	***% Difference***
Mixture	P_{fill} ***[psia]***	5	5.07	***1.4***
	(N_2/O_2)	0.263	0.306	***16.4***
	ϕ	1	0.988	***1.2***
CJ Conds.	P_{CJ} ***[psia]***	147	148	***0.7***
	U_{CJ} ***[m/s]***	2272	2260	***0.5***
	a_{CJ} ***[m/s]***	1231	1224	***0.6***

Note that the corrected equivalence ratio remained close to the stoichiometric target because of the competing effects of the volume and leakage errors. Since the volume error tended to the make the mixture rich and the leakage error tends to make the mixture lean, these effects demonstrated some degree of cancellation.

Wave Speed Measurements

The dynamic pressure transducers used were valuable diagnostic tools in that they provided both pressure and wave speed data. Because the detonation and shock events are supersonic, a wave's passage is clearly indicated as a large spike in pressure at a measurement location. Figure 5.7 are sample pressure histories illustrating this point. One can compute an average wave speed, or Time of Flight (TOF), between two measurement points using the familiar formula

$$TOF = \frac{\Delta x}{\Delta t}, \qquad \textbf{5.12}$$

where Δx is the distance between transducers and the Δt is the transit time between transducers. The transit time of the wave can manually be determined by a point picking technique where the analyst subjectively determines when in the time the peak pressure occurs. However, this method

is not repeatable, does not incorporate any possibility for an error analysis, and relies heavily on human subjectivity.

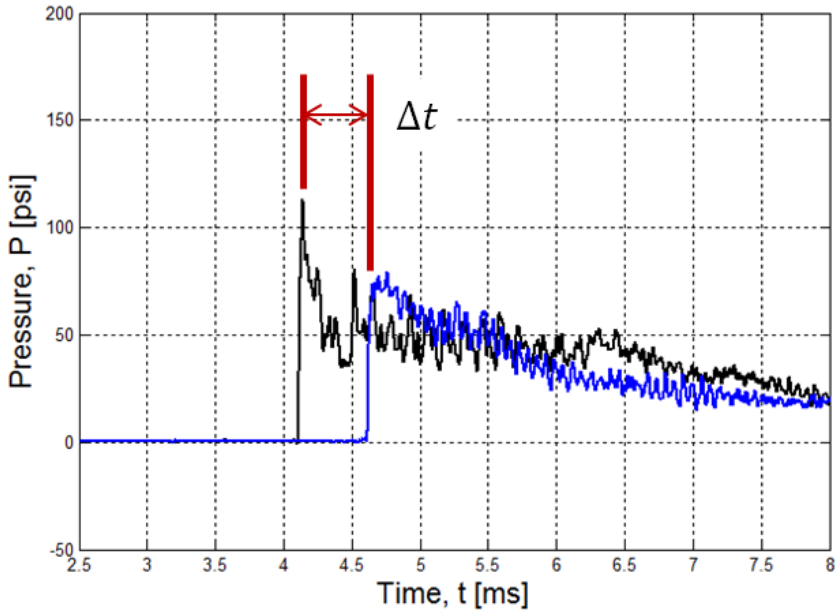

Figure 5.7. Sample pressure histories illustrating the delay between non-stationary signals.

Instead, a much improved approach for determining transit time is outlined by Lu et al. [70]. This method involves taking a series of non-stationary cross correlations over range of windows to compute the lag time between signals. Window ranges are selected such that they contain the non-stationary event(s) of interest, and a time lag is computed for each window. These are averaged to find a nominal transit time, τ, and the standard of deviation of these lags is used as error value, e_τ. This method still requires a subjective user input in the form of window selection. See the appendix for source code used.

Phase 1 – Full Fill Characterization

Included in Phase 1 shakedown were tests investigating wave dynamics in a fully filled tube. Figure 5.8 indicates pressure measurement locations and relative spacing. In these tests, detonations with characteristic CJ pressures and wave speeds were consistently detected. Note that these tests utilized no partial filling, meaning the entire test section was filled with detonable mixture shown in green in Figure 5.8.

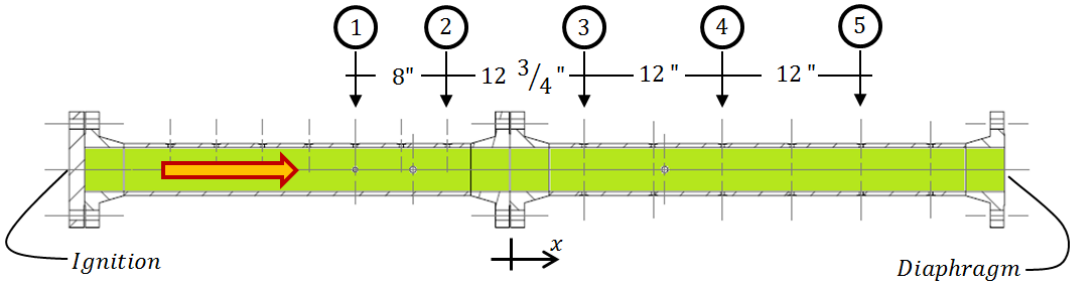

Figure 5.8. Dynamic pressure measurement locations and spacing for fully filled, Phase 1 tests.

Pressure Characterization

Figure 5.9 and Figure 5.10 are sample experimental pressure histories measured at Points 1 and 5 indicated in Figure 5.8. Both feature raw data (grey), filtered data (black or blue), and the CJ pressure (red) as a reference. Figure 5.9 is a strong example of canonical pressure history in a fully filled detonation tube. The data was recorded at measurement Point 3. In the plot, the pressure suddenly rises to approximately the CJ value and immediately decays to a plateau value due to the passage of the Taylor Wave. This plateau value seen on the plot is $P_{plateau} \approx 50$ [psi]. This value corresponds to $P_{plateau} \approx {}^{1}/_{3}\, P_{CJ}$ proposed by Wintenberger et al. [27]. This plateau period lasts until $t \approx 6.5$ [ms], when the pressure begins to decay back to ambient conditions.

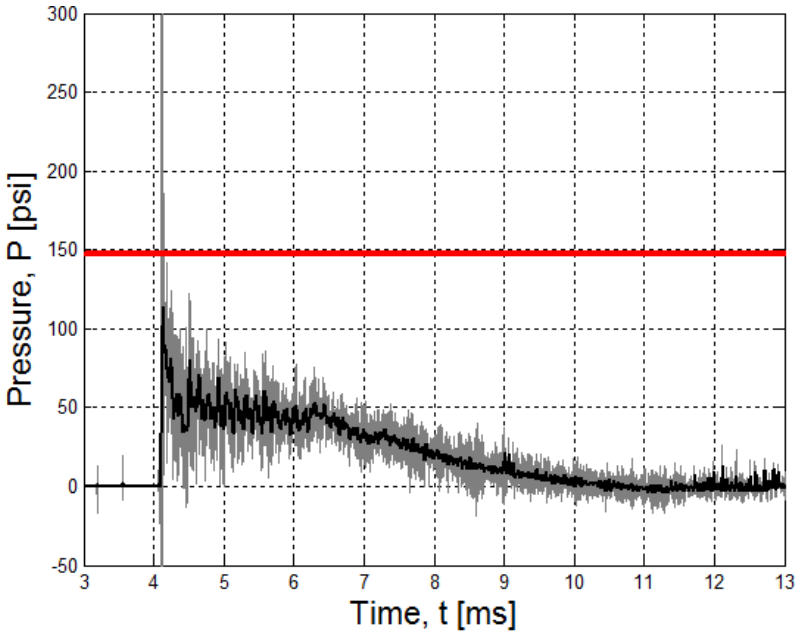

Figure 5.9. Full fill pressure history at Point 3 with both raw (grey) and filtered (black) data. Note that the pressure peaks around the expected CJ condition (red). Also, a characteristic pressure plateau and final decay follow the initial peak.

Figure 5.10 is a pressure history recorded at measurement Point 5 during the same experiment as Figure 5.9. The structure of this pressure trace fundamentally differs from the trace previously discussed. First, note that the peak pressure still approximately reaches the CJ value, but is much lower than the peak achieved in Figure 5.9. Also note the absence of a pressure plateau. This feature (or lack thereof) is characteristic of points closer to the tube exit. As the detonation exits the tube, it generates expansion waves which travel back into the tube toward the back wall. These exit expansion waves serve to drop the pressure and mark the beginning of the natural blowdown process.

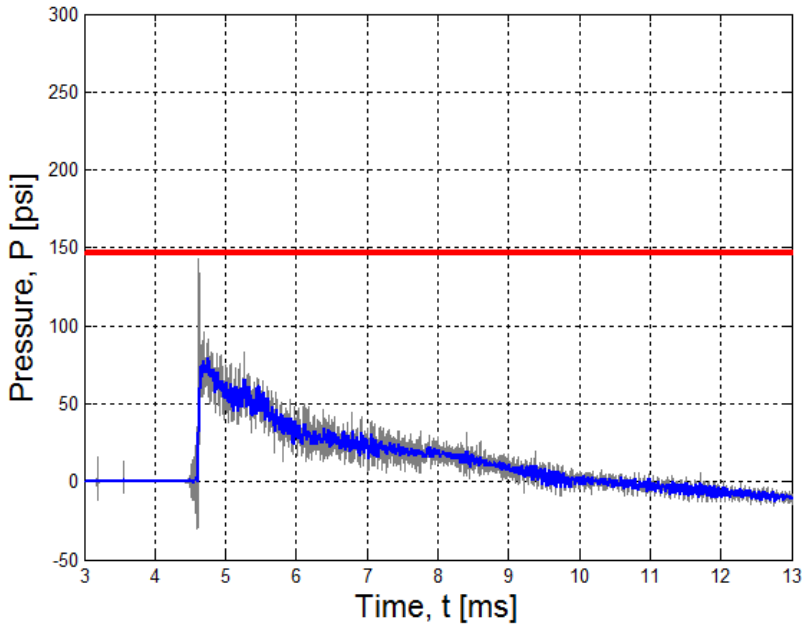

Figure 5.10. Full fill pressure history at Point 5 with both raw (grey) and filtered (blue) data. Peak pressure is much lower than in Figure 5.9. Minimal pressure plateau observed due to measurement location near the tube opening.

Wave Speed Characterization

Figure 5.11 is a plot of TOF Mach Number (TOFMN) as a function of tube position. Here,

$$TOFMN \equiv \frac{TOF}{a_0}, \qquad \textbf{5.13}$$

where is a_0 is the ambient speed of sound and was assumed to be $a_0 = 343$ [m/s]. Tube position, x, was normalized by the tube diameter to yield a dimensionless position, (x/D), where $D = 3.826$ [in]. The position origin was selected as the mid-tube flange interface (shown in

Figure 5.8). The value of (x/D) used for each measurement is the average of the transducer measurement locations. Included in the figure is the accepted CJ wave speed range corresponding to $\pm$ 10% U_{CJ} for a given mixture [2,57]. That is, a detonation is said to meet the CJ criteria as long as its wave speed falls within this range. For Phase 1, this range is

$$U_{CJ,min} = 2045 < TOF < U_{CJ,max} = 2500 \text{ [m/s]}$$

for TOF measurements and

$$M_{CJ,min} = 5.96 < TOFMN < M_{CJ,max} = 7.29$$

for TOFMN.

Because the test apparatus is single shot only, the data points in the figure indicate the average TOFMN taken across four separate experiments. It is clear that all of the TOFMN measurements fall within the accepted CJ range. However, it is evident that the wave is slowing down as it travels along the tube as the data shows a negative trend. This slowing of the wave can be attributed to insufficient mixing in the full fill configuration. Fuel and oxygen are admitted in that order at points near to the back wall of the tube. To this effect, one may assume that the mixture near the back wall was closer to the intended stoichiometric conditions than the mixture near the open end which was evidently lean. In other words, an equivalence ratio gradient caused the detonation to decelerate as it traveled toward the open end of tube. If the mixture were uniform and stoichiometric, the wave speed would be constant for all (x/D).

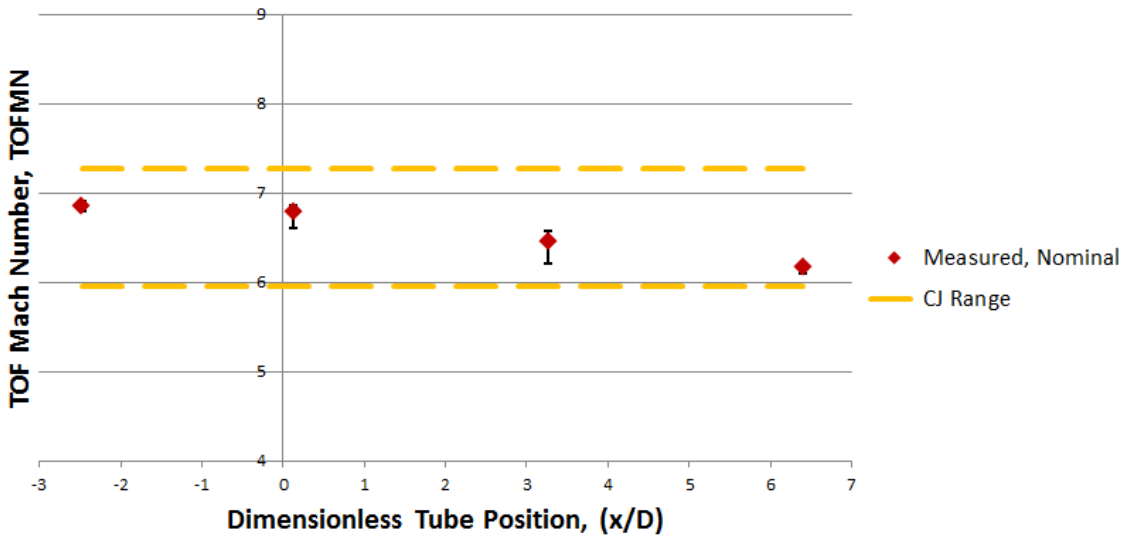

Figure 5.11. TOF Mach Number vs. Tube Position for Phase 1, full fill tests. While all measurements lie within accepted CJ range, the wave is clearly slowing as it approaches the tube opening.

Because of the relatively small number of tests performed (in this case, $n = 4$), the error bars in Figure 5.11 are simply the maximum and minimum TOFMN recorded at that position across all cases. This plot suggests strong repeatability from test to test despite possible variations during the manual filling procedure or in the deflagration-to-detonation transition process.

Conclusions

Pressure and wave speed characterization indicate the detonation tube is operating as anticipated. Pressure histories quantitatively and qualitatively match the expected wave dynamics and TOF measurements indicate that CJ detonations can be achieved. However, both the pressure and wave speed diagnostics indicate that an equivalence ratio gradient exists within the test section, causing the peak pressures and wave speeds to decrease as the detonation travels out of the tube.

Phase 1 – Partial Fill Characterization

After full fill tests concluded, the author began characterizing the detonation tube when partially filled with detonable mixture. For these tests, the apparatus is less than half-filled, corresponding to a fill fraction of $\sim 45\%$. Figure 5.12 illustrates the apparatus configuration, with green indicating detonable mixture and blue indicating ambient air. The ignition location remains unchanged from before, but now the containing diaphragm has been moved to the mid-tube

flange interface. In this set up, the detonation forms near the back wall, meets the reactive-inert interface, and decays as it exits the tube.

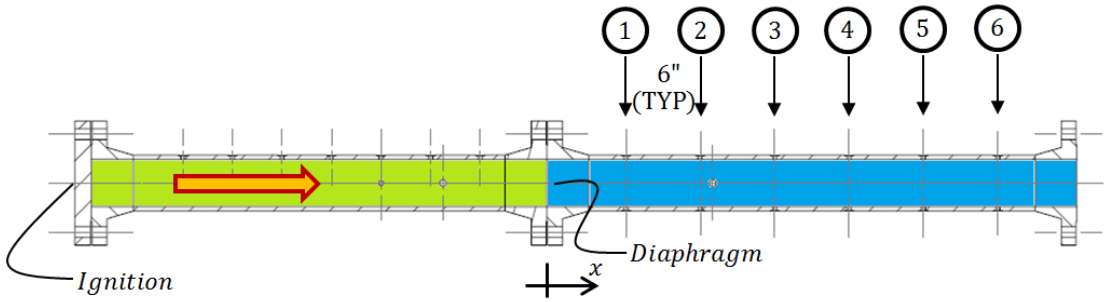

Figure 5.12. Dynamic pressure measurement locations and spacing for partially filled, Phase 1 tests.

Pressure Characterization

Figure 5.13 is a pressure history from Point 1 in the partial fill configuration located in the inert section of the tube. The histories shown in Figure 5.13 and Figure 5.14 are plotted on the same axis scale as the previous pressure histories to serve as a point of comparison. The sudden pressure spike indicates that the detonation initiated in the reactive section and has refracted into the ambient air. After the refraction, the detonation has become a decaying shock wave traveling out of the tube. The peak pressure in Figure 5.13 is comparable to the CJ value although weaker than the pressures seen in the full fill configuration. Also, a pressure plateau is still observed like in the full fill set up, however it is lower in magnitude ($P_{plateau,partial} \approx 25$ [psi], compared to $P_{plateau,full} \approx 50$ [psi]).

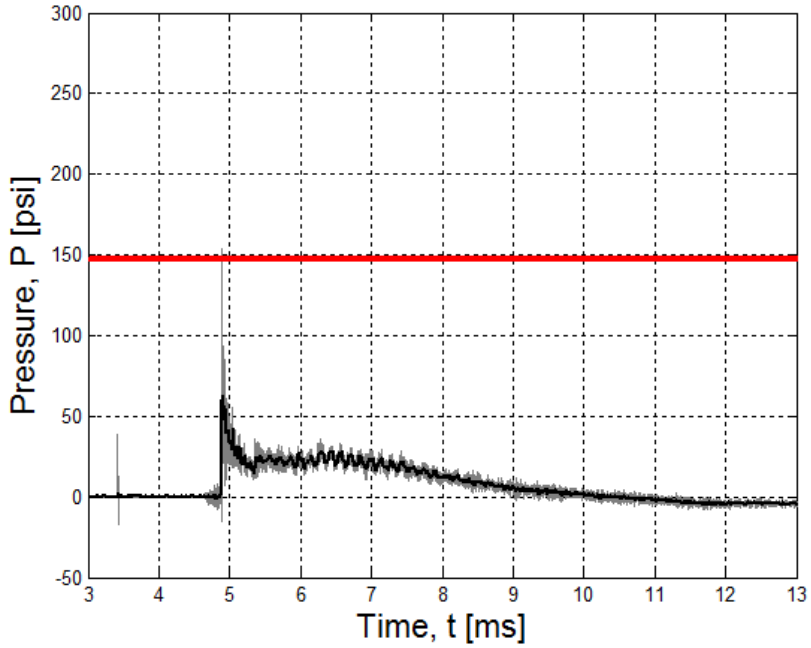

Figure 5.13. Half fill pressure history at Point 1 with raw (grey) and filtered (black) data. The peak pressure is much lower than CJ value (red), however a pressure plateau is still observed.

Figure 5.14 is a pressure history from measurement Point 5 and further illustrates the point that the wave is decaying as it transits the tube toward the opening. The peak pressure in the figure is substantially less the CJ value, only reaching $P_{peak} \approx 50$ [psi]. That said, a pressure plateau still exists following the initial peak and is unchanged from the previous measurement point. Figure 5.14 also suggests the existence of secondary waves in the tube, seen at $t = 6.2$ and 6.8 [ms]. The exact origin of these waves is unclear; however, the author speculates that they are remnants of the retonation wave from the deflagration-to-detonation transition.

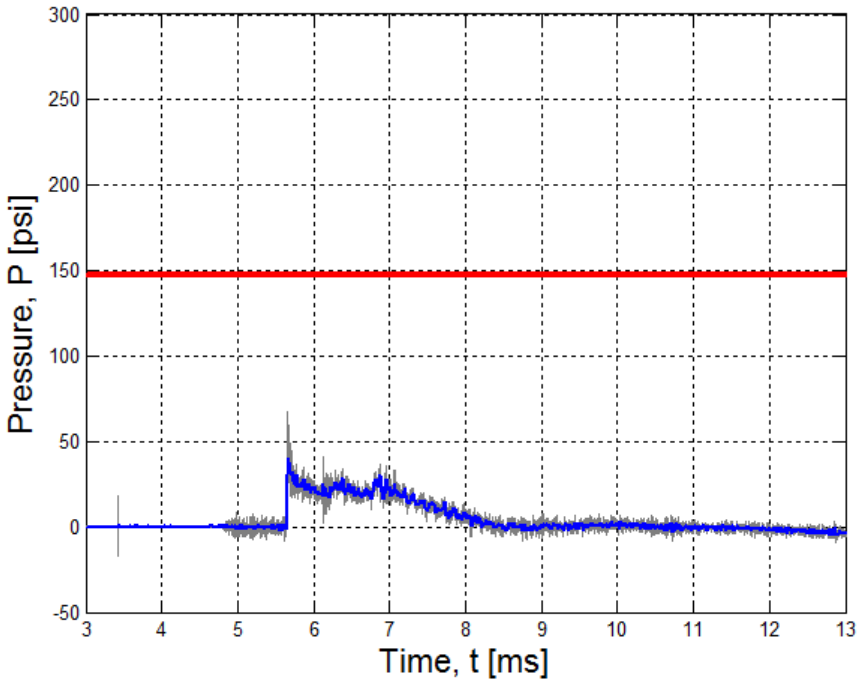

Figure 5.14. Half fill pressure history at Point 5 with raw (grey) and filtered (blue) data. Wave has been substantially attenuated and two reflected waves are apparent at $t = 6.25$ and $t = 6.8$ [ms].

Wave Speed Characterization

To aid in wave speed characterization, Figure 5.15 is a plot of the measured TOFMN as a function of the tube position in the Phase 1 partial fill configuration. As before, the data points shown in the graph are the TOFMN values averaged across multiple tests, with the error bars being the maximum and minimum TOFMN values measured at a point across all tests. This plot clearly shows the deceleration and decay of the transmitted shock wave as in the partial fill scenario. This result matches the same qualitative conclusion made from the pressure histories. Unfortunately, unlike the full fill results, the experiment to experiment variation is evident from the size of the error bounds. Especially in the case of $(x/D) = 8.8$, the error bounds are so large that they encompass the nominal values from the previous two positions. The cause for this scatter is believed to be the variability of the unenhanced DDT process from experiment to experiment.

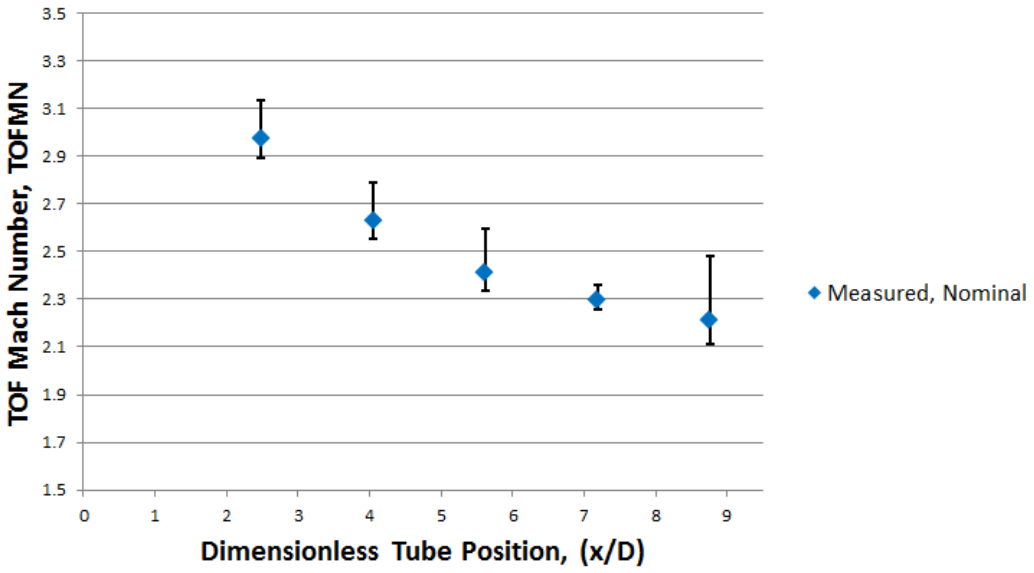

Figure 5.15. TOF Mach Number vs. Tube Position for Phase 1, partial fill tests. The data correctly indicate the wave is quickly decelerating as it approaches the tube opening.

To generate a more quantitative understanding, Figure 5.16 compares the experimental wave speeds against the wave speeds measured using results from the analogous CFD simulation. This simulation employed a simplified 2-dimensional geometry matching the Phase 1 test apparatus. Similarly, the initial pressure, temperature, and velocity profiles of this simulation were formulated using the exact Phase 1 CJ detonation parameters. The simulated wave speeds were measured using the same TOF method as in the experiments at locations corresponding to the measurement points in the actual apparatus. As the figure suggests, the measured wave speeds closely match the simulated wave speeds. Also shown in this plot is the solution to the ideal 1-dimensional refraction analysis discussed in Section 2.4. This point indicates the initial speed of the transmitted shock as the detonation refracts into the inert medium. This datum also shows strong agreement with both the experimental and simulated wave speed profiles.

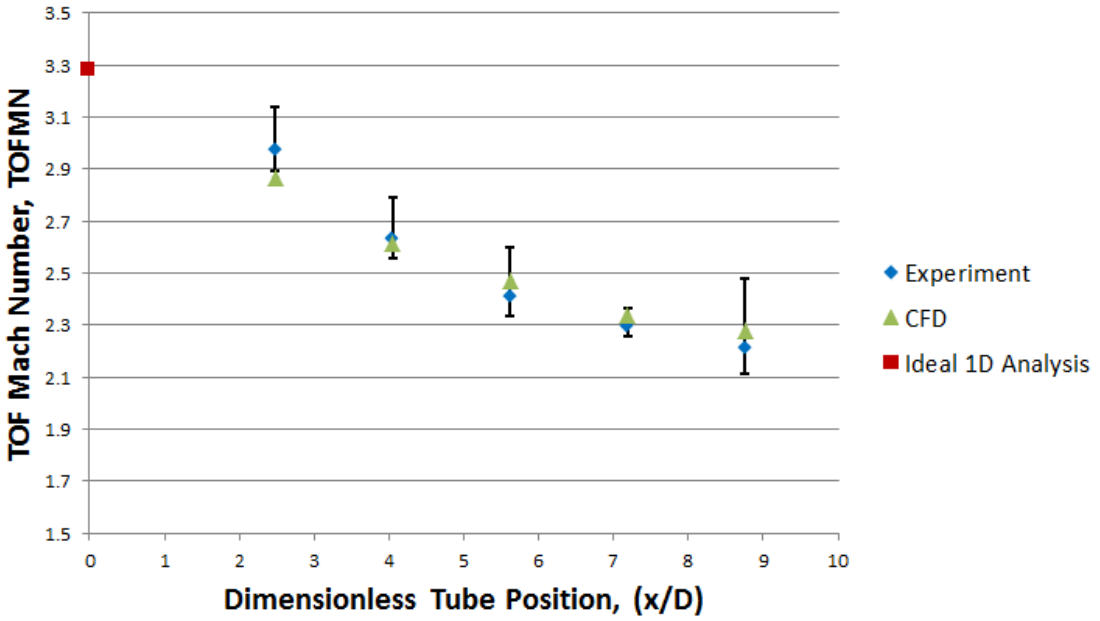

Figure 5.16. Comparison between experimental and simulated TOFMN in Phase 1. The experimental results show strong agreement with the simulated results. Also shown is the initial transmitted shock strength from the 1D refraction analysis.

Conclusions

The results from the partial fill testing agree with qualitative and quantitative predictions for a single shot detonation tube. Experimental results compare quite well with simulation and analytical results, clearly demonstrating the decay of the transmitted shock in a partial fill scenario. However, the wave speed measurements indicate a larger than desirable test-to-test variability. Before testing any diffuser prototypes, this variability must be improved upon.

5.3 Phase 2 – Baseline Modification

Motivation for Modifications

Results from the Phase 1 shakedown and testing showed encouraging results but also highlighted several areas of improvement for the detonation tube test apparatus. First, preliminary tests indicated the baseline apparatus would not be able to detonate using air as an oxidant. Recall that the Phase 1 test conditions used an oxygen-rich oxidizer consisting of very little nitrogen ($\left(\frac{N_2}{O_2}\right)_{nom} = 0.263$). The inability of the baseline rig to detonate with air is attributable to the non-optimized geometry which was selected. In order to accurately replicate the physics of a practical PDC, the detonation tube must operate with either air or a valid

substitute. Second, the partial fill wave speed measurements had large test-to-test scatter as illustrated in Figure 5.16. It is believed that variability in the DDT process and thus the initial conditions of the partial fill was the cause in this test-to-test scatter. In order to accurately assess diffuser performance, the baseline detonation tube must perform as consistently as possible.

Addition of Predetonator

A pre-detonator or initiator is an extension of a PDC in which a detonation is initiates and then transitions to the larger tube/section. An initiator may contain a more detonable mixture or employ a geometry optimized for the fastest possible DDT process [71–73]. Figure 5.17 is a machine drawing of the pre-detonator designed and added to the baseline apparatus. It consists of a length of small diameter tube with a Shchelkin spiral inserted. The use of a spiral or other turbulence generating devices greatly promotes the DDT process, and has been employed by countless researchers studying detonation physics and PDC's [11,14,50,74,75]. As before, the ignition source is an automotive type spark plug which is located near the back wall of the pre-detonator. The length and diameter of the extension were selected based on empirical design standards suggested by previous researchers which takes into account the composition of the mixture to be detonated [58,62,76]. In this case, this mixture is acetylene-air at stoichiometric proportions at an atmospheric fill pressure ($C_2H_2 - air$, $\phi = 1$, $P_{fill} = 1$ [atm]). To help the detonation transition from small to large diameters, a conical expander was installed in the large diameter section. The angle of this expander, α, was selected based on design recommendations from Sorin et al. [76]. Figure 5.18 and Figure 5.19 depict the new assembly as whole and provide context as to the pre-detonator's place and function.

To ensure that a stoichiometric mixture exists near the spark region, an injection ball valve was installed along the pre-detonator extent. The injection valve alters the operating procedure accordingly:

- The test section is evacuated to the minimum pressure as in Phase 1.
- The injection is valve is shut, isolating the spark volume from the filling process.
- The filling volume is overfilled with fuel and oxidant to some overpressure corresponding to the ratio of spark to filling volumes, $P_{fill,over} = P'_{fill} > P_{fill}$.

- The injection valve is opened, sending the mixture back to the spark region. The pressure settles to the final fill pressure, P_{fill}.

Other Modifications

Other modifications to the apparatus were simple but effective. In particular, welded joints were totally sealed with the addition of epoxy. This simple solution eliminated leakage error to zero. Also, the excess tubing was removed to minimize possible capacitance error during the filling process.

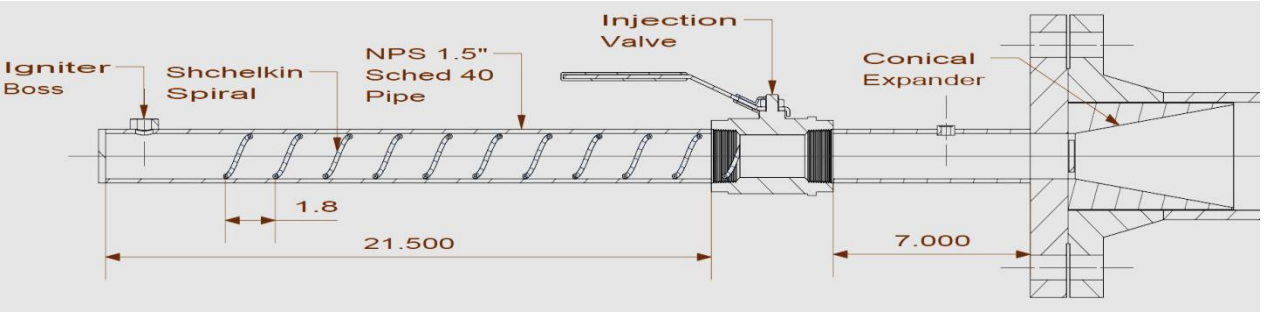

Figure 5.17. Machine drawing of the predetonator extension added to the baseline configuration during Phase 2. This device uses a Shchelkin spiral as a DDT enhancer and also employs a conical insert to help transition the detonation from the extension to the main section.

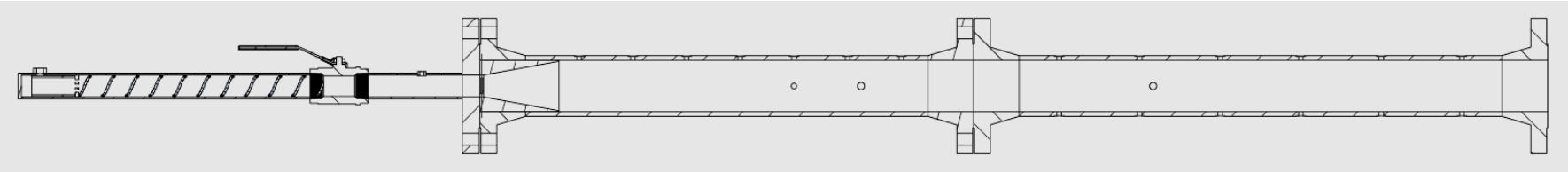

Figure 5.18. Technical drawing of Phase 2 modified baseline.

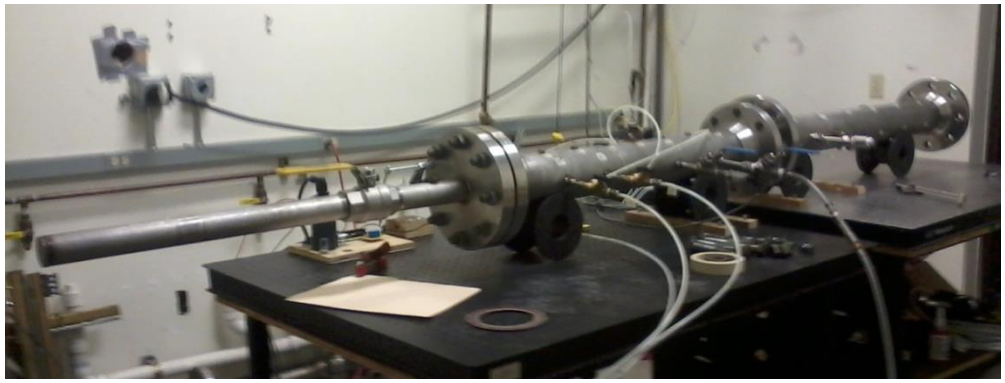

Figure 5.19. Photograph of the modified apparatus. Photo by author, 2014.

5.4 Phase 2 – Modified Baseline Shakedown, Characterization

Air as Oxidizer

Despite the very careful design of the pre-detonator extension, all attempts to detonate with air as an oxidant were unsuccessful. Over 30 tests with 7 different permutations of test apparatus hardware were attempted. In the interest of time and effort, the author decided to explore alternative mixtures which would be more detonable than an air mixture but would replicate the wave dynamics of interest.

Phase 2 – Test Conditions

As explained above, the original plan was to test diffuser concepts using a fuel-air mixture. However, due to many practical issues, a suitable alternative mixture needed to be determined. This alternative needed to be more reactive than a fuel-air mixture but replicate the wave dynamics of a PDC partially filled with a fuel-air mixture. Discussed in Section 2.4, the solution of a one-dimensional detonation refracting into air can result in either a reflected expansion wave or shock wave, depending on the CJ condition of the detonation front. If the CJ state lies above the shock adiabat in the $P - u$ domain, the reflected wave is an expansion. If the CJ lies below the adiabat, the reflected wave is a shock. Figure 5.20 is a plot of the shock adiabat in terms of pressure gain across the wave (P/P_0) versus normalized post-shock velocity (u/a_0). The red point on this graph is the CJ state for the nominal Phase 1 test conditions. Note that it lies in the region below the adiabat, indicating that it falls in the reflected shock solution regime. The blue point on this graph is the CJ state for a fuel-air mixture. Note that it lies above the adiabat, indicating that it falls in the reflected expansion wave solution regime. The solution of the alternative mixture must also fall in this same regime.

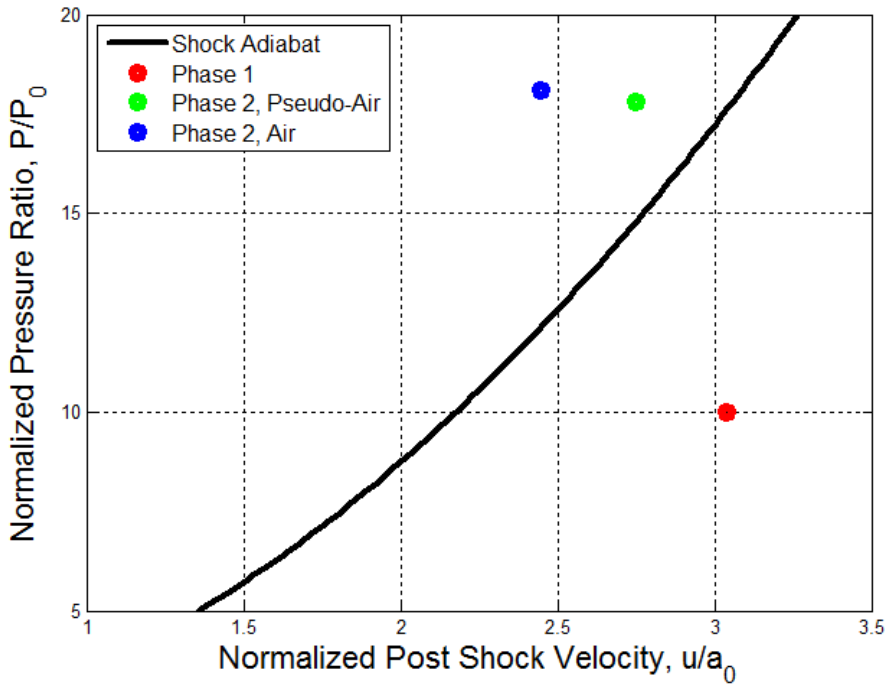

Figure 5.20. Shock adiabat with CJ states from Phases 1 and 2.

In the end, the author arrived on the alternative composition summarized in Table 5.4. The alterative oxidant has been termed "pseudo-air". This composition has a nitrogen-to-oxygen ratio of $(N_2/O_2)_{nom} = 1.484$, markedly lower than the ratio for air. However, the lowered nitrogen content makes the pseudo-air mixture more easily detonable than the comparable air mixture. The fill pressure was chosen such that the CJ pressure would closely match the CJ pressure of a fuel-air mixture with $P_{fill,air} = 14$ [psi]. As such, $P_{fill,pseudo} = 11$ [psi]. The CJ state of the pseudo-air mixture is also plotted in Figure 5.20 for comparison. Note that the pseudo-air CJ state has a faster particle velocity compared to air. However, the point lies in the appropriate region.

Table 5.4. Comparison of test conditions between Phase 1, Phase 2/3 and a fuel-air mixture. The pseudo-air mixture is more reactive the air mixture, achieves a comparable CJ pressure, and accurately replicates the wave dynamics.

		Phase 1	*Phase 2/3 (Pseudo-Air)*	*Air*
Mixture	P_{fill} *[psia]*	5	11	14
	(N_2/O_2)	0.263	1.484	3.76
	ϕ	1	1	1
CJ Conds.	P_{CJ} *[psia]*	147	261.2	266
	U_{CJ} *[m/s]*	2272	2070	1866
	a_{CJ} *[m/s]*	1231	1127	1026

Phase 2 – Partial Fill Characterization

For Phase 2, the author only investigated a partial fill configuration. Unlike Phase 1 partial fill characterization, wave speed measurements were made in both the reactive and inert portions of the apparatus. Figure 5.21 illustrates the apparatus configuration for this battery of tests, where green indicates the detonable mixture and blue indicates ambient air.

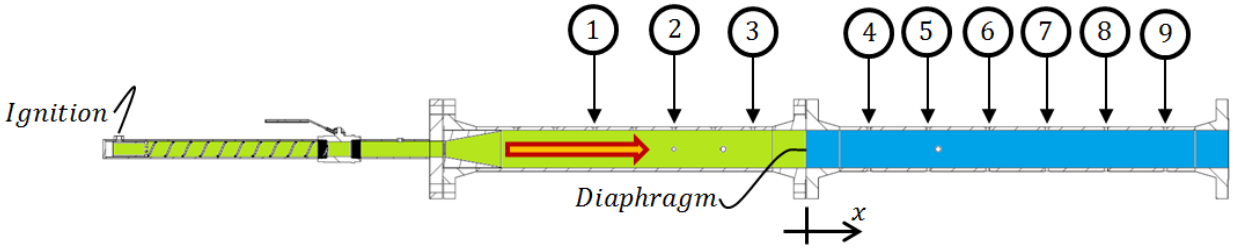

Figure 5.21. Dynamic pressure measurement locations and spacing for Phase 2 tests.

Wave Speed Characterization

Figure 5.22 is a plot the measured TOFMN versus tube position for the Phase 2 tests. The plot contains detonation and transmitted shock wave speeds, with the data points being the average and error bars being the maximum and minimum across three tests. For the detonation wave speed measurements, the yellow dotted line indicate maximum and minimum CJ speeds corresponding to $U_{CJ,min} = 1863$ [m/s] and $U_{CJ,max} = 2277$ [m/s]. The plot shows that all detonation TOFMN measurements fall within this accepted range, indicating a healthy

detonation. Inert wave speed measurements exhibit the expected decaying trend and excellent test to test repeatability. Note that the error bars are shown but not visible. This result validates the addition of the pre-detonator and shows it provided repeatable DDT enhancement. It is interesting to note the difference in magnitude between the detonation and transmitted shock wave speeds. The diffraction process halves the waves speeds over only three tube diameters, showing that even modest partial filling can provide some detonation diffusion.

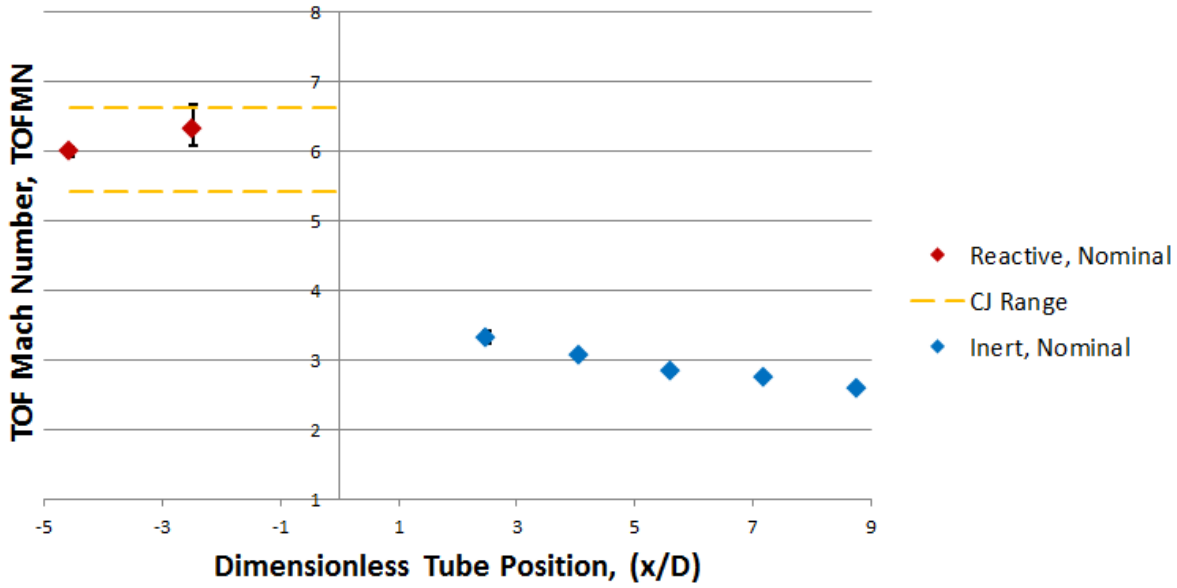

Figure 5.22. TOF Mach Number vs. Tube Position for Phase 2, partial fill tests. Detonation wave speeds meet the CJ criteria and the inert wave speeds measurements show excellent repeatability from test to test.

Figure 5.23 compares the experimental measurements against analogous data taken from 2 CFD simulations as before. The first simulation used pressure, temperature, and velocity profiles corresponding to a stoichiometric acetylene-air mixture with $P_{fill} = 14$ [psia] (purple) and second using profiles corresponding to a stoichiometric acetylene-pseudo-air mixture with $P_{fill} = 11$ [psia] (green). Also shown in the figure is the solution to the ideal one-dimensional refraction analysis (red). The tube geometry specified in the simulations matches the geometry of the *unmodified*, Phase 1 apparatus, meaning the pre-detonator was not included in the simulation. Spatially resolving initial condition profiles to reflect the area divergence was deemed to be impractical. The result of using the un-modified geometry is evident in the figure as the experimental results show a clearly faster decay rate in wave speed. This result is not well understood, but it is believed that the strength of the Taylor expansion wave following the detonation front is influenced by the divergence in flow area. This discrepancy in decay rates

also can be attributed to the highly idealized initial conditions employed in the simulation. These initial conditions assume a perfect, CJ detonation instantly generated at the back wall of the tube. As a result, the initial pressure, temperature, and velocity profiles are piecewise and linear. In the actual apparatus, the reactive wave takes time to accelerate and transition to a detonation. Also, the simulation does not account for the presence of the plastic diaphragm. This diaphragm acts as a small yet real flow impedance which would serve to decelerate the detonation/transmitted shock in the experiment.

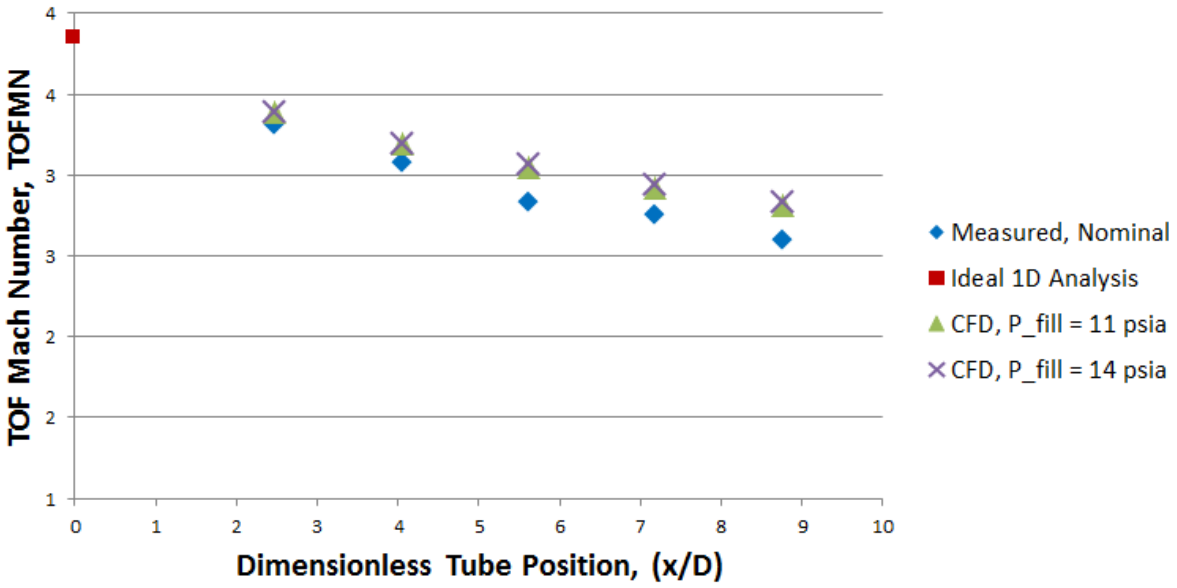

Figure 5.23. Comparison between experimental and simulated TOFMN in Phase 2. Experimental results show a faster decay than either CFD profile. The differences in CFD profiles were minimal despite the different initial conditions.

Another interesting result from this graph is the minimal difference between the decays originating with the different initial conditions. The pseudo-air mixture demonstrates a slightly faster decay compared to the air mixture. When each profile is fitted with an exponential function, the decay rates for each condition are $A_{exp} = -0.00999$ [1/in], $A_{CFD,pseudo} = -0.00774$ [1/in], and $A_{CFD,air} = -0.00741$ [1/in]. These were the decay rates used in the analytical models presented in Chapter 3.

Conclusions

The wave speed characterization showed that the pre-detonator greatly improved the test-to-test repeatability of the detonation tube apparatus. While the detonation wave speeds matched

the expected CJ conditions of the acetylene-pseudo-air mixture, the experimental wave speed profiles showed a faster decay rate than the CFD results. The reason for this difference is not fully understood, but it is believed that the area change associated with the pre-detonator strengthened the Taylor expansion wave, causing a faster decay.

5.5 Phase 3 – Design for Manufacture of Bifurcating Duct Diffuser

As detailed in Chapters 3 and 4, the bifurcating duct concept was selected as the most promising diffuser design. Of that concept, the design with the larger secondary to primary path length ratio ($L_{s,total}/L_{m,total} = 1.41$) was selected since it provided greater delay between exiting pulses and also offers provides better availability preservation. During the analytical and computational modeling stages, only designs with physically relevant geometries were investigated. A MATLAB code was generated to compute physical parameters such as pipe lengths and miter angles given the dimensions of a pipe lateral.

Because these models were made faithful to physical constraints, design for manufacture was a relatively simple process. Figure 5.24 shows a machine drawing of the bifurcating duct prototype diffuser. The first feature worth noting in this design is the converging neck, serving as a transition from NPS 4" Schedule 80 to NPS 3" Schedule 40 pipe. Despite this being a single shot apparatus, this neck down was included to improve the experiment's analogy to a multi-shot device. Multi-shot PDC's often employ a converging nozzle used to prevent overfilling during the fill process. After the area convergence, a $12" \approx 4 * ID$ run-up length was used so that the transient effects of the area change could subside and help the duct bifurcation behave as anticipated. An "off-the-shelf" lateral pipe wye was used as the flowpath bifurcation. Transducer bosses were spaced 6" apart and arranged such that wave speeds into and out of the wye could be measured. Similarly, pairs of bosses were placed along both the primary and secondary pipes to measure wave propagation. In general, the pipe and lateral were made from carbon steel and the bosses made from 304 stainless steel.

Figure 5.25 is a photograph of the finished prototype situated with the modified baseline. To help restrain the secondary, free-hanging pipe, the device was secured using a cushioned plywood chuck and a pair of ratcheting tethers. The main pipe rests on a pair of steel rollers used for easy disassembly in between tests.

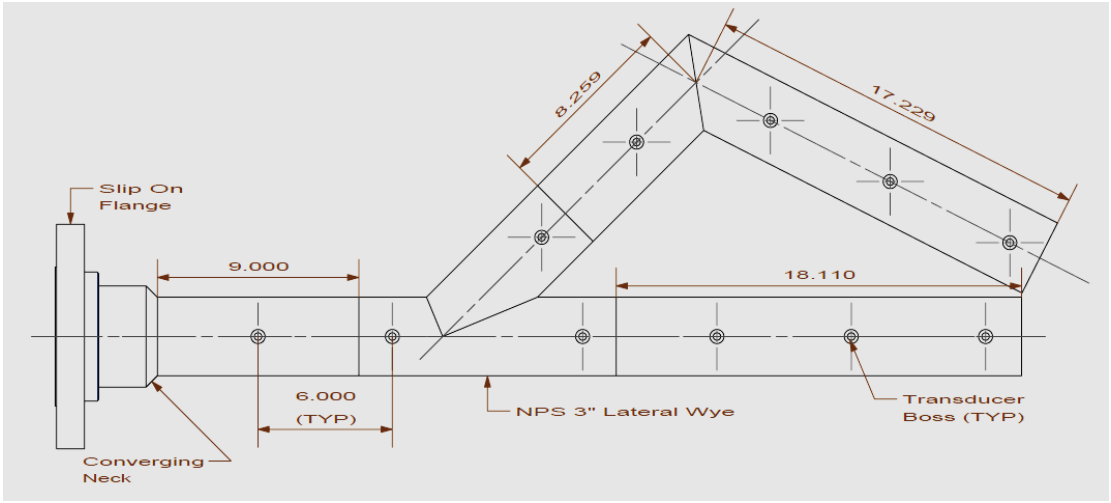

Figure 5.24. Machine drawing of the diffuser prototype. Dimensions in inches.

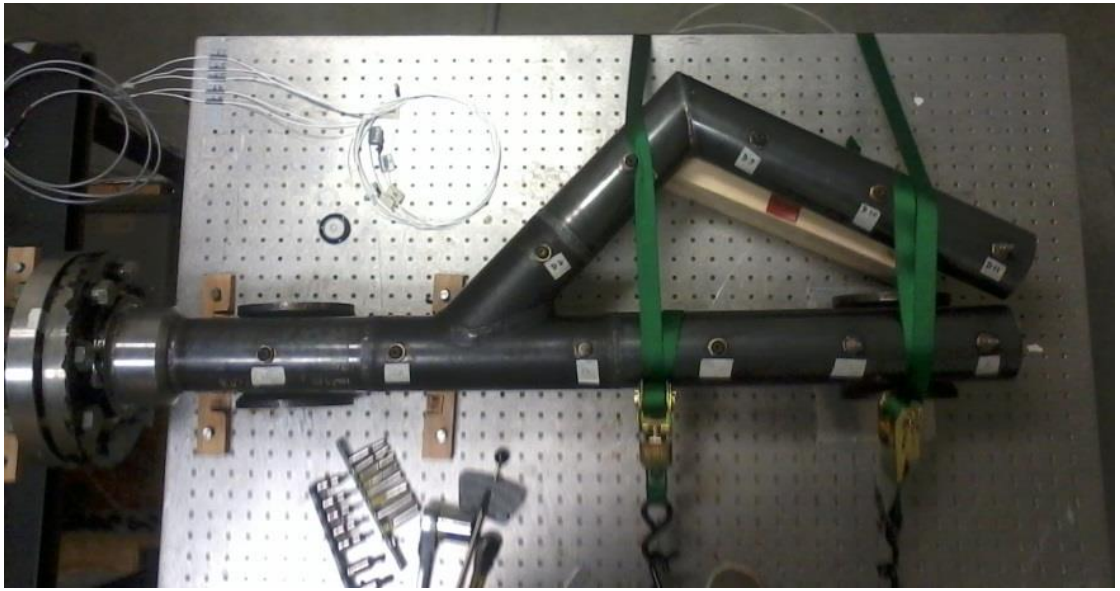

Figure 5.25. Photograph of the finished prototype installed with the detonation tube baseline. Photo by author, 2014.

5.6 Phase 3 – Diffuser Shakedown, Evaluation

The bifurcating duct prototype was tested fifteen times using the pseudo-air fill conditions outlined in the previous section. These tests sought to characterize the wave dynamics of the device and to measure various metrics for comparison to analytical and computational models. Because of the inability to measure temperature, these comparison metrics are limited to the realm of timing, wave speeds, and pressure attenuation. Although energy/exergy content of the flow could not be measured, agreement of the other parameters can provide reasonable confidence that the models and experiment behave similarly with respect to the thermal energy advection.

Phase 3 – Wave Dynamics Characterization

Figure 5.26 and Figure 5.27 are diagrams illustrating wave dynamic results of the bifurcating duct device. In these diagrams, an arrow indicates an average wave speed between two locations measured by the cross correlation process previously described. Wave speed is indicated by the relative arrow length with no scale provided. The pressure rise (PR) across the shock wave as computed by Equation 2.8 is indicated by the color of the arrow, with the color bar for this scale given. The pressure rise in this case is due the passage of an inert shock wave generated by the detonation process.

A brief comparison of these diagrams shows that CFD wave speeds are generally larger in magnitude compared to the experimental results. The incident wave speed in the simulation was larger than that measured in the experiment, where $M_{i,CFD} = 3.39$ and $M_{i,exp} = 3.22$. Recall from the last section that the the experiment exhibited faster wave decay than in simulation. This fact is likely the reason that the wave magnitudes differ in Figure 5.26 and Figure 5.27.

Despite the differences in magnitude, the experimental and computational results qualitatively very similar. From a qualitative perspective, three major wave dynamic features are common between the two. First, a strong incident wave (red) meets the bifurcation and splits into two weaker waves of asymmetric strength as predicted. The wave in the primary duct is much stronger the wave in the secondary, lateral duct. Second, the shock in the main duct monotonically decays after the split as it approaches the exit in each case. This attenuation is a result of the Taylor expansion and agrees with the basic wave dynamics of the problem. Third, in

the secondary duct, the wave reflects around the duct elbow and temporarily weakens during this reflection-diffraction process. As the transient reflections subside, the shock strengthens slightly as it approaches the exit.

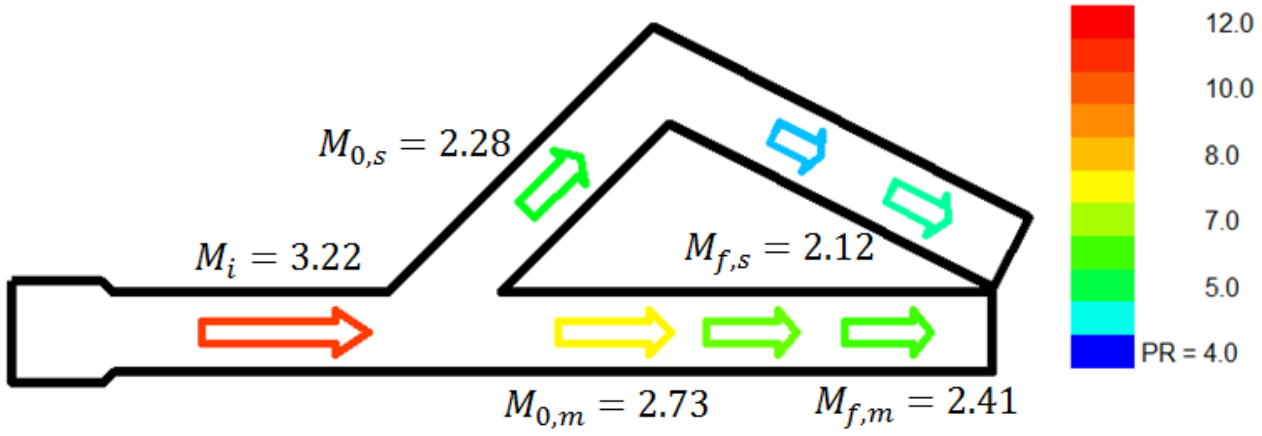

Figure 5.26. Arrow diagram illustrating wave speed results for the experimental apparatus. Wave speeds are slightly less than the simulation results, but dynamic behavior is similar between the two.

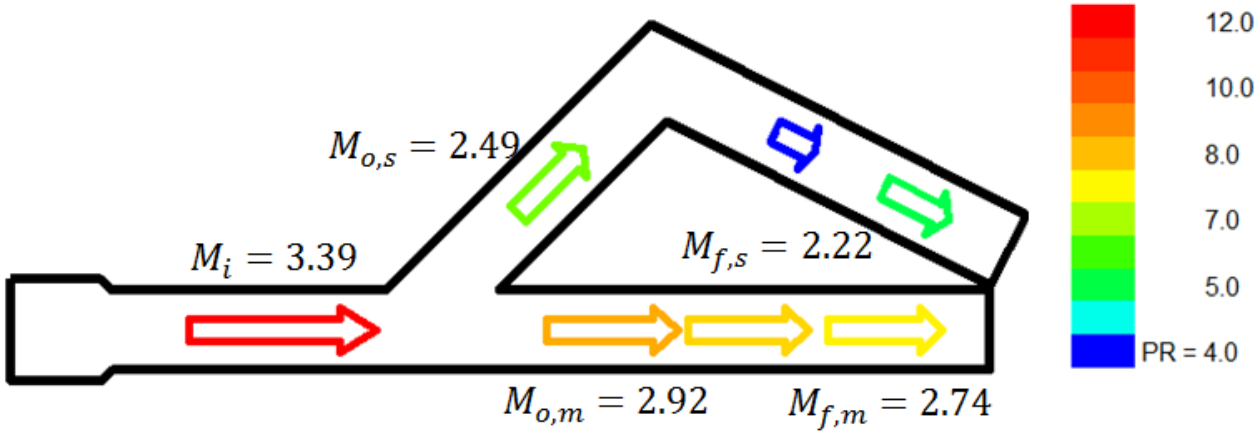

Figure 5.27. Arrow diagram illustrating wave speed results for the simulated apparatus. Wave speeds are generally larger in magnitude than the experiment due to the stronger incident wave. However, dynamics remain consistent between the two.

Phase 3 – Comparison against Analytical and Computational Models

From a quantitative perspective, let us remove ignore the difference in magnitude by considering ratios of wave speeds. That is, let us consider the initial wave speed in each branch compared to the overall incident wave speed (bifurcation attenuation) and the final wave speed compared to the initial wave speed (expansion attenuation) in each branch. Experimental results are compared against computational and experimental models in Table 5.5. Agreement between experiment and simulation is strong, although some discrepancies exist. The bifurcation attenuation, $M_{0,m}/M_i$ and $M_{0,s}/M_i$, agreed very well between experiment and simulation. However, the results for the expansion attenuation through each branch are conflicting. In the experimental results, the main branch attenuation, $M_{f,m}/M_{0,m}$, was greater than the secondary branch attenuation, $M_{f,s}/M_{0,s}$. That said, simulation showed greater secondary branch attenuation than primary. One reason for this contradiction may be the error in measuring the wave speeds in the free hanging arm of the physical prototype.

Despite excellent agreement between experiment and the computational model, the analytical model is clearly deficient in predicting wave attenuation. This model does a serviceable job of predicting bifurcation attenuation in the secondary branch and main branch expansion attenuation. That said, estimates for the other parameters are grossly inconsistent. Although the inaccuracies of the model are disappointing, these results are understandable given the basis for the model. This analytical model used empirical relationships to predict rather complex, non-linear wave dynamic events. The model was never intended to be a high fidelity representation of the physics at hand, but rather a tool used to inform the design process. The model was helpful in choosing a feasible geometric envelope to computationally investigate, but clearly needs further refinement. Possibilities for refinement include three-dimensional treatment of the flow bifurcation and treatment reflection/expansion processes at the secondary duct elbow.

Table 5.5. Summary of wave speed ratios for experimental, computational and analytical models. While experiment and simulation are rather close, the analytical model differs drastically.

	Exp.	*Comp.*	*Anal.*
$M_{0,m}/M_i$	0.85	0.86	0.95
$M_{0,s}/M_i$	0.71	0.73	0.75
$M_{f,m}/M_{0,m}$	0.88	0.94	0.86
$M_{f,s}/M_{0,s}$	0.93	0.89	0.64

Let us now turn our attention to timing parameters. Such parameters may be useful to a designer looking to finely tune a PDC-turbine design, thus making a model's accuracy compared to an experiment of general interest. Three timing parameters are considered: main duct transit duration (τ_m), secondary duct transit duration (τ_s), and stagger between pulse exits ($\Delta\tau$). The experimental, computational, and analytical results for these parameters are shown in Table 5.6. Timing parameters such as these do not have the benefit of being non-dimensional, thus making them reflect the differences in wave magnitude. Regardless, the models show encouraging agreement with experiment despite the differences in magnitude and the inconsistencies suggested above. When comparing experiment and simulation, the transit times of the experiment are slightly larger than that of the simulation. This fact once again owes to the differing decay rates observed. The experiment also over predicts the stagger time between pulses, but still shows general agreement with the simulation. Despite large inaccuracies in predicting wave attenuation, the analytical model does a much better job of predicting the timing parameters. Transit time and thus stagger time qualitatively follow an exponential decay in the short duct distances employed here. Considering a brief sensitivity analysis, errors in wave speed only linearly effect the transit time (see Equation 3.13). Thus , the more significant discrepancies in magnitude shown in the arrow diagrams have a smaller impact on the timing parameters, especially over the shorter duct lengths considered.

Table 5.6. Summary of timing parameters for experiment, computational and analytical models.

	Exp.	*Comp.*	*Anal.*
τ_m *[ms]*	0.531	0.492	0.504
τ_s *[ms]*	0.903	0.862	0.857
$\Delta\tau$ *[ms]*	0.402	0.394	0.353

Phase 3 – Pressure Trace Comparison

Figure 5.28 and Figure 5.29 depict outlet pressure histories comparing experimental and simulated results. The raw and filtered experimental data (grey and black) are measurements taken at a point ~1.5" from the outlet face, whereas the simulated data (blue) is an area-weighted average across the whole outlet, boundary face. In both figures, initial inspection shows that the pressure peaks predicted by the simulation are larger than the filtered peaks observed experimentally. The effect is a result of the old theme that the transmitted shock decays faster in the experiment. Aside from the initial peak, the simulated trace is generally lower in magnitude than the experimental trace. This effect is likely due to the differences in the observation/measurement point. The simulated trace will decay more quickly to the ambient pressure since the taken was taken exactly at the outlet boundary.

As with the arrow diagrams, the experimental and simulated traces show an encouraging similarity with qualitative features. For the main history in Figure 5.28, both data show a strong initial pulse followed by a decay to ambient conditions and then slight inflow (negative pressure). The secondary duct histories are also very similar despite the differences in magnitudes. A strong initial pulse is followed by two secondary pulses before decaying to ambient pressure. These secondary pulses and associated low pressure regions are a result of the flow turning at the elbow. As with the main duct, both simulation and experiment show negative pressures and thus slight influx after the main pressure events.

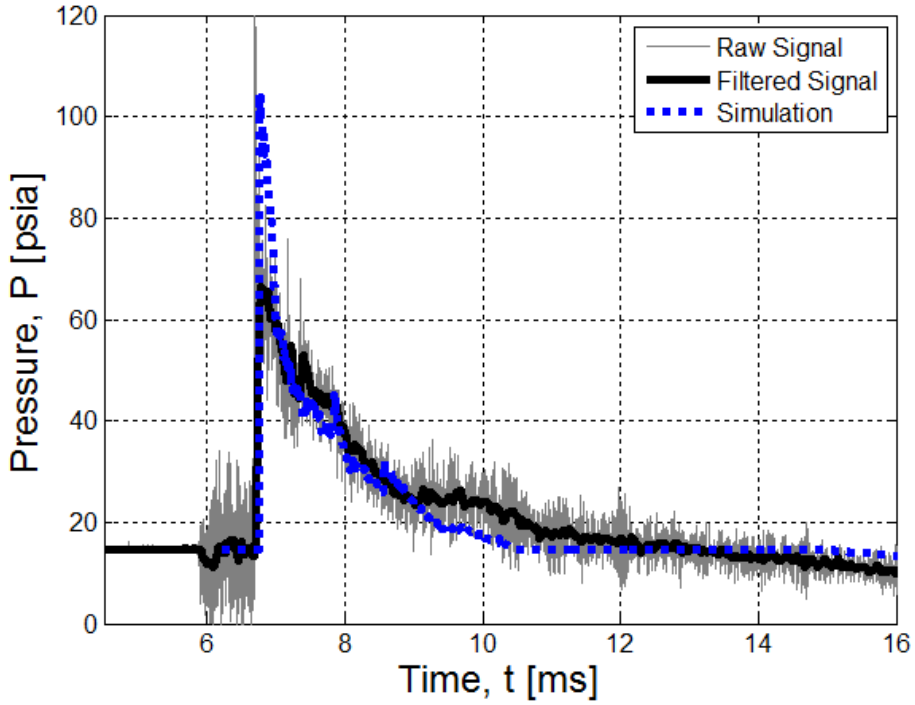

Figure 5.28. Comparison outlet pressure histories for the main duct of the diffuser. Raw and filtered experimental data is shown in grey and black while simulated data is shown in blue.

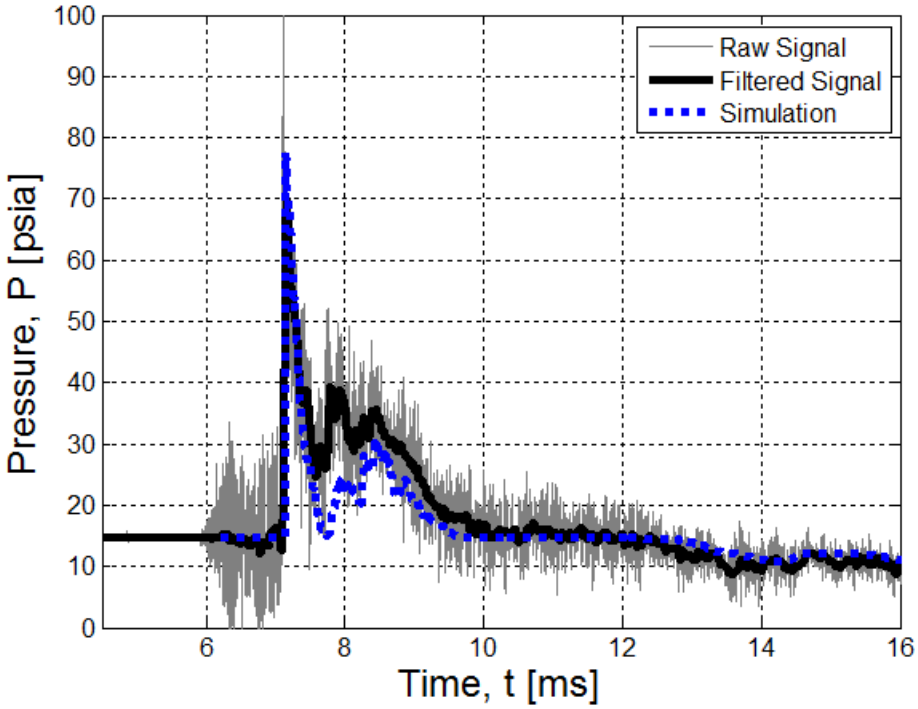

Figure 5.29. Comparison outlet pressure histories for the secondary duct of the diffuser. Raw and filtered experimental data is shown in grey and black while simulated data is shown in blue.

Phase 3 – Efficacy as Diffuser

As the comparison of results suggest, the bifurcating duct concept successfully diffused a detonation pulse generated by the detonation tube. The diffuser successfully split the initial leading shockwave into two pulses and staggered them over time, effectively elongating the pulse event by this mechanism. However, more important than this staggering of the pulses is the overall attenuation. Obviously, weakening the lead shock leads to smaller pressure and temperature fluctuations and thus smaller loads on the turbine. This will help alleviate reliability concerns. However, attenuation of the leading shock front in also crucial for work extraction efforts. The addition of a turbine to the outlet of a PDC acts much like a converging area. A one-dimensional normal shock wave analysis shows that for a strong wave i.e. $M_i > 2.068$ meeting an area contraction will result in reflected waves. This is since the incident shock has induced a supersonic, post-shock flow. These reflected waves serve a loss mechanism and increase entropy in the flow field. As mentioned in the literature review, reflected waves have been experimentally observed with both strong shocks (totally unreactive flows) and detonations. While wave attenuation from the natural expansion processes destroys the high availability of the detonation products, it is a necessary process for effective work extraction. A bifurcating duct concept could be a more effective means of attenuating a detonation than a PDC with a very small fill fraction. This diffuser utilized attenuation from both the bifurcation and natural expansion processes, whereas a partial fill configuration uses only the latter. Due to the length requirements of the DDT process, using just a partial fill to achieve the same wave attenuation would make the actual PDC much longer, increasing blowdown times and decreasing maximum operating frequencies.

Chapter 6: Conclusion

6.1 Project Summary

The goal of the present work was to design, evaluate, and implement a diffuser extension intended to distribute the energy contained in the exhaust flow of a Pulse Detonation Combustor. The diffuser is an inert extension which would aid in turbine reliability and work extraction in an energy generation application. An effective diffuser would seek to attenuate peak pressures, increase pulse duration, improve pulse steadiness, and maintain the high availability of the exhaust products.

Three diffuser concepts were generated with each employing different pulse diffusion mechanisms. In general, these concepts sought to employ transient shock dynamic phenomena such as diffraction, reflection, and refraction. The first concept employed an expansion chamber which generated a series of reflected waves intended to elongate and attenuate a decaying detonation front. The second concept used a gradual area divergence to create radially propagating reflections intended to diffuse the main wave. The third concept made use of a bifurcating flowpath to split the incident wave into two waves which exited the assembly at staggered times. For each concept, simple analytical models were developed to estimate timing pressure attenuation parameters. These models provided quantitative insight into geometric scaling and drove the detail design process.

Once specific designs were finalized for each concept, they were evaluated in a series of CFD simulations. The results of these simulations provided great insight into diffuser performance as defined pressure attenuation, pulse elongation, steadiness, and entropy generation metrics. These simulations suggested that the Expansion Chamber and Bifurcating Duct concepts could serve as viable diffusers. The Expansion Chamber concept elongated the pulse by a factor of 3 while providing substantial pressure attenuation ($\Pi \approx 0.4$). The Bifurcating Duct concept improved steadiness considerably and provided the best pressure attenuation ($\Pi \approx 0.35$). In the end, a Bifurcating Duct concept was chosen for fabrication due its ease of manufacture, ability to be assessed using pressure diagnostics, and its optimal simulated performance. Most importantly, this concept generated less entropy than the Expansion Chamber concept and maintained the high availability of the exhaust flow.

With regard to experiment, a detonation tube was constructed to serve as a lab-scale analogue to a multi-shot, PDC-turbine array. A detonation tube is a single shot device which operates based on the same physics as a multi-shot PDC, but differs with regard to initial and boundary conditions. It was argued that these differences would not significantly influence the wave dynamics and results of the current work.

The baseline tube underwent an initial design and subsequent modification, called experimental Phases 1 and 2. Each of these baselines were characterized and results were compared against qualitative and computational expectations. In general, these baselines behaved as was anticipated. Phase 3 of experimentation involved the fabrication and experimental evaluation of a bifurcating duct design. The results from Phase 3 indicate that duct qualitatively performs as expected, successfully splitting one strong wave into two staggered waves. However, the experimental results conflicted somewhat with both computational and analytical models. Estimates for wave/pressure attenuation were inconsistent with experimental results. However, model estimates for timing parameters were much better. Such timing parameters could produce useful results for a designer looking to design and tube a PDC-turbine array employing this bifurcating duct concept.

6.2 Conclusions

It was found the detonation diffusion (as defined) is a feasible concept. The bifurcating duct diffuser performed as expected in many regards. While quantitative modeling was hit or miss, the device exhibited the wave dynamic properties predicted by analysis and by simulation. It is believed that such a device could be beneficial in implementing a PDC in a turbine work extraction setting. The device attenuates the resulting detonation wave such that mechanical loading on a turbine section will be less extreme. With regard work extraction using a turbine, previous research indicates that a strong detonation/shock will reflect from the turbine section since it acts essentially as an area contraction [14]. With this in mind, efficiently attenuating a decaying shock wave is essential for turbine work extraction. A reflection event can be avoided if the main shock is sufficiently weakened to the point where post-shock particles are subsonic [39]. It would seem that a bifurcating duct concept is an effective way to attenuate the decaying detonation front while minimizing entropy generation associated with detonation product mixing.

There is little argument that the detonative mode of combustion is a better use of fuel per pound, as many modeling efforts have suggested. However, the process of efficiently expanding the products detonation wave is an extremely difficult problem The assumption that these products may isentropically expand through a turbine is dubious one at best, and the advantages of detonative combustion will only be seen once this problem is addressed more carefully [77,78].

6.3 Recommendations for Future Work

Based on the results of the current research, the following recommendations for future work are suggested:

- The largest deficiency in the present work was the agreement between the analytical modeling efforts and experimental results. While the experiment qualitatively met expectations, the results were inconsistent when compared to the analytical model. In particular, the model's estimates for wave attenuation at the bifurcation and in the secondary duct were highly inconsistent with computational and experimental results. In the present model, the inlet/outlet relationships for the bifurcation were formulated using two-dimensional shock dynamics. These relationships could be improved by considering the three-dimensional shock dynamics associated with the splitting of circular ducts Similarly, it is important to investigate how the remnants of the Taylor Expansion processes have on this diffraction and splitting process. Also, accounting for wave attenuation and time lost at duct elbows will also improve analytical timing and wave attenuation estimates.
- The current work relied upon the assumption that the wave dynamics between single shot and multi-shot experiments were practically the same. To avoid this assumption, future work should extend the analysis started here to multi-shot experiments and simulations. In particular, the effect the purging/filling processes and the boundary conditions have on the diffusion mechanisms suggested herein. Measurement of the mechanical loading and work extraction could be compared against a baseline configuration. Also, in a multi-shot PDC experiment, temporal resolution of temperature measurements could be attempted.
- Specifically with the bifurcating duct concept, it is important to further investigate geometric parameterization and optimization of the design. There exists some

relationship between basic geometry (bifurcation type, path lengths), timing parameters, and wave attenuation. Such relationships would be very useful to a designer looking to design a multi-shot PDC-turbine array. Alluded to before, more accurate analytical models will aid in this effort due to the real time required to run just one simulation.

References

1. Turns S. An Introduction to Combustion: Concepts and Applications. 2nd ed. Boston: McGraw-Hill;

2. Lee JH. The Detonation Phenomenon. 1st ed. New York, NY: Cambridge University Press; 2008.

3. Coleman ML. Overview of pulse detonation propulsion technology [Internet]. DTIC Document; 2001. Available from: http://oai.dtic.mil/oai/oai?verb=getRecord&metadataPrefix=html&identifier=ADA390257

4. Hutchins TE, Metghalchi M. Energy and exergy analyses of the pulse detonation engine. Journal of engineering for gas turbines and power. 2003;125(4):1075–80.

5. Akbari P, Szpynda E, Nalim MR. Recent developments in wave rotor combustion technology and future perspectives: a progress review. AIAA Paper. 2007;5055:2007.

6. Petela R. Application of exergy analysis to the hydrodynamic theory of detonation in gases. Fuel processing technology. 2000;67(2):131–45.

7. Bellini R. Ideal cycle analysis of a regenerative pulse detonation engine for power production. 2011 [cited 2013 Jun 3]; Available from: http://dspace.uta.edu/handle/10106/5479

8. Bellini R, Lu FK. Exergy Analysis of a Hybrid Pulse Detonation Power Device. Journal of Propulsion and Power. 2010;26(4):875–8.

9. George ACS, Gutmark EJ. Trends in Pulsating Turbine Performance: Pulse-Detonation Driven Axial Flow Turbine. AIAA Conference [Internet]. 2012 [cited 2014 Apr 2]; Available from: http://arc.aiaa.org/doi/pdf/10.2514/6.2012-769

10. Baptista M, Rasheed A, Badding B, Velagandula O, Dean AJ. Mechanical Response in a Multi-tube Pulsed Detonation Combustor-Turbine Hybrid System. 44th AIAA Aerospace Sciences Meeting and Exhibit, AIAA-2006-1234 American Institute of Aeronautics and Astronautics (AIAA), Reno Nevada [Internet]. 2006 [cited 2013 Jul 23]. p. 9–12. Available from: http://arc.aiaa.org/doi/pdf/10.2514/6.2006-1234

11. Rasheed A, Furman A, Dean AJ. Experimental investigations of an axial turbine driven by a multi-tube pulsed detonation combustor system. AIAA Paper. 2005;4209:2005.

12. Rasheed A, Furman A, Dean AJ. Wave Attenuation and Interactions in a Pulsed Detonation Combustor-Turbine Hybrid System. 44th AIAA Aerospace Sciences Meeting & Exhibit, Reno, NV [Internet]. 2006 [cited 2013 Jul 23]. p. 2006–1235. Available from: http://arc.aiaa.org/doi/pdf/10.2514/6.2006-1235

13. Rasheed A, Furman A, Dean AJ. Wave Attenuation and Interactions in a Pulsed Detonation Combustor-Turbine Hybrid System. 44th AIAA Aerospace Sciences Meeting & Exhibit,

Reno, NV [Internet]. 2006 [cited 2013 Jul 30]. p. 2006–1235. Available from: http://arc.aiaa.org/doi/pdf/10.2514/6.2006-1235

14. Schauer F, Bradley R, Hoke J. Interaction of a pulsed detonation engine with a turbine [Internet]. DTIC Document; 2003. Available from: http://oai.dtic.mil/oai/oai?verb=getRecord&metadataPrefix=html&identifier=ADA454351

15. Hoke J, Bradley R, Schauer F. Heat Transfer ad Thermal Management in a Pulsed Detonation Engine [Internet]. DTIC Document; 2003. Available from: http://oai.dtic.mil/oai/oai?verb=getRecord&metadataPrefix=html&identifier=ADA454350

16. Panicker PK, Li J-M, Lu FK, Wilson DR. Application of pulsed detonation engine for electric power generation. AIAA Paper. 2007;1246:2007.

17. Rasheed A, Tangirala VE, Vandervort CL, Dean AJ, Haubert C. Interactions of a Pulsed Detonation Engine with a 2D Blade Cascade. 42nd AIAA Aerospace Sciences Meeting & Exhibit, Reno, NV [Internet]. 2004 [cited 2014 Apr 2]. p. 2004–1207. Available from: http://arc.aiaa.org/doi/pdf/10.2514/6.2004-1207

18. VanZante D, Envia E, Turner MG. The attenuation of a detonation wave by an aircraft engine axial turbine stage. 2007 [cited 2012 Oct 2]; Available from: http://ntrs.nasa.gov/search.jsp?R=20070034924

19. Borisov AA, Roy GD, Netzer DW, Frolov SM. Pulse detonation propulsion: challenges, current status, and future perspective. Progress in Energy and Combustion Science. 2004 Jan 1;30(6):545–672.

20. Kailasanath K. Recent developments in the research on pulse detonation engines. AIAA JOURNAL. 2003 Feb 1;41(2):145–59.

21. Kailasanath K. Research on pulse detonation combustion systems–a status report. 47th AIAA Aerospace Sciences Meeting [Internet]. 2009 [cited 2013 May 8]. p. 2009–631. Available from: http://arc.aiaa.org/doi/pdf/10.2514/6.2009-631

22. Kaemming T, Dyer R. The Thermodynamic and Fluid Dynamic Functions of a Pulsed Detonation Engine Nozzle. AIAA Paper. 2004;3916:2004.

23. Kailasanath K, Patnaik G, Li C. The flowfield and performance of pulse detonation engines. Proceedings of the Combustion Institute. 2002;29(2):2855–62.

24. Li C, Kailasanath K. Partial fuel filling in pulse detonation engines. Journal of Propulsion and Power. 2003;19(5):908–16.

25. Li C, Kailasanath K, Patnaik G. A numerical study of flow field evolution in a pulsed detonation engine. AIAA paper. 2000;314:10–3.

26. Wintenberger E, Austin JM, Cooper M, Jackson S, Shepherd JE. Impulse of a Single-Pulse Detonation Tube. 2002 [cited 2012 Oct 3]; Available from: http://authors.library.caltech.edu/25816/

27. Wintenberger E, Austin JM, Cooper M, Jackson S, Shepherd JE. Analytical model for the impulse of single-cycle pulse detonation tube. Journal of Propulsion and Power. 2003;19(1):22–38.

28. Kuo K. Principles of Combustion. 1st ed. New York, NY: John Wiley & Sons; 1986.

29. Zucker RD, Biblarz O. Fundamentals of Gas Dynamics. 2nd ed. Hoboken, NJ: John Wiley & Sons; 2002.

30. Anderson J. Modern Compressible Flow. 3rd ed. New York, NY: McGraw-Hill; 2004. 750 p.

31. Hill PG, Peterson CR. Mechanics and thermodynamics of propulsion, 1992. Addison-Wesley, Reading, Massachusetts;

32. Shepherd JE. Detonation in gases. Proceedings of the Combustion Institute. 2009;32(1):83–98.

33. Handbook of Shock Waves. 1st ed. San Diego, CA: Academic Press; 2001.

34. Thompson PA. Compressible Fluid Dynamics. 1st ed. New York, NY: McGraw-Hill; 1972.

35. Rudinger G. Wave Diagrams for Unsteady Flow in Ducts. 1st ed. New York, NY: D. Van Nostrand Company; 1955.

36. Handbook of Shock Waves. 1st ed. San Diego, CA: Academic Press; 2001.

37. Taylor G. The dynamics of the combustion products behind plane and spherical detonation fronts in explosives. Proceedings of the Royal Society of London Series A Mathematical and Physical Sciences. 1950;200(1061):235–47.

38. Moran M. Availibility Analysis: A Guide to Efficient Energy Use. Corrected. New York, NY: ASME Press; 1989.

39. Salas MD. Shock wave interaction with an abrupt area change. Applied numerical mathematics. 1993;12(1):239–56.

40. Skews BW. The shape of a diffracting shock wave [Internet]. Cambridge Univ Press; 1967 [cited 2013 Aug 22]. Available from: http://journals.cambridge.org/production/action/cjoGetFulltext?fulltextid=381757

41. Bazhenova TV, Gvozdeva LG, Zhilin YV. Change in the shape of the diffracting shock wave at a convex corner. Acta Astronautica. 1979;6(3):401–12.

42. Ben-Dor G. Shock Wave Reflection Phenomena. 1st ed. New York, NY: Springer-Verlag; 1992. 304 p.

43. Han Z, Yin X. Shock dynamics [Internet]. Springer; 1993 [cited 2014 Apr 2]. Available from: http://cds.cern.ch/record/1629248

44. Bazhenova TV, Gvozdeva LG, Nettleton MA. Unsteady interactions of shock waves. Progress in Aerospace Sciences. 1984;21:249–331.

45. CARPENTER H, HAMMITT A. Unsteady flow past junctures in ducts. AIAA Journal. 1964;2(12):2224–6.

46. Newton I. Principia [Internet]. Running Press; 2005 [cited 2014 Apr 2]. Available from: http://books.google.com/books?hl=en&lr=&id=mlLAG5EUZqQC&oi=fnd&pg=PR7&dq=principia+newton&ots=xXoxLIRlkX&sig=x4TkOZaTnq8l-dzYop547FoQNWw

47. Owens ZC, Hanson RK. Single-cycle unsteady nozzle phenomena in pulse detonation engines. Journal of propulsion and power. 2007;23(2):325–37.

48. Dewey JM, McMillin DJ. Observation and analysis of the Mach reflection of weak uniform plane shock waves. Part 1. Observations. J Fluid Mech. 1985;152:49–66.

49. Sanders ST, Jenkins TP, Hanson RK. Diode laser sensor system for multi-parameter measurements in pulse detonation engine flows. power. 2000;5:7.

50. Sanders ST. Diode-laser sensors for harsh environments with application to pulse detonation engines. Mechanical Engineering (Stanford University, 2001) [Internet]. 2001 [cited 2013 Jul 8]; Available from: http://hanson.stanford.edu/dissertations/Sanders_2001.pdf

51. Cooper M, Shepherd JE. Single-cycle impulse from detonation tubes with nozzles. Journal of Propulsion and Power. 2008;24(1):81–7.

52. Cooper M, Shepherd JE. The effect of nozzles and extensions on detonation tube performance. AIAA paper. 2002;3628:2002.

53. Chung K, Lai WH, Li J. Tube diameter effect on deflagration-to-detonation transition of propane-oxygen mixtures. SHOCK WAVES. 2006 Dec 1;16(2):109–17.

54. Cooper M, Jackson S, Shepherd JE. Effect of deflagration-to-detonation transition on pulse detonation engine impulse. 2000 [cited 2014 Apr 2]; Available from: http://authors.library.caltech.edu/25815/

55. Lieberman DH, Parkin KL, Shepherd JE. Detonation initiation by a hot turbulent jet for use in pulse detonation engines. AIAA Paper [Internet]. 2002 [cited 2013 May 21];3909. Available from: http://arc.aiaa.org/doi/pdf/10.2514/6.2002-3909

56. Wintenberger E, Cooper M, Jackson S, Austin J, Shepherd JE. Direct Experimental Impulse Measurements for Detonations and Deflagrations. Journal of Propulsion and Power. 2002 Oct;18(5).

57. Lee JH. Initiation of gaseous detonation. Annual Review of Physical Chemistry. 1977;28(1):75–104.

58. Moen IO, Sulmistras A, Thomas GO, Bjerketvedt D, Thibault PA. Influence of cellular regularity on the behavior of gaseous detonations. Dynamics of explosions. 1986;220–43.

59. Kaneshige M, Shepherd JE. Detonation database. 1997 [cited 2014 Apr 2]; Available from: http://authors.library.caltech.edu/25827/

60. Chao TW, Winterberger E, Shepherd JE. On the design of pulse detonation engines. 2001 [cited 2014 Apr 2]; Available from: http://authors.library.caltech.edu/25833/

61. Lindstedt RP, Michels HJ. Deflagration to detonation transitions and strong deflagrations in alkane and alkene air mixtures. Combustion and Flame. 1989;76(2):169–81.

62. Dorofeev SB, Sidorov VP, Kuznetsov MS, Matsukov ID, Alekseev VI. Effect of scale on the onset of detonations. Shock Waves. 2000;10(2):137–49.

63. Beltman WM, Burcsu EN, Shepherd JE, Zuhal L. The structural response of cylindrical shells to internal shock loading. Journal of Pressure Vessel Technology. 1999;121(3):315–22.

64. Birman V. Thermal effects on measurements of dynamic processes in composite structures using piezoelectric sensors. Smart materials and structures. 1996;5(4):379.

65. Operating Guide, Model Series 2300V, High Frequency LIVM Pressure Sensors. Dytran Instruments; 2005.

66. Kar K, Roberts S, Stone R, Oldfield M, French B. Instantaneous exhaust temperature measurements using thermocouple compensation techniques. SAE SP. 2004;169–90.

67. O'Reilly PG, Kee RJ, Fleck R, McEntee PT. Two-wire thermocouples: A nonlinear state estimation approach to temperature reconstruction. Review of Scientific Instruments. 2001;72(8):3449–57.

68. Zimmerschied R, Isermann R. Nonlinear time constant estimation and dynamic compensation of temperature sensors. Control Engineering Practice. 2010;18(3):300–10.

69. McBride B, Gordon S. NASA Chemical Equilibrium with Applications. 1994.

70. Lu FK, Ortiz AA, Li J-M, Kim CH, Chung K-M. Detection of shock and detonation wave propagation by cross correlation. Mechanical Systems and Signal Processing. 2009;23(4):1098–111.

71. Saretto SR, Lee S-Y, Brumberg J, Conrad C, Pal S, Santoro RJ. Studies of detonation transition in a gradual area expansion for multi-cycle PDE applications. Proceedings of the Combustion Institute. 2005;30(2):2809–16.

72. Sinibaldi JO, Brophy CM, Li C, Kailasanath K. Initiator detonation diffraction studies in pulsed detonation engines. AIAA paper [Internet]. 2001 [cited 2014 Mar 19];3466. Available from: http://arc.aiaa.org/doi/pdf/10.2514/6.2001-3466

73. Fievisohn RT. Numerical Investigation of Pre-detonator Geometries for PDE Applications [Internet]. DTIC Document; 2010. Available from: http://oai.dtic.mil/oai/oai?verb=getRecord&metadataPrefix=html&identifier=ADA517597

74. Shchelkin KI. Influence of tube roughness on the formation and detonation propagation in gas. Journal of Experimental and Theoretical physics. 1940;10:823–7.

75. Knystautas R, Lee JH, Guirao CM. The critical tube diameter for detonation failure in hydrocarbon-air mixtures. Combustion and Flame. 1982;48:63–83.

76. Sorin R, Zitoun R, Desbordes D. Optimization of the deflagration to detonation transition: reduction of length and time of transition. Shock Waves. 2006;15(2):137–45.

77. Matsutomi Y, Heister SD. Entropy Considerations on Integration of Pressure Gain Combustors. AIAA/ASME/SAE/ASEE Joint Conference Paper [Internet]. 2010 [cited 2014 Apr 2]; Available from: http://arc.aiaa.org/doi/pdf/10.2514/6.2010-6707

78. Heiser WH, Pratt DT. Thermodynamic cycle analysis of pulse detonation engines. Journal of Propulsion and Power. 2002;18(1):68–76.

Appendix – Detonation TOF Cross-Correlation Source Code

```
%% ----- Moving Average Filter Application-----
close all
clear all

test = 'data_03_14_14_run5.mat';
load(['C:\Users\adamj8\Documents\MATLAB\Dynamic, Experimental Data\',test]);

[xxx numsig] = size(A); numsig = numsig - 1;
clear xxx
t = A(:,1)*1000;            %Convert time vector to ms
deltt = t(2)-t(1);
P = A(:,2:(numsig+1))/0.01; %Convert Voltage Signal to psi
clear A
% axisvec = [5 10 -25 150];
axisvec = [7e3 15e3 -25 200];

n = 30;       %number of points in the moving average
pass = 2;    %number of times to apply the filter
L = 100e3;   %number of points to take from the original pressure signal

%Apply moving average filter to "n" points for "pass" number of times
Pav = P(1:L,:);
for j=1:pass
    for i=1:numsig
        sig = i;
        Pav(:,i) = Shock_Pressure_Moving_Average_rev1(Pav(:,i),n);
    end
end
PP = P(1:L,:);       %shorten raw pressure array
tt = (1:1:L)*deltt;

% Pav(1:10200,3) = 0;
% Pav(1:10500,4) = 0;

% subplot averaged and raw data
dim1 = 2; %plot rows
dim2 = 3; %plot columns
figure
for i=1:numsig
    clear titl
    subplot(dim1,dim2,i)
    h = plot(PP(:,i));
    set(h, 'color', [0.5 0.5 0.5])
    hold on
    plot(Pav(:,i),'LineWidth',1)
    axis(axisvec)
    titl = num2str(i); titl = ['PT', titl];
    title(titl,'FontSize',14);
    ylabel('Pressure, P [psi]','FontSize',14); xlabel('Index,
i','FontSize',14);
    grid on
end
```

```
%% ----- Cross-Correlation to Find the Time Lag Between Peaks -----

%Signals of interest
sig1 = 3;
sig2 = 4;
%Windows of interest based on pressure histories
Lmin = 9.e3;
Lmax = 10.e3;
Ldelt = 10;
Umin = 11.05e3;
Umax = 11.43e3;
Udelt = 5;
L = Lmin:Ldelt:Lmax; U = Umin:Udelt:Umax;

for i=1:length(L)
    for j=1:length(U)
        Ptemp1 = Pav(L(i):U(j),sig1); Ptemp1 = Ptemp1 - mean(Ptemp1);
        Ptemp2 = Pav(L(i):U(j),sig2); Ptemp2 = Ptemp2 - mean(Ptemp2);
        [c lags] = xcorr(Ptemp2,Ptemp1,'unbiased');
        tautemp = lags*deltt;       %Convert time lag to millseconds
        [C T] = max(c);
        tau(j,i) = tautemp(T);
    end
end

tau_m = mean2(tau); tau_m_ind = tau_m/deltt;    %compute the mean time lag
tau_s = std2(tau);                                          %compute the
standard of deviation
err = sqrt(tau_s^2 + 1e-3^2);

%plot
figure
subplot(2,2,1)
plot(Pav(:,sig1))
hold on
plot(Lmin,[-100 100],'k--')
ylabel('Pressure, P [psi]','FontSize',14); xlabel('Index, i','FontSize',14)
Lminstr = ['Lmin = ', num2str(Lmin),', ']; Lmaxstr = ['Lmax = ',
num2str(Lmax),', '];
Uminstr = ['Umin = ', num2str(Umin),', ']; Umaxstr = ['Umax =
',num2str(Umax)];
titl = [Lminstr, Lmaxstr, Uminstr, Umaxstr];
title(titl,'FontSize',14)
grid on
axis(axisvec)

subplot(2,2,3)
plot(Pav(:,sig2))
ylabel('Pressure, P [psi]','FontSize',14); xlabel('Index, i','FontSize',14)
grid on
axis(axisvec)

subplot(2,2,[2,4])
surf(L,U,tau)
xlabel('L','FontSize',14); ylabel('U','FontSize',14)
zlabel('Time Lag, \tau [ms]','FontSize',14)
```

```
tau_m_str = ['time lag = ',num2str(tau_m),' ms, ']; tau_s_str = ['std dev =
', num2str(tau_s), ' ms and '];
err_str = ['total error = ',num2str(err), ' ms'];
titl = [tau_m_str, tau_s_str, err_str]; title(titl,'FontSize',14);
```